An Efficient Tensor-Network Toolbox for Topological Phase Transitions of 2D Spin-Lattice Gauge Models

Naïm Elias Mackel

Elite Master 'Theoretical and Mathematical Physics'

by

Ludwig-Maximilians-University Munich

Technical University Munich

Elite-Network Bavaria

Supervised by

Prof. Dr. Frank Pollmann

Professorship for Theoretical Solid State Physics

at

TUM School of Natural Science

Technical University Munich

February 2026

Contents

Abstract

Topological phases (TPs) are a steadily growing field of multifarious interest in the physics community. On the practical side, TPs are the gateway to exotic materials and fault-tolerant quantum computation. Moreover, they offer a plethora of profound and surprising phenomena, such as anyonic excitations, chiral edge states, and topological entanglement entropy. It is the signature property of topological order that it cannot be captured through local order parameters, nor do topological phase transitions rely on spontaneous symmetry breaking. The Ginzburg-Landau theory fails integrally, which encompasses a substantial hurdle in describing topological phase transitions. Fortunately, states in a topological phase are represented efficiently in terms of tensor networks (TNs) - a powerful class of wave functions that methodically encodes the entanglement structure of the state.

In this thesis, we exploit the holographic principle, intrinsic to the TN-description of topological states, to develop efficient numerical methods to characterize topological phase transitions on large systems. Through an iterative algorithm, we encode the reduced density matrix of 2D translation invariant topological TN states as a 1D infinite matrix product state. This approach allows for efficient classification of the topology, access to physi-

cal quantities, investigation of the universality class, and finite scaling. In particular, we explore the topological entanglement entropy, subsystem fidelity, critical exponents, central charge, and the Fredenhagen-Marcu string (a global order parameter). Remarkably, complexity is at most linear in system dimensions; moreover, we show how results can be extrapolated to the thermodynamic limit.

In addition, we trial our approach against a set of highly relevant models: We assess the accuracy of our method for an analytically solved Ising transition of the Toric Code (TC) on the square lattice - the simplest 2D lattice ($\mathbb{Z}_2$) gauge theory with topological order. We demonstrate that this transition can be generalized to the TC on both the hexagonal and triangular lattices, with the critical points identical to those of the classical Ising model on the triangular and hexagonal lattices, respectively. We find the same Ising transition for the Double Semion model (another $\mathbb{Z}_2$ gauge theory) on the honeycomb lattice. Exemplary of non-Abelian topological phases, we explore the Double Fibonacci model, a candidate for topological quantum computation through anyon braiding.

Our results are in good agreement with prior analytical and numerical approaches. Moreover, the run-times of our methods on commercially available personal hardware are multiple minutes up to a few hours (depending on the model and inquiry).

1 Introduction

There is a single light of science, and to brighten it anywhere is to brighten it everywhere.

- Isaac Asimov

For almost 40 years, the *Ginzburg-Landau Theory* of *Phase Transitions* (GLT) [1, 2] was the physicists' be-all and end-all view on phase transitions. The free energy of the thermodynamic ensemble highlights a set of symmetries, given that high enough thermal fluctuation leads to sufficient disorder, these symmetries are also respected by the system's state. However, tuning the temperature down below the critical value bars the system from disorder, and the symmetry is spontaneously broken. These two regimes are distinct phases of the system, and each phase is categorized by the value a local order parameter (typically a physical observable) takes. If the parameter is null, the system is in the disordered phase; for a finite value, one finds an ordered phase. In 1973, a surprising discovery led Kosterlitz and Thouless [3] to coin *Topological Phases* (TPs). They discovered a phase transition

on the classical 2D XY model, which did not fit the GLT picture; it knows no local order parameters nor symmetry breaking. The transition is characterized by the decoupling of vortex excitations, which appears in tandem with a shift from a power law to an exponential correlation. This transition is topological in two ways. Firstly, the vortex excitations are topologically stable. Secondly, to determine whether all vortices are coupled (into vortex and anti-vortex pairs), there is no local observable; the system must be considered in its entirety. The idea of TPs was propelled into the world of Quantum Physics and truly started to gain traction after the discovery of the *Quantum Hall Effect* (QHE) by Klitzing et al. in 1980 [4] and the *Fractional Quantum Hall Effect* (FQHE) by Tsui et al. in 1982 [5]. Both highlight conducting edge states in addition to integer and fractional quantization of the Hall conductance, respectively. Already in the same year, Thouless et al. related the Hall conductance to a topological invariant - the Chern number, which explains the quantization of the QHE [6]. In 1983, Laughlin managed to construct a family of variational states that describe the FQHE [7]. His states are doubly peculiar: the system contains quasi-particles (and holes) with a fractional charge, and the state has properties analogous to plasma. This insight led him to conjure a new state of matter. It turns out that Laughlin's fractional charge carriers are non-Abelian *Anyons* [8, 9, 10] quasi-particles discovered earlier in 1977 by Leinaas and Myrheim [11] and further explored by Wilczek in the context of magnetic flux tubes [12]. Anyons carry fractional spin and statistics that interpolate between bosonic and fermionic statistics [13]. See [14, 15] for a review of the (F)QHE.

It did not take long until the celebrated Haldane model would revolutionize the field of TPs again by pragmatically constructing another system that also displays Quantum Hall physics [16]. This discovery - in particular - primed the idea of topological insulators: 2D or 3D systems with a topological invariant, that are insulators in the bulk and have chiral edge-modes [17, 18]. By now, this bulk-boundary correspondence - the presence of boundary modes, distinct from the bulk's physics, that nonetheless are only possible due to the physics taking place in the bulk - has become an emblematic property of TPs on lattice models [19, 20]. Topological insulators have been successfully probed in a wide variety of composite materials [21, 22, 23, 24]. Beyond insulators, also conducting phases like semi-metals [25, 26] and superconductors [27] have led to vivid discussion in the community. To this day, the TPs have grown into a solid field that recognizes the existence of a topological invariant, the bulk-boundary correspondence, and the presence of anyonic excitations as simultaneously occurring signature tokens of topological order. In fact,

probably the biggest achievement of the field so far is the periodic table of topological phases, which succeeds in classifying TPs merely by system dimension and the presence and eigenvalue w.r.t. time reversal, particle-hole, and chiral symmetries, respectively [28].

Even in the quantum realm, topological phases are robust against local perturbations. In order to bring the system to another phase, it has to undergo a phase transition (which requires the gap of the Hamiltonian to close). This key property inspired Freedman [29, 30] to propose quantum computers constructed on a topological substrate to shield quantum information from decoherence. Identifying qubits with TPs instead of states makes them robust against perturbations from the environment. A concrete and pragmatic system that qualifies for *Topological Quantum Computation* (TQC) was quickly proposed by Kitaev [31, 32]. Kitaev's praised *Toric Code* (TC) model is a simple spin-lattice model with $\mathbb{Z}_2$ gauge symmetry that is inhabited by four distinct kinds of anyons and accommodates two qbits. Quite remarkably, the TC's ground state (GS) has absolute entanglement [33]. The GS has local entanglement that grows linearly with the length of the partition over which the entanglement is considered. However, beyond that, it also has large-scale entanglement that has the same value no matter the system or partition size. It was already understood beforehand, that the braiding of anyonic excitations is a signature of topological order and the generator behind large-scale entanglement of the system [34, 35], which has led to understanding this absolute entanglement or *Topological Entanglement Entropy* (TEE) as another signifier of topological phases [36, 37, 38]. By now, TEE has grown into a second gold standard to detect TPs [39, 40]. The Toric Code has been successfully implemented on quantum processors and probed experimentally for its topological properties [41].

In 2005, Levin and Wen managed to classify a whole subset of topological phases nested on lattice gauge theories through tensor category theory (as opposed to group theory in ordinary phases), and proposed a mechanism for topological phase transitions: string-net condensation (as opposed to particle condensation) [42]. The classification relies on fixed-point wave functions, which are unique to and emblematic of their respective phase. As such, they highlight all the topological properties of the phase, possess a known local gapped parent Hamiltonian, and offer a clear picture of the phase in terms of a string-net. The picture is, however, short of a precise understanding of the states beyond these fixed points. Alternative approaches must be applied to generate an understanding of these states and to characterize topological phase transitions; these typically rely on strenuous calculations. The central

questions of this thesis arise naturally: Is there an efficient numerical approach towards understanding states beyond the fixed point for a general lattice gauge theory? Which quantities can be accessed easily to accurately resolve topological phase transitions? Does complexity scale favorably with system size?

What to expect from this thesis

Studying topological phases and phase transitions is an ongoing endeavor in the community. Some transitions have been solved analytically, like [43], yet those are a limited and judiciously tailored set of cases. On the other hand, the field of *Tensor Networks* (TNs) has proven itself marvelously successful and intuitive at constructing powerful numerical methods, gaining deeper insight into quantum many-body wave functions, rendering symmetries and entanglement manifest in the description, and giving pictographic representations to states and operators [44, 45, 46, 47, 48]. Naturally, TN methods have seen a vivid development and systematic implementation [49]. The unrivaled TN-bible is [50]. A key strength of TNs is that they offer an efficient representation of the ground state of local and gapped Hamiltonians in the form of *Projected Entanglement Pair States* (PEPSs) [51]. This aspect marries itself intimately to the Levin-Wen string-net picture, which categorizes TPs through the ground states of local and gapped Hamiltonians emblematic of their phase. Remarkably, the TN representation of any of the Levin-Wen states can be systematically constructed [52]. Inferentially, tensor network methods have been used fruitfully to characterize topological phase transitions [53, 54, 55, 56, 57].

In this work, we exploit key features of topological phases, of the string-net picture, and of TN representations, to develop and trial efficient numerical methods that expand on the already existing toolbox for topological phase transitions. Specifically, we embrace the holographic principle reminiscent of the area law manifest and in PEPS [58] to write the *Reduced Density Matrix* (RDM) of a 2D string-net state as a 1D infinite *Matrix Product State* (MPS). From the RDM multiple signifiers of topological order, like TEE and order parameters, but also characteristics of phase transitions, like the reduced fidelity and critical exponents, can be obtained. Our approach comes at a twofold advantage: Foremostly, run times are efficient even at large system sizes, e.g., multiple seconds up to a few minutes in order to find the TEE of an arbitrary state, and multiple minutes up to a few hours to generate phase diagrams, running the code on commercial-standard PC hardware. Addition-

ally, we show that the validity of results can be extended from finite systems to the thermodynamic limit. The manuscript will be structured as follows:

Chapter 2 introduces the base concepts on which this thesis is constructed. From the focal point of Levin-Wen states, we will outline noteworthy features of topological phases and phase transitions. Then, we take an entanglement-guided approach to understand the structure of topological states, to motivate the area law, and to render evident why the tensor network description is so useful and natural.

Chapter 3 constructs the theoretical foundation of our approach. We demarcate under what assumptions our method works, then we prove the holographic principle from which we determine an *infinite Time-Evolving Block Decimation* (iTEBD) algorithm to efficiently construct the reduced density matrix. Subsequently, we explore which quantities relevant to topological order and phase transitions can be efficiently accessed: TEE, reduced fidelity, string order parameters, central charge, and critical exponents.

Chapter 4 puts our approach to the test. We introduce a set of models, namely the Toric Code, the Double Semion model, and the Double Fibonacci model, for which we run the numerics developed in Chapter 3. We review our results in the context of known results from other methods.

Chapter 5 will conclude the manuscript, leaving us space to comment on the quality of our results as well as on possible outlooks.

2 Topological Phases and Tensor-Networks

Intuition would naively compel that local interactions lead to local order in a system. In fact, it is this picture that motivates the Ginzburg-Landau Theory and captures a vast field of phase transitions through the lens of interaction-driven local order conflicting with fluctuation-driven disorder. It is as surprising as it is exciting that topological phases refute this intuition by offering "global" topological order in systems ruled by local Hamiltonians, all due to large-scale quantum entanglement. In their seminal paper [42], Levin and Wen outline for the vast class of "doubled" topological phases how this order comes about and propose a mechanism for phase transitions that such systems can undergo.

2.1 Levin-Wen String-Nets

The "doubled" topological phases are obtained by stacking two *Topological Quantum Field Theories* (TQFTs) with opposite chiralities; the resulting system is parity and time reversal invariant. Noteworthy physical systems that are contained in this paradigm are all discrete lattice gauge theories and all doubled Chern-Simons theories.

In the following, we will restrict ourselves to 2D systems on a hexagonal lattice; the argumentation generalizes naturally to other lattice geometries. The physical degrees of freedom are spins nested on the links of the lattice. What values s the spin can take depends on the specific gauge theory considered (e.g., $\mathbb{Z}_2$: $s = \pm 1$; $U(1)$: $s \in \mathbb{Z}$; $SU(2)$: $s \in \mathbb{N}/2$). The string-net description is obtained by mapping each spin state to a different string type, whereas we other out one spin type (e.g., $\mathbb{Z}_2$: $s = +1$; $U(1)$ and $SU(2)$: $s = 0$), which will be considered as the absence of strings.

As is, this does nothing for us but shift the picture from states as a superposition of spin configuration to a superposition of string configurations. To shape this into a gauge theory that can explain topological order, constraints need to be added: On any vertex of the lattice, exactly three strings meet, for which one can fix branching rules - i.e., a condition on which types of strings are allowed flow into each other. Fixing the data

1. **String types:** Labeling strings $i = 0, \ldots, M$ for $M + 1$ spin states.

2. **Orientation:** To keep track of the sign of the flux, it is necessary to define strings i and their duals i^*. They must be connected through an involution $(i^*)^* = i$.

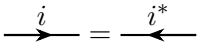

3. **Branching rules:** Triplets of string types $\{i, j, k\}$ allowed to fuse on a vertex.

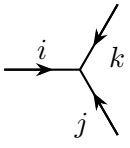

results in a family of constraint states that naturally spans a Hilbert space.

But what is the meaning of these branching rules? Assume that the strings represent some charge flux. Then, for any state with neither flux sources nor sinks the branching rule reflects Gauss's law in each vertex, assuring that none harbor a charge (e.g., $\mathbb{Z}_2$ and $U(1)$: $s_i + s_j + s_k = 0$; $SU(2)$: $s_i \leq s_j + s_k$, $s_j \leq s_k + s_i$, $s_k \leq s_i + s_j$, and $s_i + s_j + s_k$ is integer). The resulting networks of strings can be imagined as shown in Fig. 1.

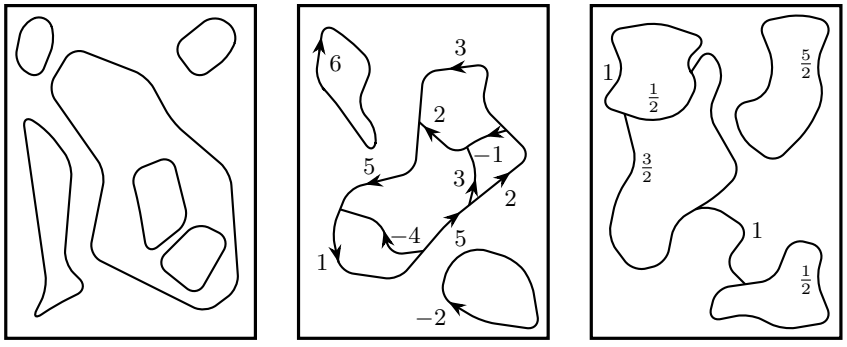

(a) (b) (c)

Figure 1: Exemplary representations of string-nets for (a) $\mathbb{Z}_2$, (b) $U(1)$, (c) $SU(2)$. (Inspired by Fig. 3 in Ref. [42].)

Albeit the local (to each vertex) rules, strings can span the whole system, so it should be somewhat intuitive to see how they impose the topological order. Within a single phase, these global properties must be identical between states. That is, at a global scale, local differences between states are imperceptible. This outlines a typical *Renormalization Group* (RG) argument: Taking any state in a given phase and systematically coarse-graining local details away results in the same fixed-point wave function (Fig. 2). This fixed-point, void of any local attributes, is emblematic of the topological order of that phase.

The fixed-point wave function can be uniquely defined through a set of constraints that relate the amplitudes $\Phi(\cdot)$ of different string-net configurations (arbitrary string-net configurations are represented by gray boxes):

1. The fixed-point only depends on topology; hence, it must be insensitive to continuous deformation:

$$\Phi\left(\quad \xrightarrow{\ i\ } \quad\right) = \Phi\left(\quad \overset{i}{\curvearrowright} \quad\right) \tag{1}$$

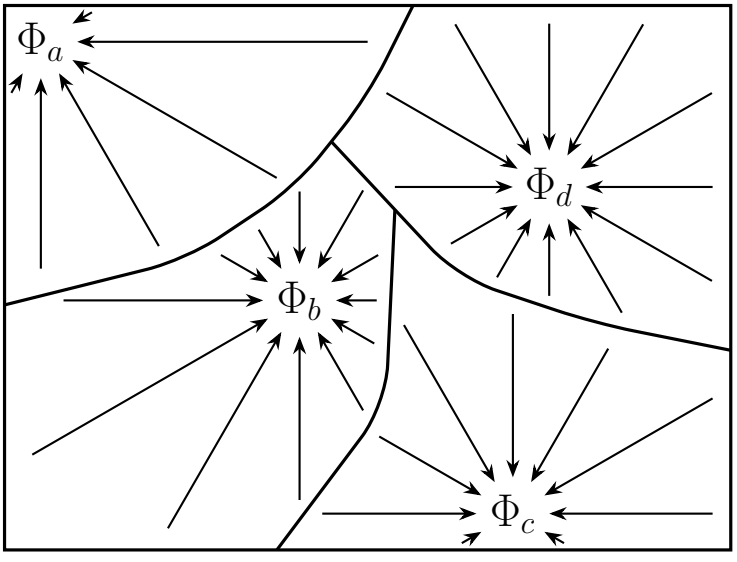

Figure 2: All states in a given phase (a, b, c, and d) flow towards their fixed-point wave function (Φ_a, Φ_b, Φ_c, and Φ_d). (Inspired by Fig. 7 in Ref. [42].)

2. Scale invariance is intrinsic to RG fixed-points; at large enough scales loops are irrelevant, and for $d_i \in \mathbb{C}^{M+1}$

$$\Phi\left(\quad\right) = d_i \Phi\left(\quad \overset{i}{\circlearrowright}\right). \tag{2}$$

3. Analogously, bubbles are irrelevant. At large scales, a bubble looks similar to a single string, which imposes

$$\Phi\left(\quad \overset{i}{\rightarrow} \overset{k}{\circlearrowright} \overset{j}{\rightarrow} \quad\right) = \delta_{ij} \Phi\left(\quad \overset{i}{\rightarrow} \overset{k}{\circlearrowright} \overset{i}{\rightarrow} \quad\right). \tag{3}$$

4. A final rule is necessary to render the fixed-point unique, the least constraining choice is

$$\Phi\left(\quad \overset{i}{\searrow} \overset{m}{\times} \overset{l}{\swarrow} \quad\right) = \sum_n F^{ijm}_{kln} \Phi\left(\quad \overset{i}{\rightarrow} \overset{l}{\rightarrow} \overset{n}{\uparrow} \quad\right), \tag{4}$$

where $F^{ijm}_{kln} \in \mathbb{C}^{(M+1)^6}$ is a rank-6 tensor that is null whenever a branching is unphysical.

Thus, any choice of (F^{ijm}_{kln}, d_i), that satisfies the self-consistency equations

$$F^{ijk}_{j^*i^*0} = \frac{v_k}{v_i v_j}\delta_{ijk}, \tag{5}$$

$$F^{ijm}_{kln} = F^{lkm*}_{jin} = F^{jim}_{lkn*} = \frac{v_m v_n}{v_j v_l} F^{imj}_{k^*nl}, \tag{6}$$

$$\sum_n F^{mlq}_{kp^*n} F^{jip}_{mns^*} F^{js^*n}_{lkr^*} = F^{jip}_{q^*kr^*} F^{riq^*}_{mls^*}, \tag{7}$$

with $v_i = v_{i^*} = \sqrt{d_i}$ and

$$\delta_{ijk} = \begin{cases} 1 & \text{if the branching } i,j,k \text{ is legal} \\ 0 & \text{otherwise} \end{cases}, \tag{8}$$

gives rise to a unique fixed-point state with topological order. Such a solution gives a tensor category, so that tensor category theory is established as the mathematical structure that underlies topological phase transitions, unlike group theory for the GLT. Nonetheless, solutions to the self-consistency equations (5)-(7) can be constructed through group theory: Pick a group G, then $M+1$ is the number of irreducible representations, d_i gives the dimension of the representations, and F^{ijm}_{kln} is the $6j$-symbol of the group.

So far, we have pursued a "state-first" approach; however, quite amazingly, Levin and Wen derived a family of local parent Hamiltonians of form

$$H = -\sum_S Q_S - \sum_P B_P. \tag{9}$$

The sums go over the stars S, respectively, plaquettes P of the lattice (see Fig. 3). The local operators act as

$$Q_S \left| \begin{array}{c} i \\ j \quad k \end{array} \right\rangle = \delta_{ijk} \left| \begin{array}{c} i \\ j \quad k \end{array} \right\rangle, \tag{10}$$

and

$$B_P = \sum_{s=0}^{M} a_s B_P^s, \tag{11}$$

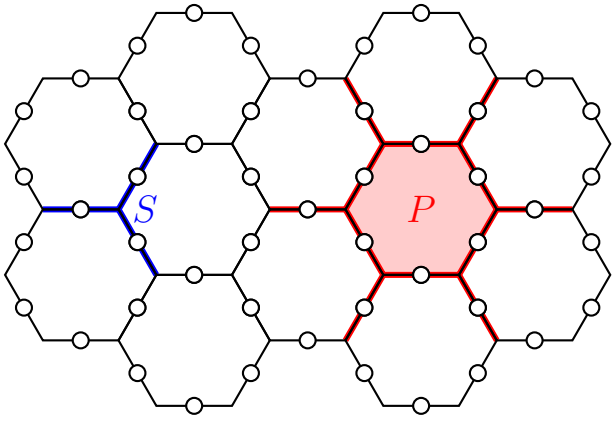

Figure 3: The honeycomb lattice consists of stars S and plaquettes P, the spins (represented as circles) live on the links. Each star corresponds to the three spins located around a vertex. The spins nested on the edges of a hexagon form the plaquette. The six links radiating out of the plaquette correspond to the legs of P.

where $a_{s^*} = a_s^*$, but are otherwise arbitrary. The explicit plaquette expression is quite cumbersome, yet, for sake of completeness:

$$B_P^s \left| \begin{array}{ccccc} & b & & c & \\ g & & h & & i \\ a & & & & d \\ l & & & & j \\ & f & & k & \\ & & e & & \end{array} \right\rangle = \sum_{i',\ldots,h'} B_{P,ghijkl}^{s,g'h'i'j'k'l'}(abcdef) \left| \begin{array}{ccccc} & b & & c & \\ g' & & h' & & i' \\ a & & & & d \\ l' & & & & j' \\ & f & & k' & \\ & & e & & \end{array} \right\rangle, \tag{12}$$

with

$$B_{P,ghijkl}^{s,g'h'i'j'k'l'}(abcdef) = F_{s^*g'l'^*}^{al^*g} F_{s^*h'g'^*}^{bg^*h} F_{s*i'h'^*}^{ch^*i} F_{s*j'i'^*}^{di^*j} F_{s*k'j'^*}^{ej^*k} F_{s*l'k'^*}^{fk^*l}. \tag{13}$$

In essence, the star operator Q_S detects whether there is a charge located at a vertex (alternatively, whether the branching rule is violated). The plaquette operator B_P detects whether there is any "magnetic" flux passing through a plaquette. Charges and magnetic fluxes both come at an energy cost. One can prove (although strenuously) that

- $\forall S, P\ [Q_S, B_P] = 0$, thus the Hamiltonian is exactly soluble;

- Depending on the choice of a_s, $M+1$ different phases can be obtained;
- For $a_s = \frac{d_s}{\sum d_i^2}$, the fixed-point wave functions Φ give the ground states to these Hamiltonians, that is, $\forall S, P$

$$Q_S|\Phi\rangle = |\Phi\rangle \text{ and } B_P|\Phi\rangle = |\Phi\rangle. \tag{14}$$

2.2 String-Net Condensation and Phase Transitions

The most general picture captures *Quantum Phase Transitions* (QPT) through a Hamiltonian $H(\eta)$ with control parameter η that has a family of instantaneous eigenstates $\{|\psi_n(\eta)\rangle\}$ and eigenenergies $\{E_n(\eta)\}$. The Hamiltonian is gapped except for the *Quantum Critical Point* (QCP) η_c:

- A **first-order transition** is obtained in the case of a level crossing (Fig. 4a), which can take place at a finite system size. The quantum critical point marks where the ground state and the first excited state exchange roles. Due to this abrupt change, the ground state wave function is non-analytic.
- A **second-order transition** occurs when the gap $\Delta = E_1(\eta_c) - E_0(\eta_c)$ closes asymptotically in the thermodynamic limit (Fig. 4b). This avoided level crossing has universal scaling properties, that is, the correlation length ξ diverges according to

$$\xi \propto |\eta_c - \eta|^{-\nu} \tag{15}$$

  with critical exponent ν.

Quantum critical points are a property of pure states; as such, quantum phase transitions take place at zero temperature. QPTs are an outstandingly rich field, to which we cannot do full justice in this manuscript; see [59] for a standard literature treatment.

The Levin-Wen framework delivers a microscopic mechanism for the process of topological phase transitions. Consider a Hamiltonian $H(\eta)$ with $\eta \in [0, \eta_{\max}]$, that smoothly interpolates between H_k - the Hamiltonian in (9) - and H_t:

$$H(0) = H_k \text{ and } H(\eta_{\max}) = H_t. \tag{16}$$

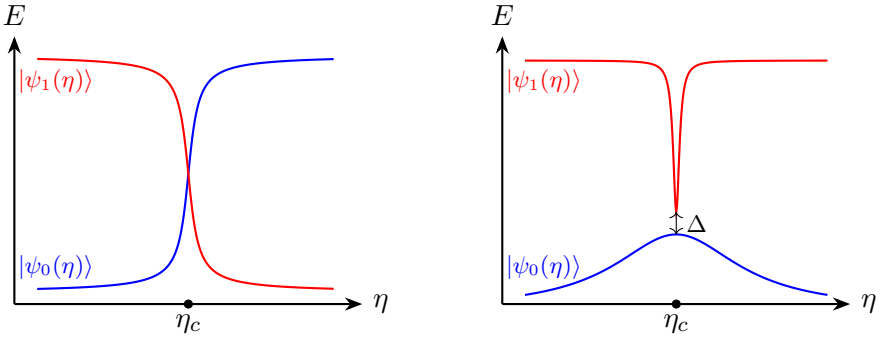

(a) Level crossing.

(b) Avoided level crossing.

Figure 4: Instantaneous spectrum across (a) a first-order QPT and (b) a second-order QPT.

H_t applies a string tension to the string-net (e.g., any link occupied by a string comes at an energy cost), contrary to H_k, this Hamiltonian prefers no or small string-net configurations. As η is driven from 0 to $\eta_{\max}$, the system passes from a regime in which H_k dominates the physics - the ground state is string-net condensed and has topological order (Fig. 5a), into a regime where H_t overweighs, and the string-net is diluted (Fig. 5b). This indicates a phase transition that occurs as the system passes between regimes.

One could also perceive a transition between different topological phases by setting H_t as a Hamiltonian of type (9) but distinct from H_k. The phase transition then consists of "reshuffling" the string-net from following branching rules imposed by H_k to those by H_t.

2.3 Topological Order and Entanglement Entropy

So far, we have only postulated that the condensed string-net states have topological order, handwavily justifying the notion of global order through the all-space-spanning structure of the string nets. Yet, in this work, we are interested specifically in characterizing the topological order of states, thus we ought render explicit how this order manifests.

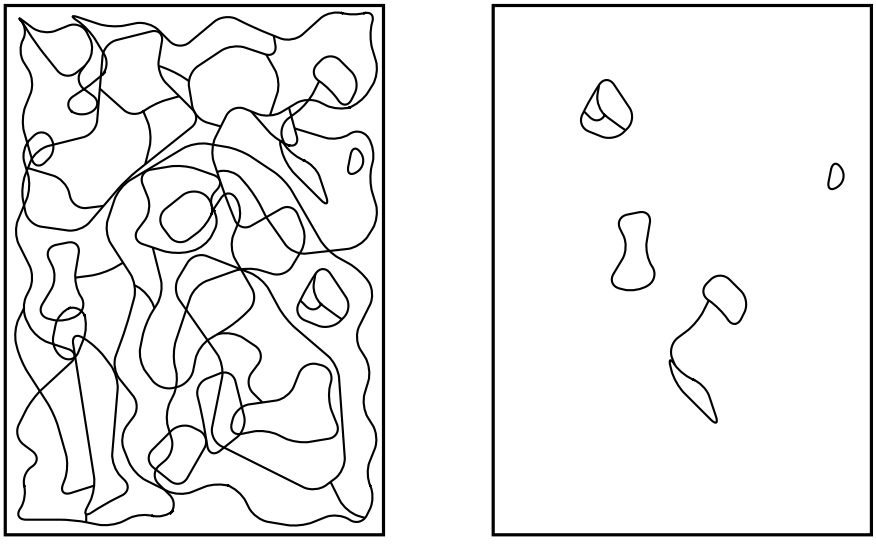

(a) Condensed string-net.

(b) Diluted string-net.

Figure 5: (a) The string-net is condensed, highly fluctuating, and fills in all space, realizing a topological phase. (b) The diluted string-net corresponds to the vacuum state with a few small string-nets; this is a topologically trivial phase. (Inspired by Fig. 1 in Ref. [42].)

2.3.1 Anyons and Statistics

Suppose one acts with a string raising operator $\mathcal{O}_1$ (e.g., sending the string from s to $s+1$) on one specific link of the ground state $|\Phi\rangle$. This action violates the branching rules in the two adjacent vertices, creating two charges (Fig. 6a). The system has been sent to an excited state. Assume now an analogous operator $\mathcal{O}_2$ acting on a second link adjacent to either of the charges, this action restores Gauss's law in that vertex, but violates another vertex (Fig. 6b). There are still two charges, and the system resides in a state with the same excited energy. This game can be continued to freely move the charges throughout the system (possibly to two different ends of the system), spanning a string of operators - or Wilson line - between them (Fig. 6c). The string vanishes in the ground state background; only its ends are detectable. As such, we may understand the charges as quasiparticles, nonetheless, they are remnants of an extended object. This really means that the system is

unaware of local details: there is no "actual" flux line that connects these charges, the string net collectively accounts for the flux between charges. Albeit localized, these excitations are of topological nature. Bringing the endpoints back together allows one to annihilate the charges, and one ends up back in a ground state. The resulting closed string of operators corresponds to a Wilson loop [60]. The identical argumentation is also applicable to "magnetic" fluxes that arise in the same fashion from violating plaquettes.

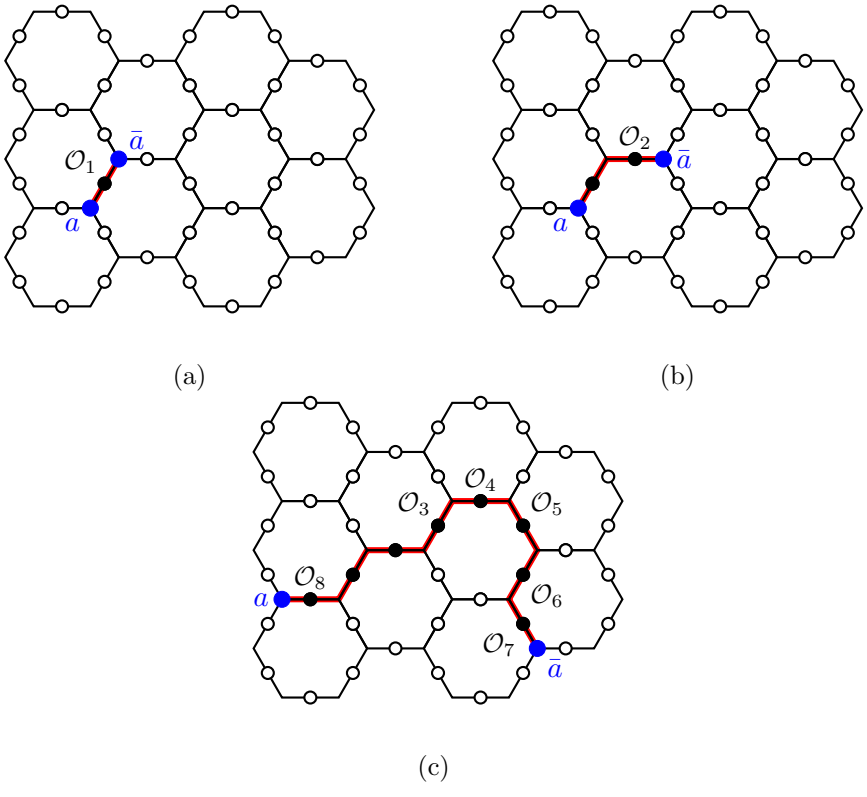

Figure 6: (a) $\mathcal{O}_1$ acts on a spin state (blackened circle) of the GS, creating a charge anti-charge pair $(a, \bar{a})$ on the adjacent vertices. (b) The action of $\mathcal{O}_2$ restores the branching rules in one vertex, but propagates the charge $\bar{a}$ to another vertex. (c) A cascade of operators $\{\mathcal{O}_3, \ldots, \mathcal{O}_8\}$ freely transports the charges to different ends of the system, spanning a string (red) in between them. The operators $\mathcal{O}_i$ are local, but needn't act onto a single spin only. Often, they track whether a charge turns left or right, as such, they generally don't commute.

The described quasiparticles are anyons [11, 12], that is, they have non-trivial statistics (neither fermionic nor bosonic) and mutual statistics, which arise directly from the fact that the operators in a Wilson line are ordered and don't (forcefully) commute between lines nor within a line.

Consider a procedure in which a charge anti-charge pair (a and $\bar{a}$) is created, a is brought adiabatically around $\bar{a}$, then annihilated again. This procedure is fundamentally distinct from just creating and annihilating the pair, as in the former case, the loop has a twist. This twist imposes that the string operators hit the same vertex twice. The associated statistic is given by

$$e^{i\theta_a} = \frac{\left\langle \Phi \left| \right| \Phi \right\rangle}{\left\langle \Phi \left| \right| \Phi \right\rangle}, \tag{17}$$

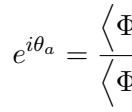

which is related through the spin statistics theorem to the spin s_a of a, and $\bar{a}$: $2\pi s_a = \theta_a$.

The mutual statistic arises similarly: Assume creating two pairs of $(a, \bar{a})$ and $(b, \bar{b})$, then bringing one anyon of pair a around one of pair b (say a around b), this braiding is only possible if the operator string of $(a, \bar{a})$ crosses that of $(b, \bar{b})$. The mutual statistic can be expressed as

$$S_{ab} = \frac{\left\langle \Phi \left| \right| \Phi \right\rangle}{\left\langle \Phi \left| \right| \Phi \right\rangle}. \tag{18}$$

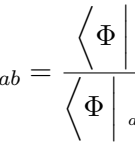

The braiding and statistics of anyons are described by the *Braid Group* [61].

Moreover anyons can fuse, that is, bound states of anyons a and b can be seen as a superposition of other anyons. One usually notes

$$a \otimes b = c \oplus d \oplus \cdots . \tag{19}$$

We may now understand how the Hamiltonian (9) shapes a gauge theory: In the low-energy sector of the theory, the star term enforces the branching rules in all vertices. On the other hand, the plaquette term dictates the dynamics of the string-net, favoring states that are a superposition of many outstretched string-net configurations. Charges and "magnetic" fluxes are forbidden; the theory then describes extended objects: string-nets. In this sector, the operators Q_S and B_P correspond to local gauge constraints. If one breaks these gauge constraints, one obtains a gauge theory coupled to anyonic charges and fluxes acting as "matter" fields: Any anyon anti-anyon

pair is linked through a flux/Wilson-line, turning the anyons into the gauge charges. This is analogous to electric charges and anti-charges spanning an electric field between them, reflecting Gauss's law. The exact argument can be extended to Hamiltonians and GS wave functions that are deformed from the fixed points.

The presence of anyons is rich in consequences: In the case of Abelian anyons, exchanging them leads to a global phase shift in the wave function. In the non-Abelian case this braiding leads to a completely distinct wave function, which can be harvested to construct stable quantum computation by encoding quantum gates through the braiding [62]. Nesting systems with non-bosonic mutual statistics on topologically non-trivial manifolds (like a torus) allows for degenerate ground states, which are different eigenstates with respect to Wilson loops enclosing the handles of the manifold [31]. This idea has led to surface [63] and color codes [64], which engineer topological stabilizer code for quantum memory.

Our takeaway message is that anyons are a signature attribute of topological order and rich in unique properties; as such, they are ideal to probe whether a state is indeed in a topological phase.

2.3.2 Topological Entanglement Entropy

For a bipartite system consisting of subsystems A and B, the entanglement entropy S is a measure of how much information is "shared" between the two subsystems, i.e., how much information cannot be accessed by looking at A and B separately. It is given by the von Neumann entropy of the partial density matrix

$$S = -\mathrm{Tr}[\rho_A \ln(\rho_A)] = -\mathrm{Tr}[\rho_B \ln(\rho_B)], \tag{20}$$

where the reduced density matrices

$$\rho_A = \mathrm{Tr}_B[\rho] \text{ and } \rho_B = \mathrm{Tr}_A[\rho] \tag{21}$$

are obtained from tracing out one of the subsystems.

We will deliver an intuitive argument that underlines how topological order is deeply enshrined in the entanglement spectrum of a state: Assume a Levin-Wen state with M different string types embedded in a large system partitioned such that L links lead from A into B. The only knowledge each subsystem has of its neighboring subsystem is the string-net configuration that is being passed from one to the other. In fact, due to the local rules imposed by the Hamiltonian, this also suffices to fully characterize the subsystem states, so that we may specify the states on either side merely through

the string configuration at the partition. For simplicity, consider a subset of string-net states such that for the first $L-1$ links the strings are totally unconstrained, any configuration is physical, and any configuration comes with the same amplitude (e.g., Toric Code). The total flux between A and B must assure that neither side is carrying anyonic charges; this constrains the Lth link, which must carry a string gauge-compatible with all the others. For the sake of directness, assume that then the Lth link can only carry one specific string. With respect to the partition, the wave function takes the form (see Fig. 7)

$$|\psi\rangle = \frac{1}{(M+1)^{\frac{L-1}{2}}} \sum_{\{s_i\}_{1\leq i<L}} |\{s_i\}\rangle_A |s_L| \{s_i\}\rangle_A |\{s_i^*\}\rangle_B |s_L^*| \{s_i^*\}\rangle_B, \tag{22}$$

where $|s_N|\{s_i\}\rangle$ is the state of the string across the Lth link conditioned to the other $L-1$ strings.

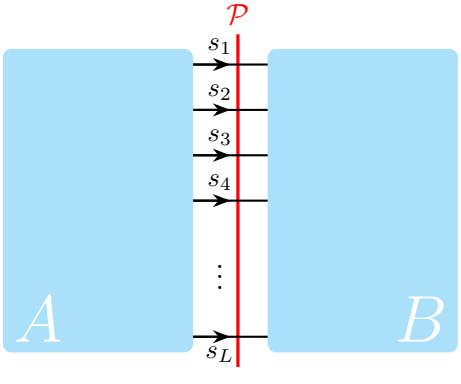

Figure 7: The partition $\mathcal{P}$ splits the system into subsystems A and B (cyan). The set $\{s_1, \ldots, s_L\}$ defines the fluxes from A into B on each of the L links connecting one region to the other. The state in the bulk of each region is specified through these fluxes. Moreover, states in A can only be matched with states in B if the fluxes $\{s_i\}$ out of A correspond to the fluxes $\{s_i^*\}$ into B. Taking an equal superposition of all states that ensure a trivial anyonic charge on both sides gives equation (22).

The states (of the superposition) on either side are all mutually orthogonal, $|\psi\rangle$ satisfies the SVD condition, and it is straightforward to calculate the entanglement entropy:

$$S = (L-1)\ln(M+1) = L\ln(M+1) - \ln(M+1). \tag{23}$$

This result spotlights two well known conclusions:

1. States ruled through local Hamiltonians have an entanglement entropy that is proportional to the length of the partition. The exact proportionality is not universal and can depend on the partition and the Hamiltonian [65, 66]. Typically, this proportionality is referred to as the *Area Law*.

2. The sub-leading term is an artifact of topological order; in particular, it is the requirement that the system does not contain any anyons that globally enforces the flux from A to B to be of trivial charge. This constraint between all the links gives the topological entanglement entropy, which reduces the total entanglement entropy.

Proving this area law in the general case is more involved (particularly due to fusion), but has been done for the string-net states by Levin and Wen [40] following a similar argument. The topological entanglement entropy S^{topo} is a universal property of a TQFT [39] that only depends on the anyonic charges that can be realized in the system:

$$S^{\text{topo}} = \ln(\mathcal{D}) \text{ and } \mathcal{D}^2 = \sum_i d_i^2, \tag{24}$$

the sum goes over all the anyonic superselection sectors that have quantum dimensions d_i, $\mathcal{D}$ is the full quantum dimension.

The discussion about entanglement, superselection sectors, anyons, and entanglement entropy is much deeper and more exciting [67, 68, 69]. Notably, as for gauge theories, the multipartite Hilbert space is subject to non-local constraints (as we argued above), so that it cannot be constructed as a tensor product of subsystem Hilbert spaces. Recent advancements have appropriated the Haag duality - a strong notion of locality and causality [70, 71] from algebraic QFTs - to forward an algebraic approach that proves the stability of anyonic charges and superselection sectors [72, 73, 74, 75, 76].

The presence of the area law

$$S = \zeta L - S^{\text{topo}} \tag{25}$$

will see twofold use in this manuscript: Firstly, we can use the TEE to characterize the topological phase of a state. Secondly, the presence of an area law has deep implications for the structure of a state: it can be represented efficiently in tensor network form.

2.4 Tensor Network Description of Fixed-Point Wave Functions

Due to the tensor product structure of the configuration space of a many-body system, its number of degrees of freedom is bound to grow exponentially with the number of its constituents. Consequently, it is integral to many-body methods to formalize a workaround that renders large systems tractable. The tensor network approach was born in this spirit, specifically tailored to describing strongly interacting systems. The broad line of argument supposes a local and gapped Hamiltonian

$$H = \sum_n h_{n,k}, \tag{26}$$

acting locally on lattice site n and at most k nearest neighbors. Due to the local interactions, the entanglement of the ground state is bound to those k-local blocks, alike excited states at low energy are reminiscent of the ground state up to local perturbations. This locality of entanglement is exactly reflected by the area law, as the region for which the entanglement across a bipartition is relevant is given by the blocks across the partition and thus must scale with its length.

Projected entanglement pair states (PEPS) harvest the area law to systematically construct the ground states of local Hamiltonians [77]: Consider a square lattice, every site is inhabited by four spins with D degrees of freedom, each associated with one of the four links (see Fig. 8). Across each link, these D-dimensional systems are in a maximally entangled state (e.g., $\frac{1}{\sqrt{D}} \sum_{i=1}^{D} |ii\rangle$). The area law is infused into this auxiliary state $|\xi\rangle$ by construction. Moreover, $|\xi\rangle$ can be turned into any other state $|\psi\rangle$ (with d physical degrees of freedom in each site) that also respects the area law (and has equal or less entanglement) through local projections $A^s_{udlr} \in \mathbb{C}^{dD^4}$

$$|\psi\rangle = \otimes_v A(v)|\xi\rangle \tag{27}$$

for sites v. This works as local operations, classical communication, and local measurements allow to transform any state into any other state with equal or less entanglement [78]. The projectors A^s_{udlr} are rank-5 tensors, where the lower indices act on the auxiliary spins (u, d, l, and r for the auxiliary spins entangled to the up, down, left, and right neighbors, respectively), while the upper index reflects the physical degree of freedom.

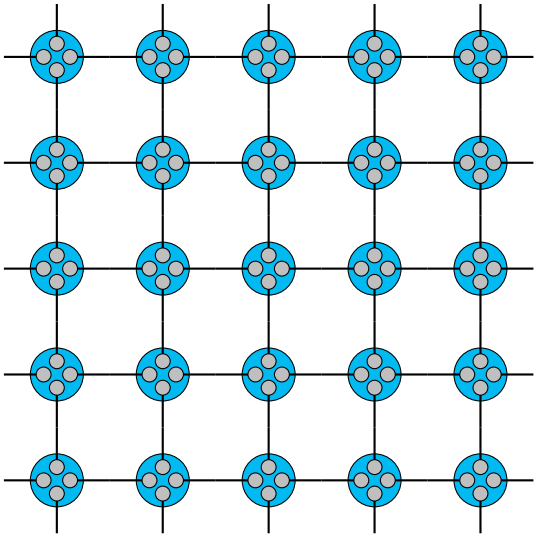

Figure 8: Sites (cyan) are inhabited by four spins (gray), which are in pairwise maximally entangled states (black) across the links of the lattice.

In this framework, states manifest as networks of A-tensors, which have a straightforward pictographic representation: Conventionally, each tensor is represented by a box or sphere and carries a leg for each index. Unless otherwise specified, we will write physical legs as upper and virtual indices as lower indices; moreover, physical legs will be drawn along the z-direction, while virtual indices will lie in the horizontal plane (e.g., Fig 9). Figure 10 translates mathematical operations on tensors into diagrammatic language.

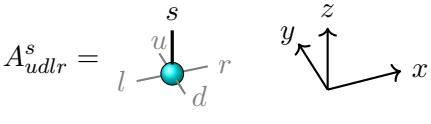

Figure 9: A-tensor drawn according to convention.

We just cooked up a tensor network state that can be expressed as

$$|\psi\rangle = \sum_{\{s_v\}} \mathrm{tTr}\left[\otimes_v A^{s_v}(v)\right] |\{s_v\}\rangle, \tag{32}$$

the tensor trace tTr signifies the contraction of all the virtual (lower) indices

1. **Juxtaposition:** tensors appearing in a diagram disconnectedly correspond to a tensor product, e.g.,

$$A^{ij} \otimes B^{kl} =$$ 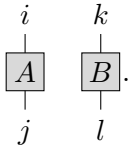 . (28)

2. **Connected legs** represent to the contraction of the corresponding indices, e.g.,

$$\sum_j A_{ij} B_{jk} =$$ 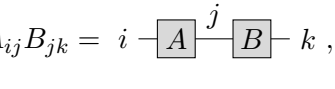 , (29)

   where the sum runs over the full range of the index j.

3. Analogously, the **Trace** corresponds to the contraction of two indices of the same tensor, e.g.,

$$\sum_j A_i^{jj} =$$ 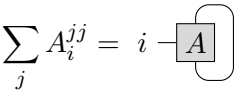 . (30)

4. The **Transpose** exchanges indices, e.g.,

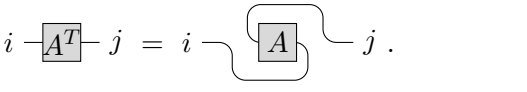 . (31)

Figure 10: Diagrammatic representation of fundamental operations on tensors.

in accordance to the lattice geometry in Fig. 8 (i.e., u with d and l with r indices of neighboring tensors). (Notice that we can forget about the underlying auxiliary system, as the fully entangled states act as identity on the contraction of virtual indices of the A-tensors.) Clearly, the tensor trace plays the role of the probability amplitude of a specific spin configuration in $|\psi\rangle$. Typically, the bra-ket notation is kept implicit, as the maps from physical indices onto local spin states are bijective.

The PEPS construction can be generalized to other lattice geometries and to fewer or more spatial dimensions, whereas the 1D and 2D cases are the most interesting and also most well understood. In the 1D case, it is common to refer to the tensor network state as a matrix product state (MPS).

MPSs can always be brought into canonical form, replacing each A tensors with V and S tensors yields

$|\psi\rangle$ = 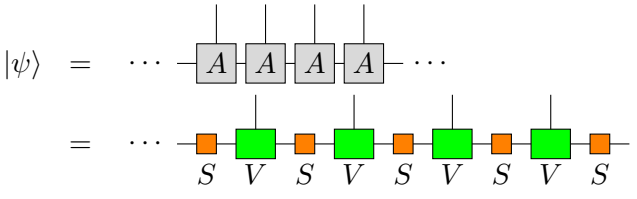

(33)

=

, (34)

where V and S are chosen such that

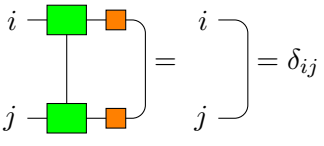

$= \delta_{ij}$ (35)

and

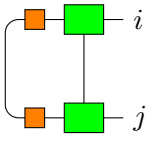

$= \delta_{ij}.$ (36)

The canonical is outstandingly convenient [47, 48]:

- The canonical form assures the singular value decomposition (SVD) condition on any two neighboring V-tensors; thus, the S-tensors contain the Schmidt values and encode the bipartite entanglement structure.
- Due to the Eckart-Young-Mirsky theorem, the compression (reduction in virtual bond dimension) of an MPS is optimal in canonical form.
- Local expectation values become very efficient to compute.

Complementary, operators can be cast into TN-language: Assume $\hat{O}$ an operator acting on spins $\{s_i\}_{n \leq i \leq N}$, then

$$\hat{O} = \sum_{\{s_i'\},\{s_i\}} O_{\{s_i'\},\{s_i\}} |\{s_i'\}\rangle\langle\{s_i\}|, \tag{37}$$

where one may represent

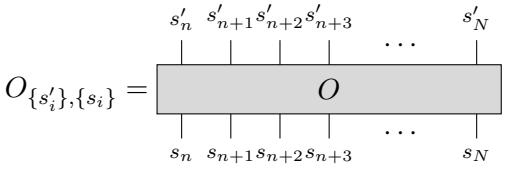

(38)

as tensor. Provided operators are written in the same basis, their action corresponds to the contraction onto the physical degrees of freedom of the state, e.g.,

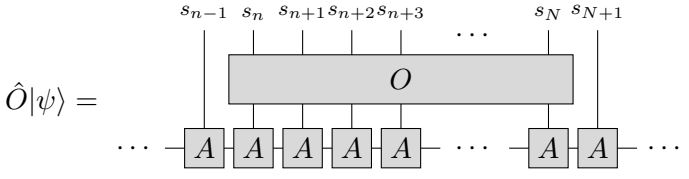

(39)

for $\hat{O}$ acting onto an MPS.

The advantages of this description are manifold:

- On a Hilbert space level, the initial problem has been resolved: PEPS represent a class of variational wave functions that inhabit a small subspace of the full configuration space, namely the space of states with area law.
- Remarkably, in 1D, each local gapped Hamiltonian has an efficient representation in terms of an MPS [79, 80]. Conversely, any MPS is also the ground state of a local and gapped parent Hamiltonian [45]. Similarly, a large class of PEPS is also a ground state to a parent Hamiltonian [51].
- From a practical point of view, the TN description grants access the to local degrees of freedom without the need to resolve the full state. This is employed by a multitude of algorithms like (i)TEBD [81, 82], *Density Matrix Renormalization Group* (DMRG) [83, 84, 85], or calculating the expectation value of local observables.
- In the case of periodic systems, a few tensors (or even just one) can resolve the full state, which offers immense compression capability.
- Tensor network states don't just have the area law and lattice geometry hard-coded into them, but also extra global symmetries can be

encoded evidently, by assuring that the tensors transform under some representation of the associated group [86, 87].

All these aspects and many beyond are worthy of their own treatment; however, in the spirit of conciseness, we ought develop the methods used as we come across them.

Levin-Wen States as TNS

Typically, one finds the PEPS ground state of a parent Hamiltonian through iterative methods; remarkably, however, the Levin-Wen states have a known exact TNS description [52]. In fact, the string-net states can be written as

$$|\Phi\rangle = \prod_P B_P|0\rangle = \prod_P \sum_s a_s B_P^s|0\rangle, \tag{40}$$

where B_P is the known plaquette operator from (11)-(13), and $|0\rangle$ is the vacuum state. This expression can be translated into a tensor network consisting of T-tensors on the vertices and g-tensors on the links of the hexagonal lattice (Fig. 11). Both have triple-line structure; each link carries three indices (Fig. 12).

The tensors $(a_i, v_i, F_{kln}^{ijm})$ previously used to specify the Levin-Wen states are sufficient to define the T- and g-tensors,

$$T_{u'\alpha u;t'\beta t;s'\gamma s} = (a_t a_s a_u)^{\frac{1}{6}} \frac{v_\alpha v_\beta}{v_u} F_{ts^*u}^{\alpha\beta\gamma} \delta_{ut'} \delta_{ts'} \delta_{su'}, \tag{41}$$

$$g^m_{u'_A \alpha_A u_A; u'_B \alpha_B u_B} = \delta_{\alpha_A m} \delta_{\alpha_A \alpha_B^*} \delta_{u_A u'_B} \delta_{u'_A u_B}, \tag{42}$$

where the indices A and B reflect whether the indices belong to sublattice A or B. The g-tensors translate the physical state m to virtual indices. The T-tensor assures that the strings along adjacent plaquettes are recombined correctly along the shared link. The oriented indices contracted along the edges of each plaquette assure a consistent flux s around it and book-keep for the weight a_s associated with that flux. The string-net states are easily expressed through a tensor trace:

$$|\Phi\rangle = \sum_{\{m_l\}} \mathrm{tTr}[\otimes_v T(v) \otimes_l g^{m_l}(l)]|\{m_l\}\rangle. \tag{43}$$

If one wishes for a traditional TN description, it is possible to split the g-tensors while doubling the degrees of freedom on each link to obtain g_A and g_B. These new tensors enforce $m_A = m_B$ for each link to counteract the

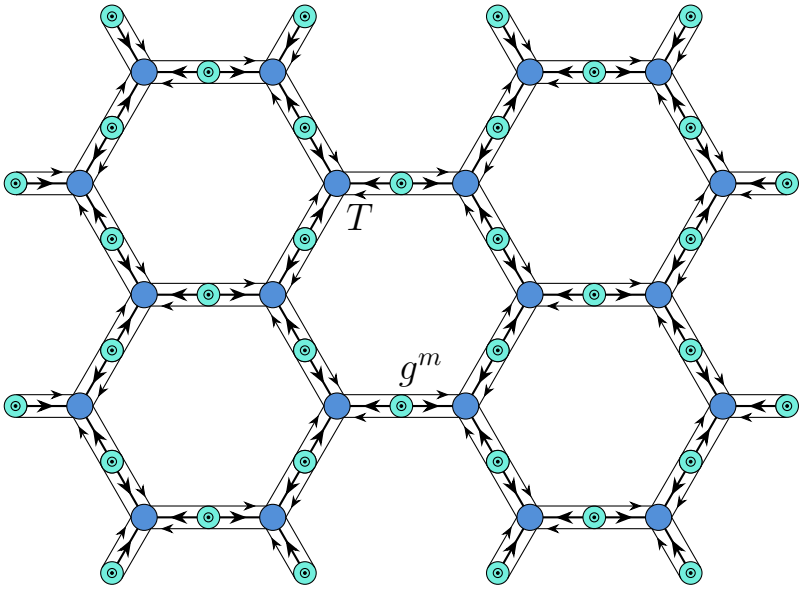

Figure 11: Honeycomb lattice with T-tensors on the vertices, and g-tensors on the links. (Inspired by Fig. 14 in Ref. [52].)

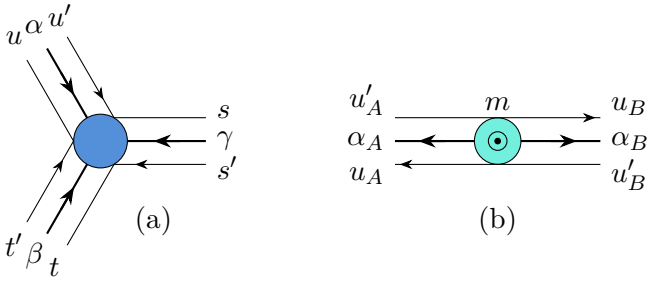

Figure 12: The indiex convention of (a) the T-tensors and (b) the g-tensors. The physical index m (symbolized by $\odot$) points out from the plane spanned by the lattice. Notice the triple-line structure. (Inspired by Fig. 15 in Ref. [52].)

doubling. Contracting the T-tensors with their respective g_A's or g_B's gives

T_A and T_B, respectively;

$$T^{ijk}_{A,u\alpha u';t\beta t';s\gamma s'} = (a_t a_s a_u)^{\frac{1}{6}} \frac{\sqrt{v_i v_j v_k}}{v_\gamma v_u} F^{\alpha\beta\gamma}_{ts^*u} \delta_{ut'} \delta_{ts'} \delta_{su'} \delta_{i\alpha} \delta_{j\beta} \delta_{k\gamma}, \quad (44)$$

$$T^{klm}_{B,u\alpha u';t\beta t';s\gamma s'} = (a_{t'} a_{s'} a_{u'})^{\frac{1}{6}} \frac{\sqrt{v_k v_l v_m}}{v_\gamma v_{u'}} F^{\alpha^*\beta^*\gamma^*}_{t's'^*u'} \delta_{u't} \delta_{t's} \delta_{s'u} \delta_{k\alpha} \delta_{l\beta} \delta_{m\gamma}, \quad (45)$$

which define the string-net state only through tensors located at the vertices of the lattice (see Fig. 13). The new upper indices (i, j, k, l, m) are the physical degrees of freedom absorbed from the contraction with the $g_{A,B}$-tensors.

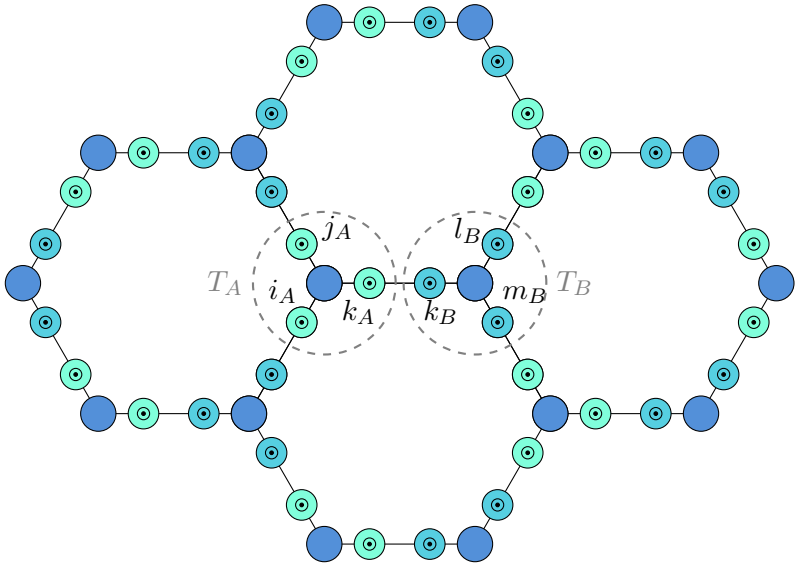

Figure 13: On each link, the g-tensors have been split into g_A and g_B. The standard TPS representation is achieved by assembling the T-tensor with the $g_{A,B}$ that corresponds to its sublattice on each link. (Inspired by Fig. 15 in Ref. [52].)

With all the puzzle pieces set in place, we can now appreciate the complete picture: The string-net paradigm provides a mechanism for topological phase transitions and assures that the area law is manifest in the phases described. Thus, any state can be written efficiently as TNS; moreover, the fixed-point wave functions have exact TN expressions. In addition, signature attributes of topological order, like anyons and the TEE, can be used to describe a phase and are also intrinsic to the string-net picture. Hence, tensor networks

provide the ideal platform to develop efficient numerical methods to study topological phase transitions on 2D lattice gauge theories in the following.

3 Methods and Quantities

The previous chapter suggests that the study of topological phases is straightforward; it should merely suffice to write a family of states that leads across a phase transition as TN states and then compute whichever quantities are of interest. Unfortunately, the exact contraction of 2D tensor networks is exponentially hard in system size, preventing access to large systems and the thermodynamic limit. In the following, we will develop an efficient approach based on boundary states alongside an accessible set of quantities that is sufficient to resolve topology and phase transitions. The MPS structure of the boundary states is viable to contract even in large systems.

Although our treatment of TNSs seeks to be general, two requirements must be set before we can develop our methods: The TN representation

- must be translation invariant;
- can be mapped onto a square lattice (Fig. 14c).

Luckily, translation invariance is manifest in the string-net picture: the states

determined in [42] are emblematic of their topological phase and originate from an RG argument that eliminates any local and non-topological contributions. As the rules specifying the string-net structure are local and defined identically across the whole system, the string-net states have to look alike everywhere. (A similar RG argument can probably be extended to a much larger set of TPs.) After all, treating translation invariant primarily TNs is common and considered good practice [50]. Importantly, translation invariance sets a limit as to what deformations of the GS (that drives the phase transition) we can hope to describe, as the deformation too must respect the translation invariance.

Most common lattices can be reshaped into a square lattice; specifically, the honeycomb lattice and the triangular lattice (Fig. 14b) are mapped as shown by Fig. 15. These processes are general, although they require extra care in the presence of physical indices that need to be tucked into a single multi-site physical index per tensor. This, however, will not be necessary in the following, as any TN contraction relevant to us will get rid of the physical indices ahead of this mapping.

Conjointly, these properties allow us to characterize any TNS of interest through a single rank-5 tensor T^s_{udlr}, with physical index s and imaginary indices u, d, l, and r, one for each link on the square lattice. This is a key property we will use in the development of our numerical methods.

With these general conditions set, we can now discuss the central object of our method.

3.1 Reduced Density Matrix

Despite knowing the TN representation of any state that may interest us, the state itself is not the most advantageous object to determine certain quantities like the entanglement entropy. Departing from the state itself would require either realizing the Schmidt decomposition for a matrix growing exponentially with the system size, or tracing out exponentially many partial states. A much more favorable object is the *Reduced Density Matrix* (RDM) ρ_A (or ρ_B) with respect to a bipartition of the system into sub-systems A and B.

For a translation invariant TN, the RDM can be constructed very easily. Consider a system of rectangular shape with arbitrary length and width.

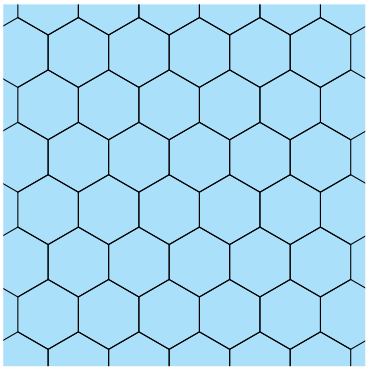

(a) Honeycomb lattice.

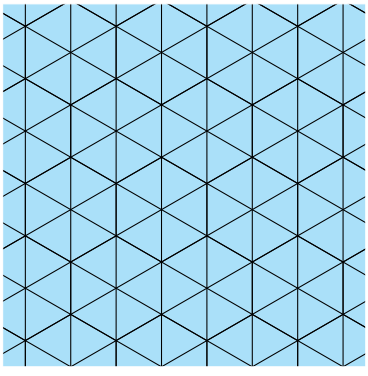

(b) Triangular lattice.

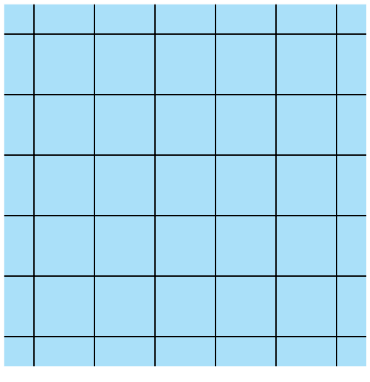

(c) Square lattice.

Figure 14: The honeycomb, triangular, and square lattice will be the three lattices considered in this work.

A square lattice offers two partitioning choices with respect to its lattice geometry, as displayed in Fig. 16.

Proposition 1. *On a translation invariant square TN, each way to partition*

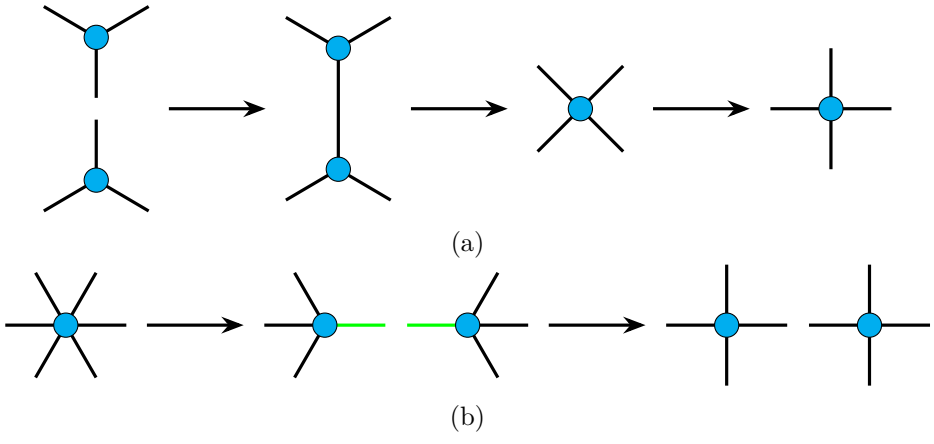

Figure 15: (a) On the honeycomb lattice, all rank-3 tensors inhabiting distinct sub-lattices are contracted with another across their vertical link, the resulting TN of rank-4 tensors is a rotation away from the square lattice. (b) The rank-6 tensors that constituate the triangular lattice can be decomposed into two rank-4 tensors through a *Singular Value Decomposition* (SVD), giving rise to the additional green indices. The resulting lattice is square.

(as displayed in Fig. 16) gives for the traced out region a TN contraction, that can be interpreted as a repeated multiplication of a transfer matrix Θ*.*

Proof. Each way to partition (according to Fig. 16) looks microscopically as displayed in Fig. 17. Clearly, by wrapping up the links in y-direction into the boundary condition, and collecting the links in x-direction into a single index for upper-left, upper-right, lower-left, and lower-right, one can identify:

$$\Theta^{\alpha\alpha'}_{\beta\beta'} = \begin{matrix}\alpha & \alpha' \\ \beta & \beta'\end{matrix} = \tag{46}$$

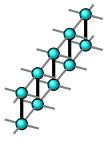

$$\Theta^{\alpha\alpha'}_{\beta\beta'} = \begin{matrix}\alpha & \alpha' \\ \beta & \beta'\end{matrix} = \tag{47}$$

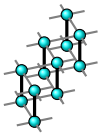

In particular, $\Theta^{\alpha\alpha'}_{\beta\beta'}$ can be interpreted as a transfer matrix (viewing $\alpha\beta$ and $\alpha'\beta'$ as single indices each) due to the translation invariance. □

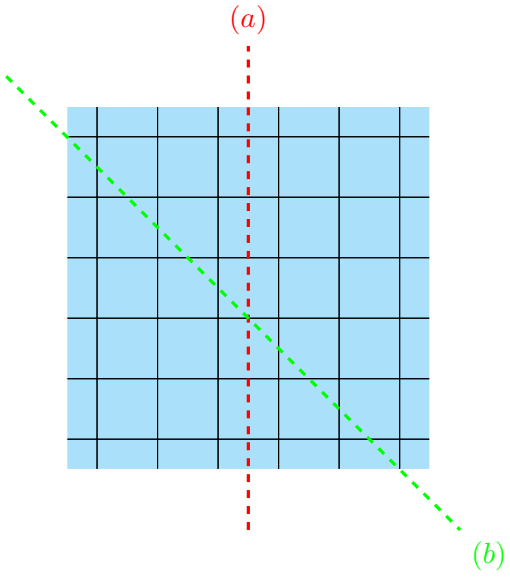

Figure 16: Two possible ways to partition the square lattice with respect to its geometry.

Theorem 1. *The reduced density matrix of subsystem A (with respect to a partition of the system into subsystems A and B) encoded by a translation invariant TN state is (up to an isometry) given by*

$$\rho_A \propto \sqrt{L^T} R \sqrt{L^T}, \tag{48}$$

in the limit of a very large system. L and R are the left and right dominant eigenvectors of the transfer matrix above, respectively.

Proof. Suppose a rectangular system of arbitrary but large dimensions that is partitioned into two regions, A and B, according to either of the partitions highlighted in Fig. 16. The state of the system across the partition can be written in TN language

$$|\psi\rangle = \sum_{\alpha,\{s_i\},\{s_j\}} \mathrm{tTr}\left[\otimes_i T^{s_i}\right]^A_\alpha \mathrm{tTr}\left[\otimes_j T^{s_j}\right]^B_\alpha |\{s_i\}\rangle_A \otimes |\{s_j\}\rangle_B, \tag{49}$$

where $\{s_i\}$, $\{s_j\}$ are the physical indices embedded in regions A and B, respectively. The tensor traces contract over all virtual indices internal to their

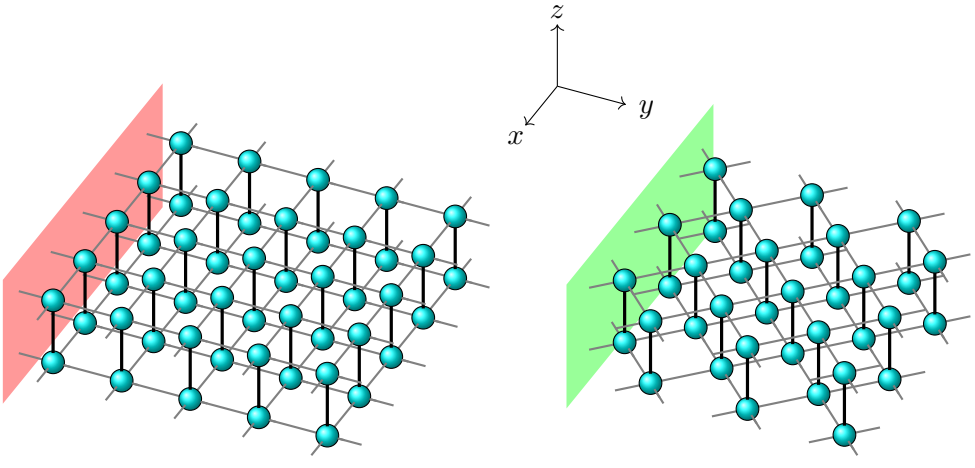

(a) (b)

Figure 17: Exact visualization of the double-layer TN in the traced out region next to the partition (in red resp. green) for choices (a) and (b) from above. The gray links in the xy-plane are virtual, the thick links in z-direction are traced over and physical.

respective region, and α is the accumulation of all virtual indices that cross from A into B. Each of the tensor traces can be viewed as a large matrix and represented graphically through

$$\mathcal{A}_{\alpha,\{s_i\}} = \mathrm{tTr}\left[\otimes_i T^{s_i}\right]^A_\alpha = \overbrace{}^{\{s_i\}} \alpha \ , \tag{50}$$

$$\mathcal{B}_{\alpha,\{s_j\}} = \mathrm{tTr}\left[\otimes_j T^{s_j}\right]^B_\alpha = \alpha \overbrace{}^{\{s_j\}} . \tag{51}$$

So that the reduced density matrix takes the elegant form

$$\rho_A = \mathrm{Tr}_B\left[|\psi\rangle\langle\psi|\right] = \sum_{\alpha,\alpha',\{s_j\}} \mathcal{A}_{\alpha,\{s_i\}} \mathcal{B}_{\alpha,\{s_j\}} \mathcal{B}^*_{\alpha',\{s_j\}} \mathcal{A}^*_{\alpha',\{s'_i\}} \tag{52}$$

$$= \tag{53}$$

Notice that the traced-out part of the TN, i.e., region B, corresponds to

the transfer matrix acting repeatedly onto the right boundary of the system, which - for now - we need not specify:

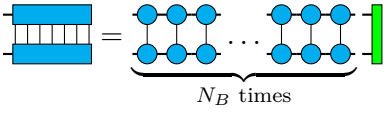

$$= \Theta^{N_B} v_{\mathcal{R}} \tag{54}$$

The green tensor represents the right boundary $v_{\mathcal{R}}$, region B is N_B transfer matrices wide. A priori, we have no guarantee that the transfer matrix is normal and that the left and right eigenvectors are identical, so that, for now, we have to distinguish between the two. In the limit of a large system, the repeated action of the transfer matrix is identical to the projection onto the right eigenspace $\mathcal{R}_0$ of the maximal eigenvalue λ_0 of the transfer matrix up to exponentially suppressed corrections:

$$\Theta^{N_B} v_{\mathcal{R}} = \lambda_0^{N_B} \left[\mathrm{P}(\mathcal{R}_0) + \left(\left(\frac{\lambda_1}{\lambda_0} \right)^{N_B} \right) \right] v_{\mathcal{R}} \overset{\text{large } N_B}{\to} \lambda_0^{N_B} \mathrm{P}(\mathcal{R}_0) v_{\mathcal{R}} = R, \tag{55}$$

λ_1 being the second largest eigenvalue of Θ, and $\mathrm{P}(\mathcal{R}_0)$ the projector onto $\mathcal{R}_0$. This statement leads to the conclusion that

$$\mathcal{B}\mathcal{B}^\dagger \propto R \tag{56}$$

up to exponentially suppressed terms. Clearly R must be Hermitian and

$$\mathcal{B} \propto \sqrt{R} U, \tag{57}$$

U being an isometry, we need not specify.

An identical line of arguments on region A with left boundary $v_{\mathcal{L}}$ allows to conclude

$$\mathcal{A}\mathcal{A}^\dagger \propto L = \lambda_0^{N_A} v_{\mathcal{L}} \mathrm{P}(\mathcal{L}_0), \tag{58}$$

$\mathrm{P}(\mathcal{L}_0)$ is now the projector onto the left eigenspace $\mathcal{L}_0$ of λ_0. L is Hermitian and up to an isometry

$$\mathcal{A} \propto \sqrt{L} U^T. \tag{59}$$

From the above discussion, we can conclude the statement of the theorem

$$\rho_A = \mathcal{A}^T \mathcal{B}\mathcal{B}^\dagger \mathcal{A}^* \propto U \sqrt{L^T} R \sqrt{L^T} U^\dagger \tag{60}$$

up to an isometry. □

Remark 1. To exactly define the RDM, one would also need to specify the isometry in (60), the role of which is to relate $\sqrt{L^T}R\sqrt{L^T}$ written in terms of virtual indices to the RDM expressed in terms of physical indices. Nonetheless, we can ignore U as any quantities we are interested in can either be expressed through traces over products of the RDM (e.g. Rényi entropies) or through direct calculation of observables in the space of virtual indices, for which L and R are sufficient. In fact, getting rid of the isometry is crucial in rendering any calculations in the following efficient: U relates the exact RDM that grows exponentially with the bulk of the system to $\sqrt{L^T}R\sqrt{L^T}$ that grows exponentially with the length of the partition of the system.

Relating information in the bulk to a boundary object - as Theorem 1 does - reflects the bulk boundary-correspondence, a direct consequence of the area law, which states that information in a region grows with its boundary. Notably, this holographic principle and theorem is well understood and explored for TNSs and goes back to Cirac et al. [58].

Remark 2. There is no guarantee that the transfer matrix has exactly one dominant vector, so it is partially a misnomer to talk of "the" dominant vector in Theorem 1. What we actually mean is the dominant vector selected by a specified boundary condition, i.e., projecting the left and right boundary onto the left and right eigenspace, respectively. The physical choice of boundary is insignificant when looking at large systems and topological properties. However, in the case of TN constructions in which physical links aren't just projected into the space of virtual links, extra care must be taken to construct a valid boundary in the virtual space.

Corollary 1. *If $L^T = R$, then*

$$\sqrt{\rho_A} \propto R. \tag{61}$$

Proof. Trivially

$$\rho_A \propto R^2 \Rightarrow \sqrt{\rho_A} \propto R. \tag{62}$$

□

The discussion in Remark 1 legitimizes thinking of the RDM as the state of a 1D system; moreover, the proof of Theorem 1 proposes a straightforward way to construct it: Acting sufficiently many times with the transfer matrix onto a given boundary choice will generate the dominant vectors L and R.

In particular, choosing a square lattice geometry and partition choice (b), we may formulate that procedure as an iTEBD-type algorithm acting on an infinite MPS.

The iTEBD Algorithm and Dominant Vectors

The *Time-Evolving Block-Decimation* (TEBD) algorithm - fathered by Vidal in 2003 - was constructed as an efficient classical algorithm to simulate quantum computations on a multipartite system, provided the classical correlation or entanglement is proficiently restricted [81]. MPSs, following the area law, naturally form a class of states with restricted entanglement. As such, MPSs form the perfect vehicle to host the TEBD algorithm to simulate general time evolution on a 1D quantum state. Notably, Vidal adapted TEBD into the *infinite TEBD* (iTEBD) algorithm operating in the limit of an infinite lattice [82]. Running iTEBD in imaginary time allows for calculating the ground state $|\mathrm{GS}\rangle$ of the Hamiltonian H at the origin of the (imaginary) time evolution [88]. In essence, imaginary iTEBD calculates for large imaginary time τ

$$\frac{e^{-\tau H}|\psi\rangle}{||e^{-\tau H}|\psi\rangle||} \overset{\tau\to+\infty}{\to} |\mathrm{GS}\rangle, \tag{63}$$

as long as $|\psi\rangle$ is not orthogonal to the GS eigenspace. iTEBD is, however, much more powerful: the GS calculation is merely a special case of finding the maximal eigenvector of an operator. As such, iTEBD has been used to find the dominant vector of 2D translation invariant TNs to construct partition functions [88], and as such, iTEBD will serve us to construct the reduced density matrix.

One restriction of the (i)TEBD algorithm is that the Hamiltonian must be under local block form

$$H = \sum_n h_n(k), \tag{64}$$

consisting of n blocks each acting on k neighboring physical links at most. Partition choice (b) will exactly impose this block form onto the TN by defining the (double-layer) blocks Z through the contraction of the local tensor with its conjugate over the physical index

$$\mathrm{Z}_{ijkl} = \quad = \sum_s T^s_{udlr} T^{s*}_{\tilde{u}\tilde{d}\tilde{l}\tilde{r}}, \tag{65}$$

where the upper and lower indices have been conjoined into one ($i = u\tilde{u}, j = l\tilde{l}, k = r\tilde{r}, l = d\tilde{d}$). This recasts the action of the transfer matrix directly as iTEBD acting onto the boundary written as (infinite) MPS, as shown in Fig. 18. One may argue that the Z-tensors could be related to a Hamiltonian

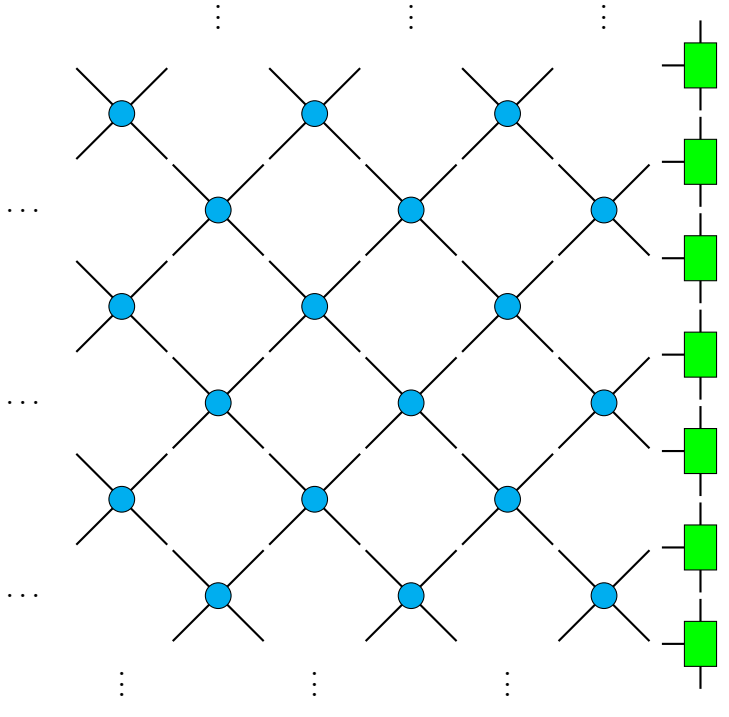

Figure 18: The repeated action of the transfer matrix takes the form of Z-tensors acting in iTEBD fashion onto the boundary state, written as infinite MPS (represented in green).

through

$$\mathrm{Z} = e^{-\mathrm{d}\tau h} \tag{66}$$

for an arbitrarily small yet finite flow of imaginary time $\mathrm{d}\tau$. The role of the "physical" indices of the MPS is now being played by the virtual indices of the Z-tensor, the dimension of the virtual links d of Z is equal to the local "physical" degree of freedom of the dominant vector.

Given the translation invariance, one can construct the dominant vector as an infinite MPS in canonical form, which requires defining four tensors

to properly perform the iTEBD update steps represented in Fig. 19. The two tensors $\mathrm{S}^A, \mathrm{S}^B$ contain the singular values while $\mathrm{V}^A, \mathrm{V}^B$ carry the local physical index. One application of the transfer matrix across the infinite chain requires two iTEBD steps, switching the order of A and B tensors in between. To prevent the virtual dimension of the MPS from steadily growing through consecutive iTEBD steps increasing the complexity of each update, we can compress the MPS by truncating all but the χ largest Schmidt coefficients. Since the MPS is the GS of a local and gapped "Hamiltonian", it also follows the area law, and the compression is efficient. Nonetheless, χ sets a first constraint on the accuracy with which the dominant vector is determined. One iTEBD update takes $O(d^2\chi^2)$ space and has complexity $O(d^3\chi^3)$ [82].

From the above development, we can formulate an algorithm to construct the left and right dominant vectors:

1. Assemble the Z-tensor.
2. Map the Z-tensor onto the geometry of a square lattice.
3. Construct the boundary MPS by translating a boundary state into the virtual space. A straightforward and efficient choice is a boundary without string-nets (e.g., all +1 spins on the Toric Code), assuring the boundary doesn't contain anyonic charges.
4. Perform $2N$ steps of iTEBD truncating the Schmidt coefficients and exchanging A and B tensors in between each update. This corresponds to N transfer matrices.

N sets a second constraint on the accuracy of the dominant vector, although not as strict due to the exponential suppression of any non-dominant component of the boundary. The algorithm requires $O(d^2\chi^2)$ space and has complexity $O(d^3\chi^3 N)$.

Remark 3. Naively, partition choice (a) could conceive a similar but less efficient algorithm with complexity $O(d^6\chi^3 N)$ that would also require intermediate update steps to recover the canonical form of the MPS. The Variational Uniform Matrix Product State (VUMPS) algorithm [89] is appropriate to deal with choice (a) at the same the complexity as the iTEBD. Depending on the lattice geometry and on the symmetries of the Z-tensor, this choice can have advantages. For instance, if one wishes to enforce the transfer matrix to be Hermitian in an attempt to make Corollary 1 hold.

Accessing the information of a 2D topological state through an infinite

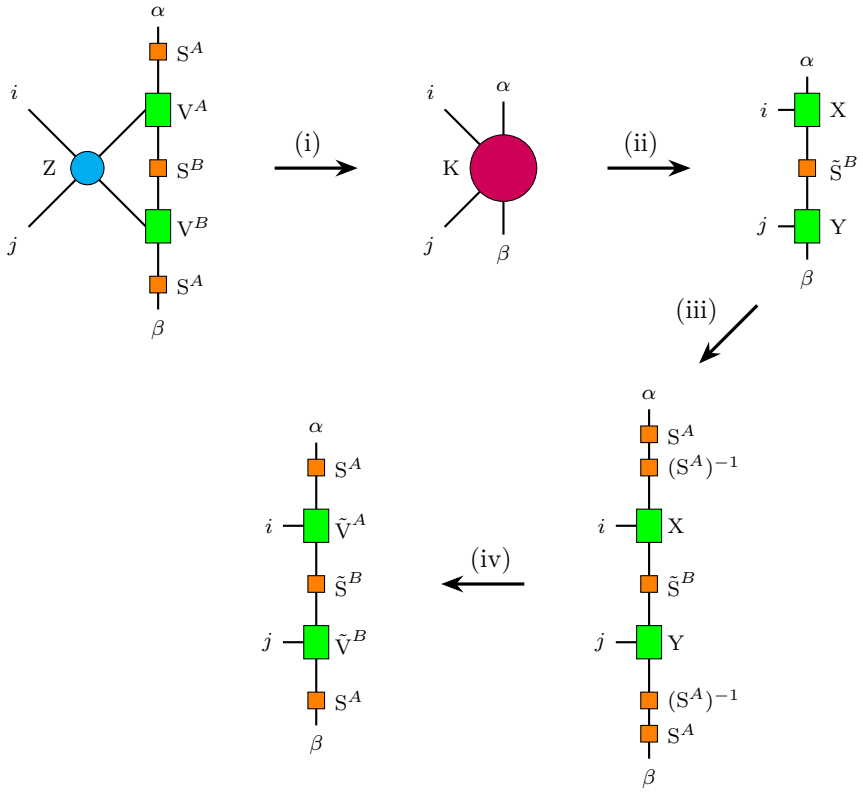

Figure 19: (i) The Z-tensor is contracted with the physical indices of the MPS into the K-tensor. (ii) A SVD is performed (viewing $i\alpha$ and $j\beta$ as single indices each) to rewrite the K-tensor as $\mathrm{K}_{i\alpha;j\beta} = \sum_k \mathrm{X}_{i\alpha;k}\tilde{\mathrm{S}}^B_k\mathrm{Y}_{k;j\beta}$. Normalize the state by enforcing $||\tilde{\mathrm{S}}^B|| = 1$. (iii) The canonical form is restored by inserting $\mathrm{S}^A(\mathrm{S}^A)^{-1} = (\mathrm{S}^A)^{-1}\mathrm{S}^A = \mathbb{1}$. (iv) Absorbing $(\mathrm{S}^A)^{-1}$ into X resp. Y gives the tilted tensors that correspond to the updated MPS. The updated state can be compressed by only holding onto the χ largest Schmidt coefficients of $\tilde{\mathrm{S}}^B$.

MPS has numerous advantages:

- The translation invariance implies that the MPS can be wrapped, through periodic boundary conditions, into a system of any size. This results in a straightforward pathway to the topological entanglement entropy and to extending results and quantities to their behavior in the thermodynamic limit.
- Contractions on a 1D MPS are much more computationally efficient than contractions on a 2D TN, especially for large system sizes.
- The MPS form grants access to characterizations of phase transitions that are only feasible or much more efficiently obtained in 1D, like finite-size scaling.

In the following, we will develop a set of quantities to fully characterize topological phase transitions, which are efficiently accessed just through the knowledge about the dominant vectors.

3.2 Topological Entanglement Entropy

The topological entanglement entropy S^{topo} for a state that follows the area law is a sub-leading term to the von Neumann entropy

$$S = -\text{Tr}\left[\rho_A \ln(\rho_A)\right] = -\left[\rho_B \ln(\rho_B)\right] = \zeta L - S^{\text{topo}}, \tag{67}$$

where L is the length of the bi-partition of the system into A and B. The von Neumann entropy is, however, just a special case of the family of Rényi entropies R_α that generalizes the notion of entropy beyond the Shannon picture [90]. They all follow the area law

$$R_\alpha = \frac{1}{1-\alpha} \ln\left(\text{Tr}[\rho_A^\alpha]\right) = \frac{1}{1-\alpha} \ln\left(\text{Tr}[\rho_B^\alpha]\right) = \zeta_\alpha L - S_\alpha^{\text{topo}} \tag{68}$$

for $\alpha \in \mathbb{R}^+ \setminus \{1\}$. The von Neumann entropy is recovered in the limit

$$S = \lim_{\alpha \to 1} R_\alpha, \tag{69}$$

$$S^{\text{topo}} = \lim_{\alpha \to 1} S_\alpha^{\text{topo}}. \tag{70}$$

This allows us to obtain a topological invariant S_α^{topo} from whichever Rényi entropy is most efficient to compute or of specific interest. It is forthcoming that for the vast set of non-chiral topological phases, the topological contribution to any of the Rényi entropies is identical to that of the von Neumann entropy [91]. Nonetheless, in the service of generality and as numerical results may possibly lead to varying results between the orders, we will explicitly distinguish the different Rényi entropies.

Notably, all of the Rényi entropies can be brought back to a trace over the RDM to a power; this is even true for the von Neumann entropy if we content ourselves with expanding it to a finite order. More importantly, since the RDM is periodic, any trace takes the form as shown in Fig. 20 and can be constructed at any length L. Linear regression allows us to determine the topological entanglement entropy. As we want to take a large L, the contraction is most efficient if one first contracts along the "physical" indices, the complexity of contracting the virtual indices grows as $O(L\chi^{3\alpha})$, so that the smallest possible choice of χ and more importantly α should be made.

Proposition 2. *The row of n contracted* X*-tensors in Fig.20 can be viewed as a matrix X_α, and*

$$\mathrm{Tr}[\rho_A^\alpha] \propto \mathrm{Tr}\left[\mathrm{X}_\alpha^{L/2}\right]. \tag{72}$$

Lemma 1. *The area law of any Rényi entropy R_α for a large system is entirely ruled by the maximal eigenvalues of X_α and X_1 and their multiplicity. Specifically*

$$\zeta_\alpha = \frac{1}{2}\frac{1}{1-\alpha}\left[\ln(\lambda_{\alpha,0}) - \alpha\ln(\lambda_{1,0})\right], \tag{73}$$

$$S_\alpha^{\text{topo}} = -\frac{1}{1-\alpha}\left[\ln(m_{\alpha,0}) - \alpha\ln(m_{1,0})\right], \tag{74}$$

where $\lambda_{\alpha,0}, \lambda_{1,0}$ are the maximal eigenvalues with multiplicity $m_{\alpha,0}, m_{1,0}$ of $\mathrm{X}_\alpha, \mathrm{X}_1$, respectively.

Proof. The Rényi entropy of order α for a partition of length L can be written as

$$R_\alpha = \frac{1}{1-\alpha}\ln\left(\mathrm{Tr}[\rho_A^\alpha]\right) = \frac{1}{1-\alpha}\ln\left(\mathrm{Tr}\left[\frac{\mathrm{X}_\alpha^{L/2}}{\mathrm{Tr}\left[\mathrm{X}_1^{L/2}\right]^\alpha}\right]\right), \tag{75}$$

where the denominator enforces that the encoded RDM has unit trace. In terms of decreasingly ordered eigenvalues $\{\lambda_{\alpha,i}\}$, $\{\lambda_{1,j}\}$ of $\mathrm{X}_\alpha, \mathrm{X}_1$ and their

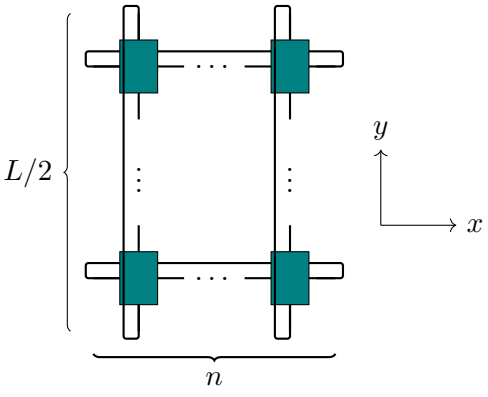

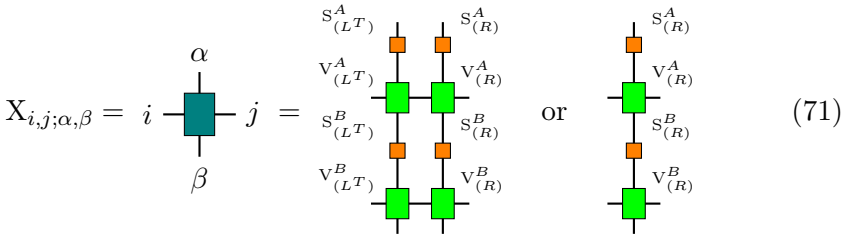

(71)

Figure 20: Imposing periodic boundary conditions on the MPS recasts $\mathrm{Tr}[\rho_A^\alpha]$ as the contraction of a translation invariant tensor network on a torus, where the virtual indices lie in y-direction and the "physical" indices of the RDM in x-direction. In the general case, the X-tensor corresponds to the contraction of the tensors constituting the left and right dominant vector (first choice in equation (71) and the trace for any integer order can be found by setting $n = \alpha$. In the special case that Corollary 1 holds, also traces of half-integer order can be found with the second choice in equation (71) and $n = 2\alpha$. Notice that the indices of the dominant vectors and thus of the V-tensors have been separated in order to write L and R as matrices.

respective multiplicities $\{m_{\alpha,i}\}$, $\{m_{1,j}\}$ this becomes:

$$R_\alpha = \frac{1}{1-\alpha}\left[\ln\left(\sum_i m_{\alpha,i}\lambda_{\alpha,i}^{L/2}\right) - \alpha\ln\left(\sum_j m_{1,j}\lambda_{1,j}^{L/2}\right)\right] \tag{76}$$

In the large L limit, the non-maximal eigenvalue contributions are exponential

suppressed, and one recovers the area law

$$R_\alpha \overset{\text{large } L}{\to} \frac{1}{1-\alpha}\frac{1}{2}\left[\ln(\lambda_{\alpha,0}) - \alpha\ln(\lambda_{1,0})\right] L + \frac{1}{1-\alpha}\left[\ln(m_{\alpha,0}) - \alpha\ln(m_{1,0})\right] \quad (77)$$

from which one can easily read off the statement of the lemma. □

Evidently, it is a nice sanity check to see the area law hard-coded so plainly into the above development; however, Lemma 1 comes with deeper insights.

Remark 4. The contraction of the TN in Fig. 20 can be brought back to an eigenvalue problem, which, depending on how large L is, can be computed much more efficiently. In particular, as only the largest few eigenvalues are of interest, run times can be accelerated even further employing a technique that only seeks the k largest eigenvalues of a large matrix (e.g., a Lanczos-type algorithm).

Remark 5. The topological entanglement entropy is naturally quantized as the multiplicities are. The entropy can be found exactly for any phase that has a quantum dimension that is a root of a rational number. However, for any systems with a quantum dimension that is irrational and that cannot be expressed as the root of a fraction, we can only hope to approach the true value through fractions (we will see an example when studying the Double Fibonacci model). A topological phase transition directly corresponds to a jump in the multiplicity of maximal eigenvalues.

Remark 6. Lemma 1 directly extrapolates the validity of any results to the thermodynamic limit.

3.3 Reduced Fidelity

Conceptually appropriated from Quantum Information Theory, *fidelity* generalizes the notion of likeness of states to mixed states [92].

Definition 1. Let be ρ, σ two density matrices, then their fidelity is given by

$$F(\rho,\sigma) = \left(\mathrm{Tr}\left[\sqrt{\sqrt{\sigma}\rho\sqrt{\sigma}}\right]\right)^2, \quad (78)$$

with $0 \leq F(\rho,\sigma) \leq 1$ and $F(\rho,\rho) = 1$.

The use of the fidelity for quantum phase transitions was pioneered by Quan et al. [93] and has grown into a commonplace approach [94]. Heuristically, the likeness of states behaves for a ground state $\rho(\eta)$ driven by a Hamiltonian $H(\eta)$ through a phase transition in η_c as follows: Far from the critical point, small changes in the control parameter $\delta\eta$ merely correspond to a small perturbation on the state level, and one can reasonably assume the fidelity to almost equal 1. However, close to η_c the state undergoes a (possibly avoided) level crossing - the state transforms rapidly into a state orthogonal to itself, and the perturbation can no longer be deemed small

$$F\left(\rho(\eta), \rho(\eta+\delta\eta)\right) \begin{cases} \approx 1 & \text{far from } \eta_c \\ \ll 1 & \text{close to } \eta_c \end{cases}. \tag{79}$$

This notion turns rigorous if we expand the fidelity perturbatively in η and sort the eigenenergies $\{E_n\}$ increasingly [94]

$$F\left(\rho(\eta), \rho(\eta+\delta\eta)\right) = 1 - \delta\eta^2 \sum_{n\neq 0} \frac{c_n(\eta)^2}{\left[E_n(\eta) - E_0(\eta)\right]^2} + \ldots, \tag{80}$$

where c_n is the hopping matrix element (with respect to the instantaneous Hamiltonian) of the 0th eigenstate to the nth eigenstate. At the phase transition the gap closes, the quadratic coefficient blows up, and even minuscule shifts $\delta\eta$ lead to a considerable reduction (dip) in fidelity (see Fig. 21). The fidelity approach has a noteworthy advantage, it relies merely on the quantum information perspective, it knows nothing of symmetry breaking nor of local order parameters. As such, it is equally well applicable to phase transitions that follow the Ginzburg-Landau picture as to topological phase transitions.

In order to obtain a relevant fidelity efficiently, consider the trace shown in Fig. 22.

Proposition 3. *The contraction in Fig. 22 is identical to the scalar product* $\langle R_2|R_1\rangle$ *of the dominant vectors* R_1 *and* R_2 *with a system partition of length* $L/2$*. Moreover*

$$\langle R_2|R_1\rangle = \mathrm{Tr}[\mathrm{X}'(R_1,R_2)^{L/2}], \text{ where } \mathrm{X}'_{\alpha,\beta}(R_1,R_2) = \sum_i \tilde{\mathrm{X}}_{i,i;\alpha,\beta}(R_1,R_2). \tag{82}$$

Proof. Writing R_1 and R_2 in matrix form leads to

$$\langle R_2|R_1\rangle = \mathrm{Tr}[R_2^\dagger R_1] = \mathrm{Tr}[R_2 R_1], \tag{83}$$

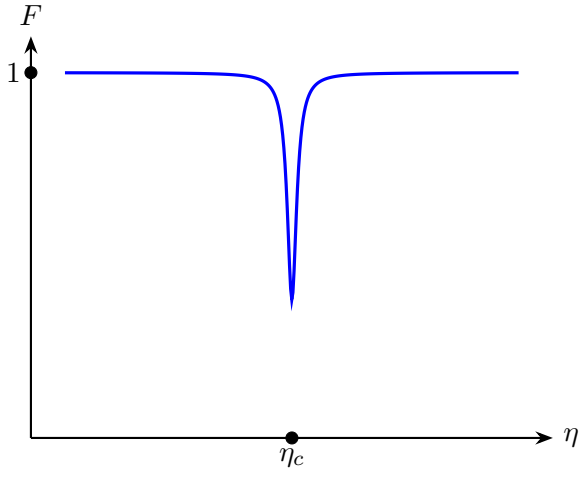

Figure 21: The fidelity approaches unity far from the phase transition; at criticality, it dips sharply and reaches a minimum exactly at the critical point.

where the second equality follows from the self-adjointness of R_1, R_2. $\mathrm{Tr}[R_2 R_1]$ is the above contraction, contracting the horizontal indices gives equation (82). □

Lemma 2. *The fidelity of R_1 with R_2 is given by*

$$F(R_1, R_2) = \frac{\left|\mathrm{Tr}[\mathrm{X}'(R_1, R_2)^{L/2}]\right|^2}{\mathrm{Tr}[\mathrm{X}'(R_1, R_1)^{L/2}]\mathrm{Tr}[\mathrm{X}'(R_2, R_2)^{L/2}]} \tag{84}$$

Proof. Normalizing the dominant vectors and using that $\rho_{1,2} = |R_{1,2}\rangle\langle R_{1,2}|$ for pure states, the fidelity becomes

$$F(R_1, R_2) = \left(\mathrm{Tr}\left[\sqrt{\frac{|R_1\rangle\langle R_1||R_2\rangle\langle R_2|}{\langle R_1|R_1\rangle\langle R_2|R_2\rangle}}\right]\right)^2 = \frac{|\langle R_1|R_2\rangle|^2}{\langle R_1|R_1\rangle\langle R_2|R_2\rangle} \tag{85}$$

The statement is obtained by identifying the scalar products using Prop. 3. □

In the first consideration, the fidelity of the dominant vectors may seem unrelated to the fidelity of the 2D TN states for which we actually wish to visualize the phase transition. The holographic principle proven in Theorem 1 however asserts, that all the information that is stored in the bulk of region

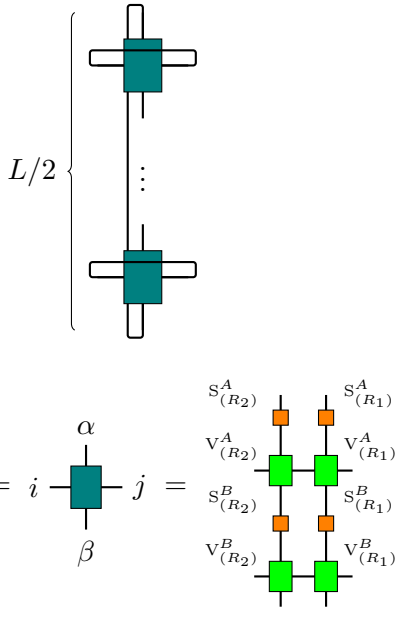

$$\tilde{\mathrm{X}}_{i,j;\alpha,\beta}(R_1,R_2) = \quad = \tag{81}$$

Figure 22: In this contraction (analogous to Fig. 20) R_1 and R_2 are the right-dominant vectors of possibly distinct transfer matrices. Starting the contraction with the horizontal indices leaves the vertical contraction at a complexity $O(L\chi^6)$. Here again, the indices of the dominant vectors and thus of the V-tensors have been spliced in order to write L and R as matrices.

A of the 2-D TN states can be accessed through the dominant vectors L and R. Fidelity is information-based, and as such a rapid change in ρ_A must correspond to a rapid change in R and L, the fidelity of the dominant vectors must be emblematic for the one of the RDMs. Notice that we only have efficient access to the RDM or a quantity representative of it, so that what we are actually dealing with is the reduced fidelity. The reduced fidelity approach has been used [95] and formalized [96], and will behave identically to what we expect from the fidelity. Remarkably, a special case renders the correspondence between RDM and dominant vector information exact:

Corollary 2. *Let be R_1, R_2 two dominant vectors s.t. Corollary 1 holds and $[R_1, R_2] = 0$, then*

$$F(\rho_{1_A}, \rho_{2_A}) = F(R_1, R_2). \tag{86}$$

Proof. Corollary 1 allows to write

$$F(\rho_{1_A},\rho_{2_A}) = \left(\mathrm{Tr}\left[\sqrt{\sqrt{\rho_{1_A}}\rho_{2_A}\sqrt{\rho_{1_A}}}\right]\right)^2 = \frac{\left(\mathrm{Tr}\left[\sqrt{R_1R_2^2R_1}\right]\right)^2}{\mathrm{Tr}[R_1^2]\mathrm{Tr}[R_2^2]}, \tag{87}$$

where the denominator again assures normalization. Using the commutation of R_1 and R_2 the proves the statement

$$\begin{aligned} F(\rho_{1_A},\rho_{2_A}) &= \frac{\left(\mathrm{Tr}\left[\sqrt{R_1^2R_2^2}\right]\right)^2}{\mathrm{Tr}[R_1^2]\mathrm{Tr}[R_2^2]} && (88)\\ &= \frac{\left(\mathrm{Tr}\left[R_1R_2\right]\right)^2}{\mathrm{Tr}[R_1^2]\mathrm{Tr}[R_2^2]} && (89)\\ &= F(R_1,R_2), && (90) \end{aligned}$$

where in the second equality we used $\sqrt{AB} = \sqrt{A}\sqrt{B}$ if $[A,B]=0$. □

Remark 7. The fidelity can be brought back to a contraction that mirrors the properties of the contraction in Fig. 20 so that one can draw a similar conclusions: Only the few largest eigenvalues of $\mathrm{X}'(R_1,R_2), \mathrm{X}'(R_1,R_1)$, and $\mathrm{X}'(R_2,R_2)$ are relevant, allowing to accelerate numerics and to extend results to the thermodynamic limit.

Conjecture: 2D to 1D phase transition correspondence

Consider seriously equation (66), which suggests that $R(\eta)$ is the ground state of a 1D next-neighbor Hamiltonian

$$H_{1D}(\eta) \propto -\sum_k \ln[\mathrm{Z}(\eta)]_{k,k+1}. \tag{91}$$

If Corollary 2 holds, this 1D GS has the same fidelity across the phase transition as the 2D topological state $|\psi(\eta)\rangle$ at the origin of the Z-tensors driven through the 2D Hamiltonian $H_{2D}(\eta)$. Beyond the critical point, the fidelity also encodes knowledge of the universality class of the phase transition that can be extracted through finite scaling [94]. This consideration reasonably suggests a direct correspondence of an identical phase transition on a 2D system and on a 1D system. Clearly, this result is interwoven with the holographic principle, possibly some type of bulk-boundary correspondence. How deep (or shallow) this connection is, or whether it holds beyond Corollary 2, are intriguing questions that, however, lie beyond the scope of this

work. Nonetheless, this seems like a neat conjecture that should be mentioned. Schuch et al. have studied similar considerations through the lense of boundary state Hamiltonians [53].

3.4 Fredenhagen-Marcu Order Parameter

Topological phase transitions cannot be characterized through the spontaneous breaking of a symmetry of the model, such that local order parameters are inadequate to resolve the transition. Nonetheless, one can conceive observables that reveal whether a system is in a topological phase, notably through whether the system can host anyons. A candidate operator is the Wilson line $\mathcal{W}$, which creates an anyon anti-anyon pair when it acts on a topologically ordered ground state. Consider a parametrized ground state $|\psi(\eta)\rangle$ that undergoes a topological phase transition. Within the topological phase the expectation value

$$\langle\psi(\eta)|\mathcal{W}|\psi(\eta)\rangle \tag{92}$$

must be null, as $\mathcal{W}|\psi(\eta)\rangle$ is an excited state and thus orthogonal to the ground state. As one leaves the topological phase, charge fluctuations are possible, and the expectation value can be non-zero. The Wilson line suffers from a fatal flaw: There is no guarantee that $|\psi(\eta)\rangle$ has an exact 1-form Wilson loop symmetry [97, 98, 99, 100]. In the case of an *emergent* 1-form Wilson loop symmetry [101, 102], it is possible to adapt the initial idea into the Fredenhagen-Marcu (FM) order parameter [103, 104, 105, 106]: The bulk of the Wilson line (i.e., all but the end-points) is suppressed exponentially $\propto e^{-\alpha L}$ for a line of length L and some $\alpha > 0$. This suppression can be mitigated by embedding the system on a cylinder and defining the FM string as

$$\mathcal{O}_{\mathrm{FM}}(\eta) = \frac{\langle\psi(\eta)|\mathcal{W}_{L/2}|\psi(\eta)\rangle}{\sqrt{\langle\psi(\eta)|\mathcal{W}_{L}|\psi(\eta)\rangle}}, \tag{93}$$

where $\mathcal{W}_L$ is a Wilson loop that wraps the perimeter of the cylinder, while $\mathcal{W}_{L/2}$ covers only half of the perimeter (see Fig. 23). The exponential suppression is divided out exactly, while only $\mathcal{W}_{L/2}$ produces anyonic charges, which gives for the FM string the exact behavior of the Wilson line but without its pathology.

The FM string can be obtained efficiently from the dominant vectors.

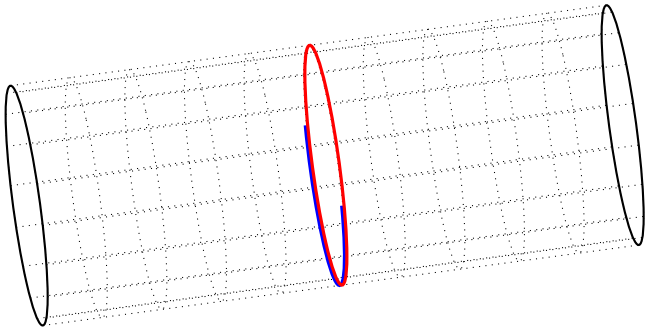

Figure 23: System nested on cylinder, with $\mathcal{W}_L$ (red) and $\mathcal{W}_{L/2}$ (blue) wrapping the perimeter of the cylinder.

Proposition 4. *Let $\mathcal{W}$ be a string-like operator that spans along the perimeter of a cylindrical system. In the limit of a large translation invariant system, the expectation value of $\mathcal{W}$ is given by*

$$\langle\psi|\mathcal{W}|\psi\rangle \propto \sum_{\alpha,\alpha',\beta,\beta'} L_{\alpha\beta}\Theta^{\alpha\alpha'}_{\beta\beta'}(\mathcal{W})R_{\alpha'\beta'} \tag{94}$$

where the $\Theta^{\alpha\alpha'}_{\beta\beta'}(\mathcal{W})$ is the modified transfer matrix hosting $\mathcal{W}$ on the contraction of physical indices. L and R are the dominant vectors of the usual transfer matrix.

Proof. The periodic boundary condition forces the operator string to lie within one transfer matrix, the expectation value can then be written as

$\langle\psi|\mathcal{W}|\psi\rangle =$ 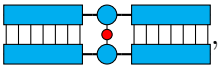 , (95)

where the red sphere represents $\mathcal{W}$. In the large system limit, the bulk left and right of the operator are proportional to the left and right dominant vector respectively. Defining

$\Theta^{\alpha\alpha'}_{\beta\beta'}(\mathcal{W}) =$ 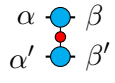 (96)

proves the statement. □

The proportionality only depends on the dominant vectors and not the

operator. Thus, it can be canceled by defining

$$\mathcal{O}_{\mathrm{FM}} = \frac{\sum_{\alpha,\alpha',\beta,\beta'} L_{\alpha\beta}\Theta^{\alpha\alpha'}_{\beta\beta'}(\mathcal{W}_{L/2})R_{\alpha'\beta'}}{\sqrt{\sum_{\alpha,\alpha',\beta,\beta'} L_{\alpha\beta}\Theta^{\alpha}_{\beta}(\mathcal{W}_{L})R_{\alpha\beta}}\sqrt{\sum_{\alpha,\alpha',\beta,\beta'} L_{\alpha\beta}R_{\alpha'\beta'}}}. \tag{97}$$

All of those contractions can be obtained efficiently through the familiar looking contraction in Fig. 24.

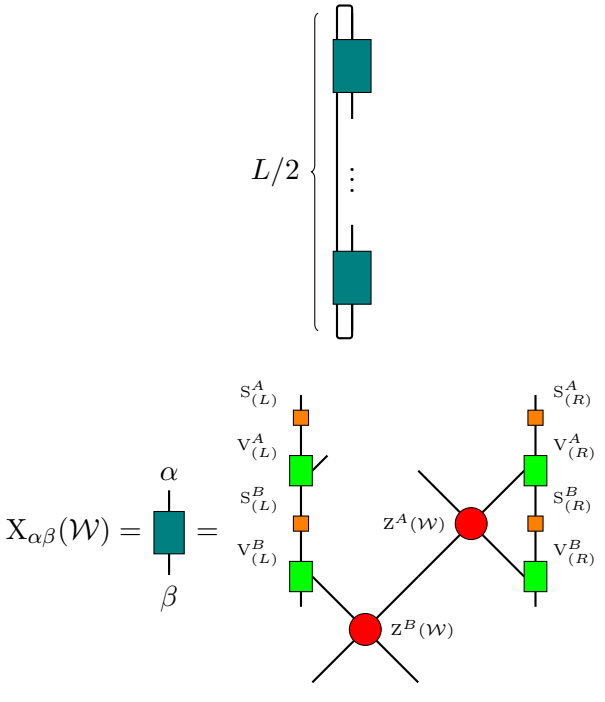

(98)

Figure 24: The contraction that allows the evaluation of the expectation value of a string operator $\mathcal{W}$ on the perimeter of the system embedded on a cylinder. The tensors $\mathrm{Z}^{A,B}(\mathcal{W})$ are modified Z-tensors hosting the local operators that make up the string $\mathcal{W}$, on the contraction of the physical indices. Possible virtual indices of the local operators are tucked in with the virtual indices of the state accordingly. Contracting first horizontally leaves the vertical contraction at complexity $O(L\chi^6 d^6)$, with d the dimension of the links of the modified Z-tensors. Notice that this contraction is not a repeated multiplication of the same matrix, as $\mathcal{W}$ needn't be translation invariant; in fact, $\mathcal{W}_{L/2}$ isn't.

Remark 8. Typically, the string operators have some translation invariance in the bulk, then one recovers the repeated multiplication of possibly multiple matrices. In this case, similar comments to Remarks 4, 6, and 7 can be made.

3.5 Universality at Criticality

It is a remarkable insight of the *renormalization group method* that the abundant set of all phase transitions (spanned by all the possible ways local details of a system may manifest) can be categorized through a few universality classes. In the vicinity of the phase transition, the correlation length ξ diverges; it is then reasonable to assume that the properties of the system at criticality can only depend on that scale set by ξ and not on details like the interaction, lattice spacing, or lattice geometry [59].

3.5.1 Universal Critical Exponent

The universal critical exponent ν determines how the correlation length diverges as criticality is approached

$$\xi \propto |\eta_c - \eta|^{-\nu}. \tag{99}$$

Fortunately, ξ can be accessed easily through our approach.

Proposition 5. *The correlation length ξ of a translation invariant TNS is determined by the left or right dominant vectors. Specifically,*

$$\xi = -\left[\ln\left|\frac{e_1}{e_0}\right|\right]^{-1}, \tag{100}$$

e_0 and e_1 are the largest and second largest eigenvalues of the transfer matrix $\mathcal{T}$ spanned by the dominant vector.

Proof. The spins of the TNS are nested on the links of the lattice. The "physical" degrees of freedom of the dominant vectors are the links. Moreover, the left and right dominant vectors reflect the left and right bulk of the system, respectively. Hence, observables acting locally on the spins of the 2D TNS are linked (through sandwiching in the Z-tensor) to observables acting locally on the dominant vectors (analogous to equations (95) and (96)). The correlation

function $C(r)$ of two "physical" degrees of freedom of the dominant vector (distant by r sites) is also the correlation function of two spins of the 2D TNS (distant by r sites parallel to the transfer matrix). It is a well-known fact that the correlation function of an infinite MPS is given by

$$C(r) = \left|\frac{e_1}{e_0}\right|^r, \tag{101}$$

e_0 and e_1 are the largest and second largest eigenvalues of $\mathcal{T}$ [88]:

$\mathcal{T}_{\alpha\beta} =$ 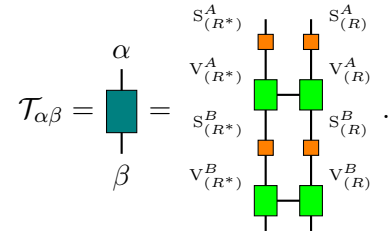

. (102)

The statement follows from the definition of the correlation function

$$C(r) = e^{-\frac{r}{\xi}} \tag{103}$$

upon taking the logarithm. □

It is standard procedure to determine the critical exponent from linear regression on a plot of $\ln(\xi)$ versus $\ln|\eta_c - \eta|$.

3.5.2 Central Charge

A seminal work by Pollmann et al. [107] showed that the finite-entanglement scaling of a 1D system is ruled by the central charge C, which counts the universal degrees of freedom of the critical point. Namely, the entanglement entropy $S(\chi)$ of an MPS (at the critical point) with a finite virtual bond dimension χ is given by:

$$S(\chi) = \frac{C}{6}\ln(\xi(\chi)). \tag{104}$$

The central charge can then be determined from the dominant vectors through linear regression on a plot of S versus $\ln(\xi)$, with data generated from varying choices of χ. To determine S, it may be necessary to execute N_u update steps (iTEBD-steps where $\mathrm{Z} = \mathbb{1}$) to ensure that the dominant vector satisfies the SVD-condition, then from the singular values

$$S = -\sum_{i=1}^{\chi} \left(\mathrm{S}_i^{A,B}\right)^2 \ln\left[\left(\mathrm{S}_i^{A,B}\right)^2\right] \tag{105}$$

as usual.

Now that we understand our method well and are armed with a handful of quantities that allow us to characterize topological phases and phase transitions, we can put the approach to the test.

4 Models and Results

To assess how accurate and efficient our method turns out to be, we trial it for a set of phase transitions on different physically relevant gauge models and varying lattice geometries. Moreover, it is important to attune our intuition to what parameters χ, N, L, and N_u numerics will deliver faithful results, while not spinning out the run-times. We will not bother with coming up with Hamiltonians $H(\eta)$ to then find the ground state $|\psi(\eta)\rangle$, either analytically or numerically, to then only test our code. That is beside the point of this thesis. We will start with a known Levin-Wen fixed-point wave function and deform it locally (e.g., through a string tension operator), such that for any $|\psi(\eta)\rangle$ the corresponding TN representation is known exactly. The results in the following were all generated from *Python 3* code constructed from scratch and running on a personal laptop operating on 32 GB of RAM and an *AMD Ryzen 9 7940HX* CPU.

4.1 Toric Code

The legendary Toric Code (TC) model proposed by Kitaev [31, 32] is the simplest and most well-understood lattice gauge model with topological order. It is constructed on the $\mathbb{Z}_2$ gauge, that is, it "knows" only one string type. Traditionally, the model is nested on a square lattice wrapped into the shape of a torus, and is reigned through the Hamiltonian

$$H_{\mathrm{TC}} = -\sum_S \bigotimes_{i\in S} \sigma_i^x - \sum_P \bigotimes_{i\in P} \sigma_i^z, \tag{106}$$

with the usual Pauli operators $\sigma_i^{x,z}$ acting on sites i of the stars S and plaquettes P, respectively. The ground state is known exactly

$$|\mathrm{TC}\rangle = \frac{1}{\sqrt{2^{\mathcal{N}}}} \prod_P \left(\mathbb{1} + \bigotimes_{i\in P} \sigma_i^z \right)_P |0\rangle, \tag{107}$$

with $\mathcal{N}$ the number of plaquettes in the system. From the string-net perspective, the ground state is given by an equal superposition of all possible closed string configurations $\mathcal{C}$

$$|\mathrm{TC}\rangle = \frac{1}{\sqrt{N_{\mathcal{C}}}} \sum_{\mathcal{C}} |\mathcal{C}\rangle, \tag{108}$$

with $N_{\mathcal{C}}$ the total number of configurations. The system hosts four different anyon types, all of which are their own anti-particle: $\mathbf{1}$ with trivial charge, e with "electric" charge, m with "magnetic" charge, and the fusion product $\epsilon = e \otimes m$. All of the anyons are self-bosonic, but e, m, and ϵ are mutually fermionic. All of the anyons are Abelian ($d_{\mathbf{1}} = d_e = d_m = d_\epsilon = 1$), leading to $S^{\mathrm{topo}} = \ln(2)$ in the Toric Code Phase. The Toric Code inspired the surface and color code paradigms for stable quantum memory and has served the physics community as a testing ground for more than two decades.

4.1.1 TC on the Square Lattice

Castelnovo et al. [43] solved a phase transition between the Toric Code phase on the square lattice and a trivial phase analytically. The considered Hamiltonian

$$H(\eta) = H_{\mathrm{TC}} + \sum_S e^{-\eta \sum_{i\in S} \sigma_i^z} \tag{109}$$

adds a string tension term to the usual TC Hamiltonian, i.e., -1 spin states come at an energy cost, which will dilute the string-net at large enough η. For any η the ground state is known to be

$$|\psi(\eta)\rangle = \frac{1}{\sqrt{\Omega}} e^{\frac{\eta}{2}\sum_i \sigma_i^z} |\mathrm{TC}\rangle \tag{110}$$

with normalization Ω. The ground state clearly illustrates how the amplitude of string configurations is suppressed exponentially with η, and the larger the string-net spans. The analytical solution stems from the fact that the magnetization is directly related to the energy of the classical Ising model on the square lattice:

$$m(\eta) \propto \sum_i \langle\psi(\eta)|\sigma_i^z|\psi(\eta)\rangle = E_{\mathrm{Ising}}(\eta). \tag{111}$$

The derivative is discontinuous, which maps the critical point η_c of the topological phase transition onto the critical point $\beta_c = \frac{1}{2}\ln\left(1+\sqrt{2}\right) \approx 0.440687$ of the classical Ising model. As this critical point is well understood, this transition offers the perfect testing bed as to whether our approach determines correctly the expected critical point and its universal characteristics: $\nu = 1$ and $C = \frac{1}{2}$.

The parametrized Z-tensor can constructed (up to a multiplicative constant) with minimal bond dimension $d = 2$ (see Appendix B.1):

$$\mathrm{Z}_{\alpha\beta\gamma\delta} = \begin{cases} e^{4\eta} & \text{if } \alpha+\beta+\gamma+\delta = 0 \\ e^{2\eta} & \text{if } \alpha+\beta+\gamma+\delta = 2 \\ 1 & \text{if } \alpha+\beta+\gamma+\delta = 4 \\ 0 & \text{otherwise} \end{cases}. \tag{112}$$

As the simplification in Appendix A.1 was used, the dominant vectors must be diagonal matrices. It follows from Hermiticity that the dominant vectors are real and symmetric; moreover, the Z-tensor is real, so that the transfer matrix must also be. Hence, by the definition of right dominant vector

$$\Theta R = \lambda_0 R \tag{113}$$
$$\Rightarrow \quad (\Theta R)^\dagger = (\lambda_0 R)^\dagger \tag{114}$$
$$\Rightarrow \quad \Theta^T R = \lambda_0 R \tag{115}$$

so that the right dominant vector must also be the left dominant vector, on top $R = L^T$. Corollaries 1 and 2 both hold for this phase transition.

Fig. 25 illustrates the phase transition through the TEE, which drops sharply at the expected critical point. Notice that the transition is still continuous in the zoomed-in pictures, even though it is expected to be discontinuous, given that it depends on the multiplicity of the largest eigenvalues. This follows, as the considered system is large but still finite, a necessary numerical choice: Across the phase transition, the eigenvalues shift slowly and continuously, so that it is hard to discern whether the minimal difference between them follows from numerical inaccuracies / machine error or the phase transition. The transition in the TEE plot sharpens as the system size is increased, suggesting a perfectly sharp transition in the thermodynamic limit. However, arbitrarily increasing χ does not provide a considerable improvement. The reduced fidelity in Fig. 26 finds the critical point to be identical to the critical point of the classical Ising model on the square lattice up to a relative error of 0.02%. The central charge and the critical exponent are determined with satisfying accuracy in Fig. 27 and Fig. 28 respectively.

Topological Entanglement Entropy across the Phase Transition for the Toric Code on the Square Lattice

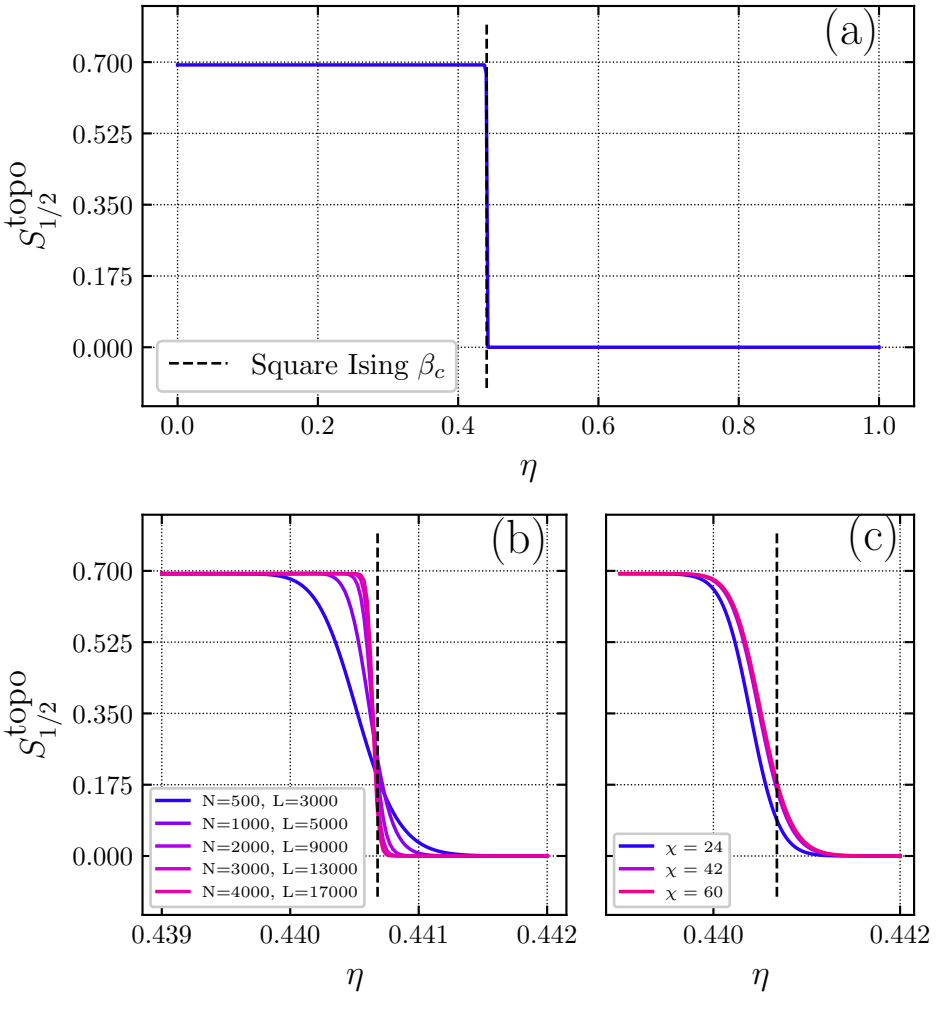

Figure 25: (a) The TEE remains constant and equal to ln(2) up to the critical point, coinciding with the critical point of the classical 2D-Ising model on the square lattice $\beta_c = \frac{1}{2}\ln\left(1+\sqrt{2}\right) \approx 0.440687$. At the critical point, it drops sharply to zero. (The plot generation took 2.6 min with $N = 500$, $L = 2400$, $\chi = 24$, and η in steps of 0.0025.) (b) At criticality, the sharpness of the transition is dictated by the system size; the scaling indicates a perfectly sharp transition in the thermodynamic limit. (The plot generation took 26 min, with $\chi = 44$, and η in steps of 0.000025.) (c) Even large increments in χ don't provide a noteworthy improvement. (The plot generation took 10 min with $N = 500$, $L = 3600$, and η in steps of 0.000025.)

Reduced Fidelity across the Phase Transition for the Toric Code on the Square Lattice

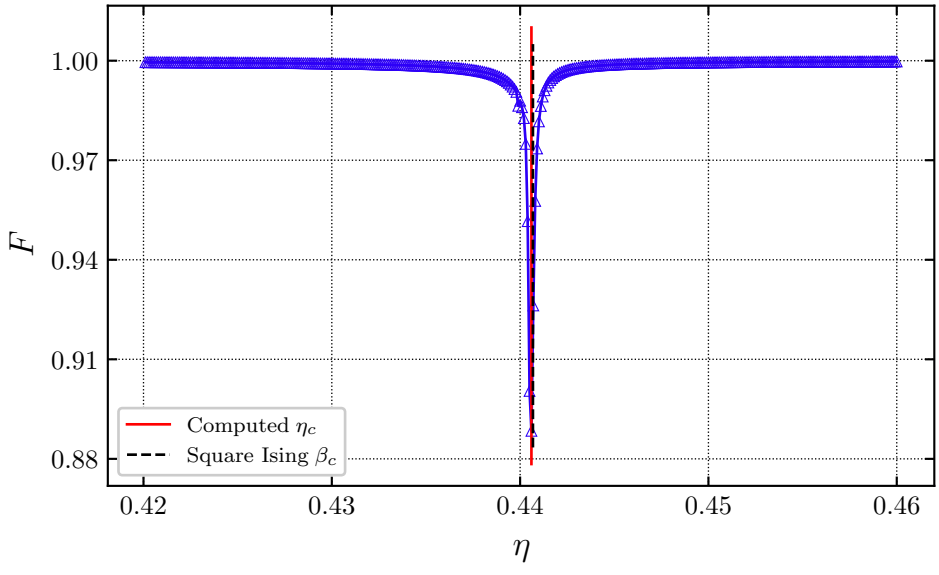

Figure 26: The partial fidelity dips around the critical point of the 2D-Ising model on the square lattice. The critical point found through the fidelity is $\eta_c = 0.4406 \pm 0.0001$. (The plot generation took 10 min, with $N = 1200$, $L = 8192$, $\chi = 30$, and η in steps of 0.0001.)

MPS Entanglement Entropy v. the Logarithm of the Correlation Length at the Critical Point for the Toric Code on the Square Lattice

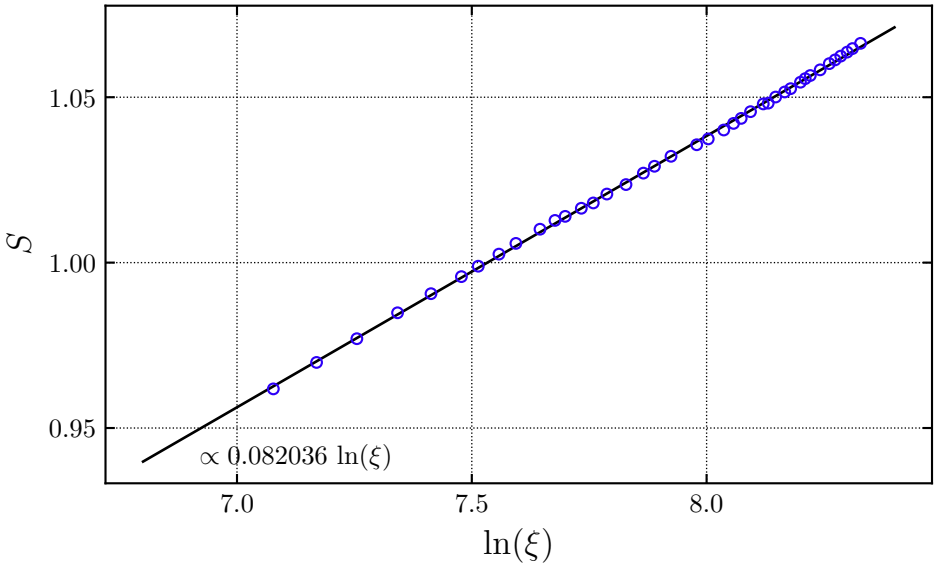

Figure 27: All points are clearly aligned. Linear regression numerically determines the central charge as $C = 0.492216$. (The plot generation took 14.5 min, with $N = 5000$, $N_u = 3000$, $\chi \in \{30, 31, \ldots, 69\}$, and $\eta = \eta_c = 0.440687$.)

Logarithm of the Correlation Length v. the Logarithm of the Distance from Critical Point for the Toric Code on the Square Lattice

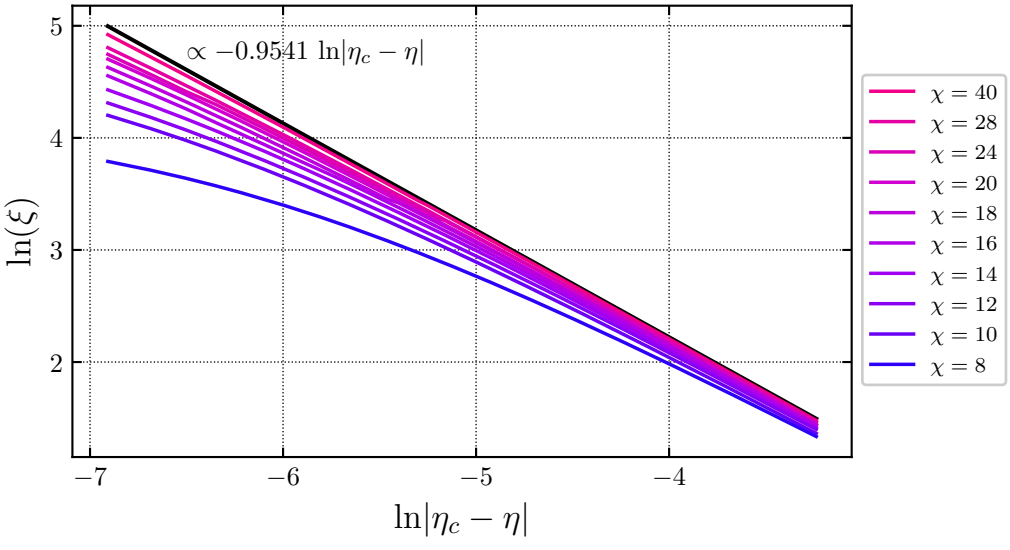

Figure 28: The graphs converge to a line as χ increases. Linear regression on the linear part of the graph for large χ determines the critical exponent $\nu = 0.9541$.(The plot generation took 18 min, with $N = 1000$ and η in steps of 0.00025.)

4.1.2 TC on the Honeycomb Lattice

The argument from Castelnovo et al. can be translated identically to other lattice geometries, up to one nuance: Since the spins are nested on the links of the lattice, the mapping is onto the classical Ising model on the dual lattice. The expected critical point on the honeycomb lattice is then the critical point of the classical Ising model on the triangular lattice $\beta_c = \frac{1}{4}\ln(3) \approx 0.274653$. Meanwhile, the critical properties remain unaltered.

Analogously to the the square lattice the Z-tensor has bond dimension $d = 2$ the non-zero entries are (see Appendix B.2):

$$\mathrm{Z}_{0000} = e^{4\eta}, \tag{116}$$

$$\mathrm{Z}_{1100} = \mathrm{Z}_{0011} = e^{2\eta}, \tag{117}$$

$$\mathrm{Z}_{1001} = \mathrm{Z}_{0110} = \mathrm{Z}_{1010} = \mathrm{Z}_{0101} = \mathrm{Z}_{1111} = 1. \tag{118}$$

Corollaries 1 and 2 both hold for the identical reason as beforehand on the square lattice.

Fig. 29 illustrates the phase transition through the TEE, which drops sharply at the expected critical point. The reduced fidelity in Fig. 30 finds the critical point to be identical to the critical point of the classical Ising model on the triangular lattice up to a relative error of 0.02%. The central charge and the critical exponent are determined with satisfying accuracy in Fig. 31 and Fig. 32 respectively.

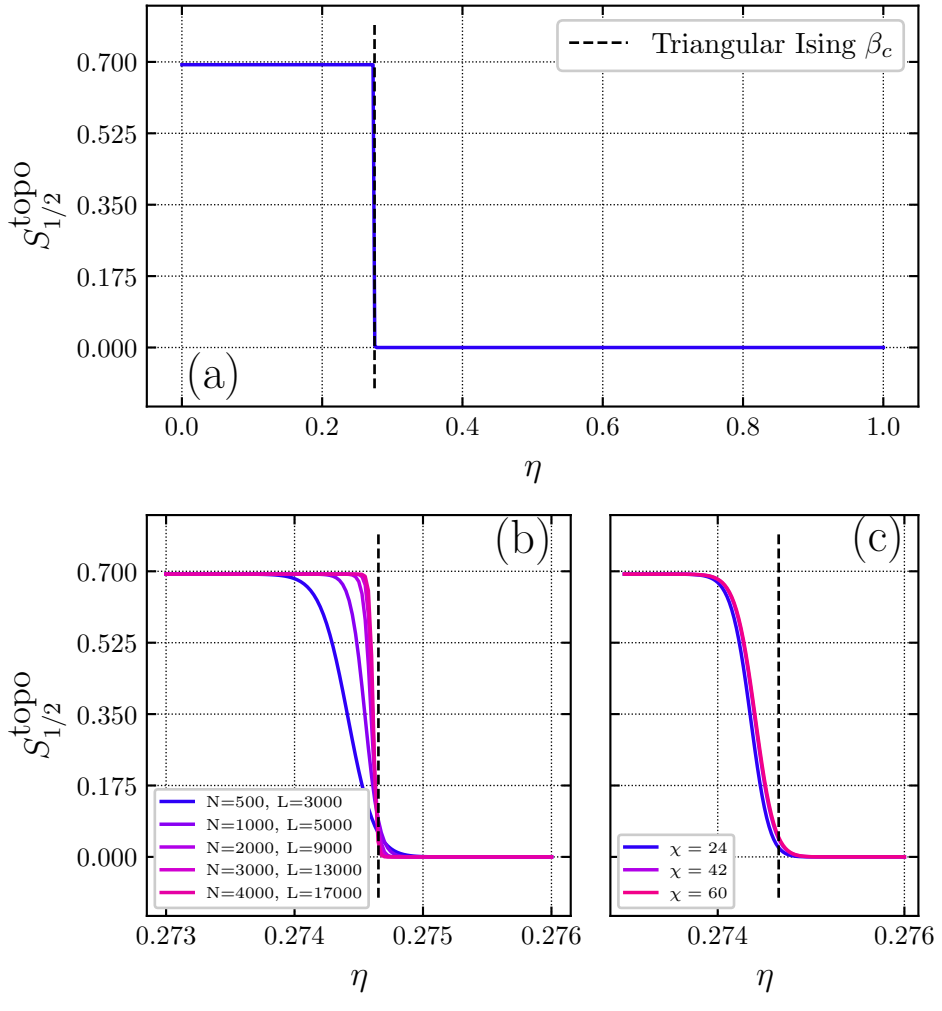

Figure 29: (a) The TEE remains constant and equal to ln(2) up to the critical point, coinciding with the critical point of the classical 2D-Ising model on the triangular lattice $\beta_c = \frac{1}{4}\ln(3) \approx 0.274653$. At the critical point, it drops sharply to zero. (The plot generation took 1.4 min with $N = 500$, $L = 2400$, $\chi = 24$, and η in steps of 0.0025.) (b) At criticality, the sharpness of the transition is dictated by the system size; the scaling indicates a perfectly sharp transition in the thermodynamic limit. (The plot generation took 26 min, with $\chi = 44$, and η in steps of 0.000025.) (c) Even large increments in χ don't provide a noteworthy improvement. (The plot generation took 10 min with $N = 500$, $L = 3600$, and η in steps of 0.000025.)

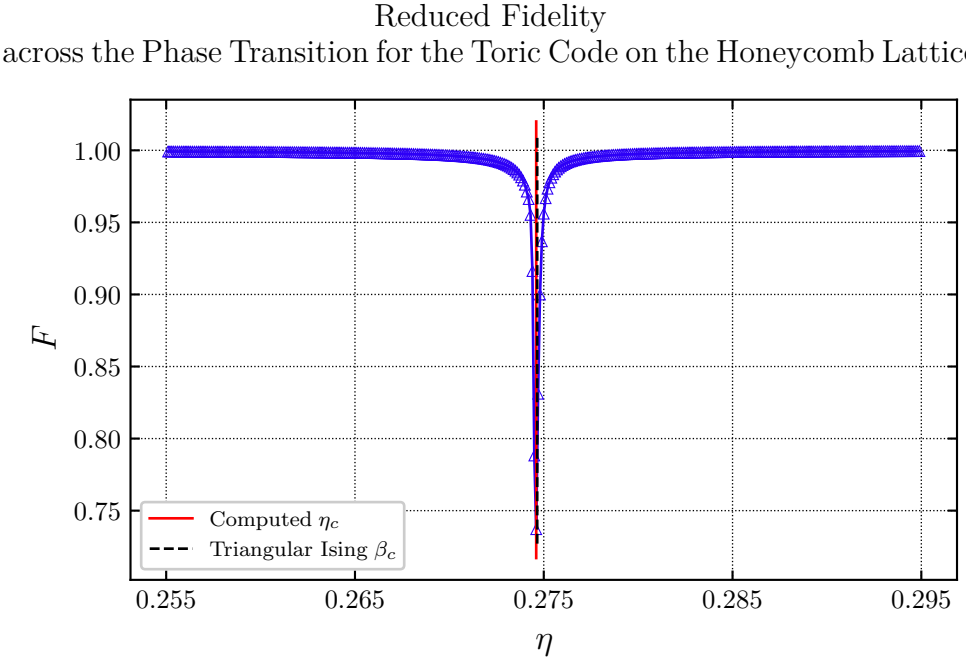

Figure 30: The partial fidelity dips around the critical point of the 2D-Ising model on the triangular lattice. The critical point found through the fidelity is $\eta_c = 0.2746 \pm 0.0001$. (The plot generation took 12 min, with $N = 1200$, $L = 8192$, $\chi = 30$, and η in steps of 0.0001.)

MPS Entanglement Entropy v. the Logarithm of the Correlation Length at the Critical Point for the Toric Code on the Honeycomb Lattice

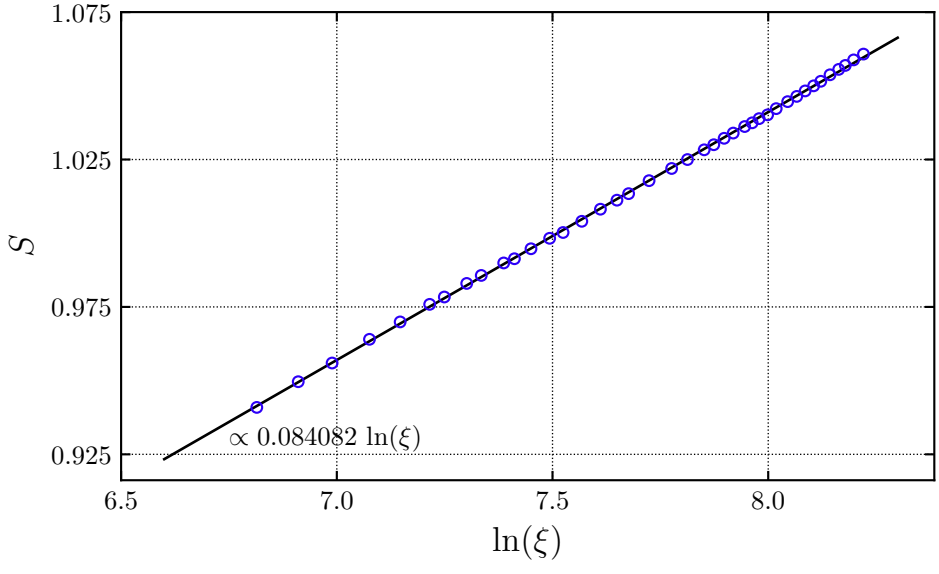

Figure 31: All points are clearly aligned. Linear regression numerically determines the central charge as $C = 0.504492$. (The plot generation took 19.7 min, with $N = 9000$, $N_u = 2000$, $\chi \in \{30, 31, \ldots, 69\}$, and $\eta = \eta_c = 0.274653$.)

Logarithm of the Correlation Length v. the Logarithm of the Distance from Critical Point for the Toric Code on the Honeycomb Lattice

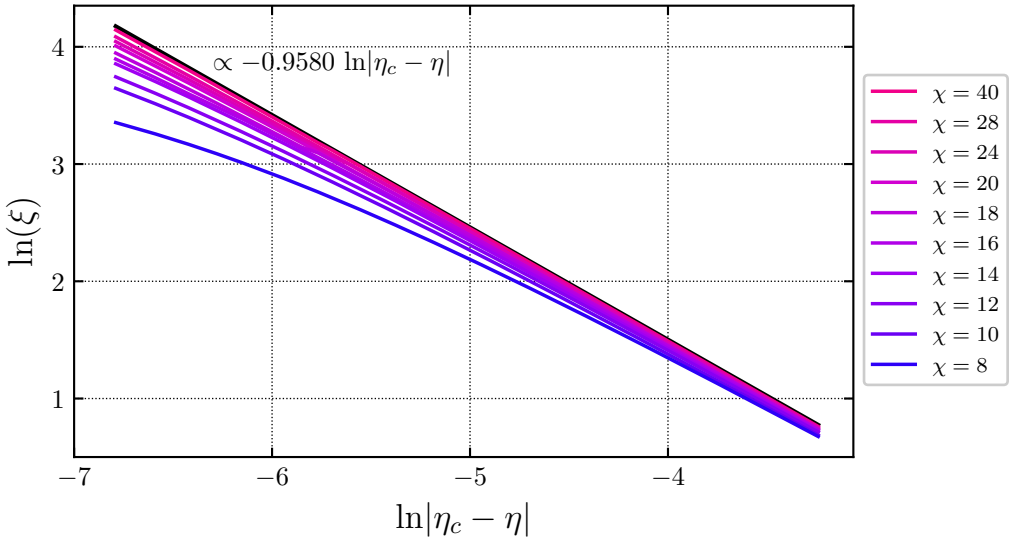

Figure 32: The graphs converge to a line as χ increases. Linear regression on the linear part of the graph for large χ determines the critical exponent $\nu = 0.9580$. (The plot generation took 17.5 min, with $N = 1000$ and η in steps of 0.00025.)

4.1.3 TC on the Triangular Lattice

The expected critical point for the Toric Code on the triangular lattice is the critical point of the classical Ising model on the honeycomb lattice $\beta_c = \frac{1}{2}\ln\left(2+\sqrt{3}\right) \approx 0.658479$.

The Z-tensor can again be brought back to bond dimension $d = 2$ with non-zero entries (up to a multiplicative constant, see Appendix B.3):

$$\mathrm{Z}_{0000} = e^{3\eta}, \tag{119}$$

$$\mathrm{Z}_{1001} = \mathrm{Z}_{1100} = \mathrm{Z}_{1010} = e^{2\eta}, \tag{120}$$

$$\mathrm{Z}_{0110} = \mathrm{Z}_{0011} = \mathrm{Z}_{0101} = e^{\eta}, \tag{121}$$

$$\mathrm{Z}_{1111} = 1. \tag{122}$$

One subtlety must be minded: Remember that the mapping of the triangular lattice onto the square lattice in Fig. 15b makes use of an SVD giving rise to a new bond (in green) - here the first index of the Z-tensor. To properly apply the transfer matrix, these bonds must connect along the iTEBD, that is, this bond must hop back and forth between the first and last index on each update step. Corollaries 1 and 2 both hold

Fig. 33 illustrates the phase transition through the TEE, which drops sharply at the expected critical point. The reduced fidelity in Fig. 34 finds the critical point to be identical to the critical point of the classical Ising model on the honeycomb lattice up to a relative error of 0.02%. The central charge and the critical exponent are determined with satisfying accuracy in Fig. 35 and Fig. 36 respectively.

Topological Entanglement Entropy
across the Phase Transition for the Toric Code on the Triangular Lattice

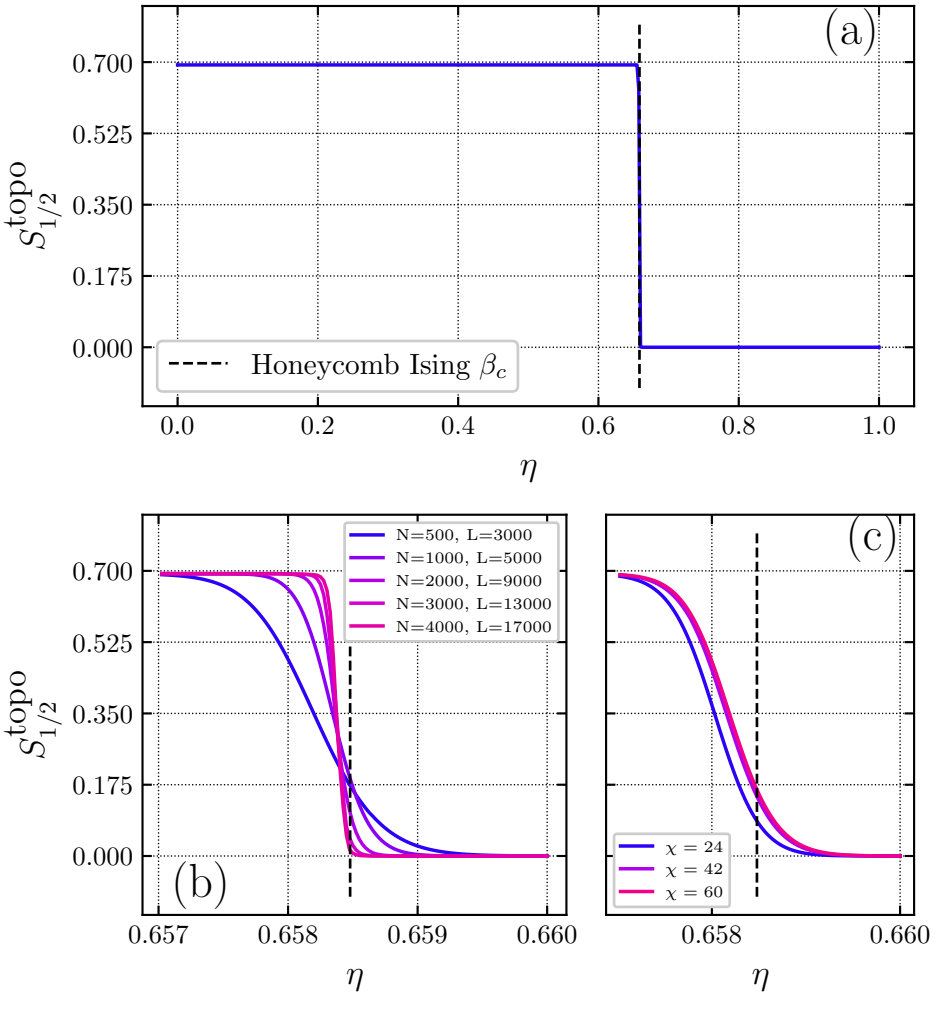

Figure 33: (a) The TEE remains constant and equal to ln(2) up to the critical point, coinciding with the critical point of the classical 2D-Ising model on the honeycomb lattice $\beta_c = \frac{1}{2}\ln\left(2+\sqrt{3}\right) \approx 0.658479$. At the critical point, it drops sharply to zero. (The plot generation took 2.3 min with $N = 500$, $L = 2400$, $\chi = 24$, and η in steps of 0.0025.) (b) At criticality, the sharpness of the transition is dictated by the system size; the scaling indicates a perfectly sharp transition in the thermodynamic limit. (The plot generation took 26 min, with $\chi = 44$, and η in steps of 0.000025.) (c) Even large increments in χ don't provide a noteworthy improvement. (The plot generation took 11 min with $N = 500$, $L = 3600$, and η in steps of 0.000025.)

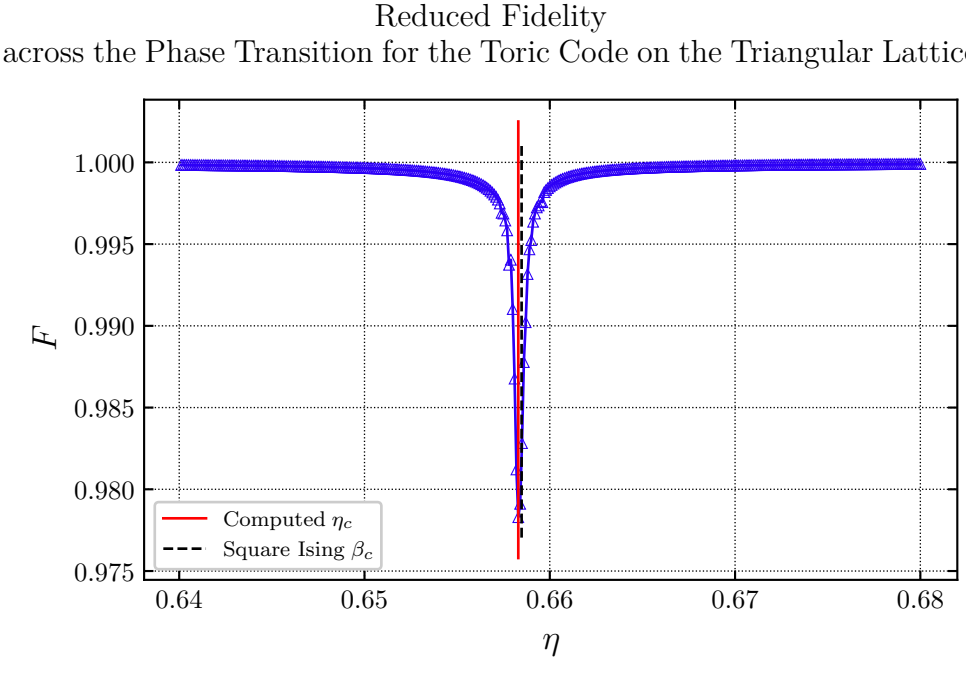

Figure 34: The partial fidelity dips around the critical point of the 2D-Ising model on the honeycomb lattice. The critical point found through the fidelity is $\eta_c = 0.6583 \pm 0.0001$. (The plot generation took 11 min, with $N = 1200$, $L = 8192$, $\chi = 30$, and η in steps of 0.0001.)

MPS Entanglement Entropy v. the Logarithm of the Correlation Length at the Critical Point for the Toric Code on the Triangular Lattice

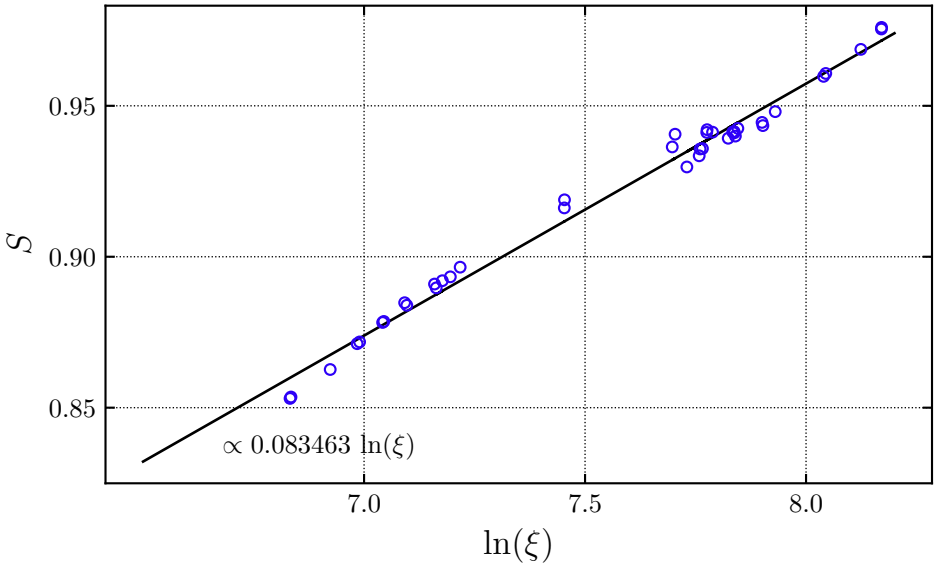

Figure 35: All points are aligned. Linear regression numerically determines the central charge as $C = 0.500777$. (The plot generation took 19.9 min, with $N = 7500$, $N_u = 2500$, $\chi \in \{30, 31, \ldots, 69\}$, and $\eta = \eta_c = 0.658479$.)

Logarithm of the Correlation Length v. the Logarithm of the Distance from Critical Point for the Toric Code on the Triangular Lattice

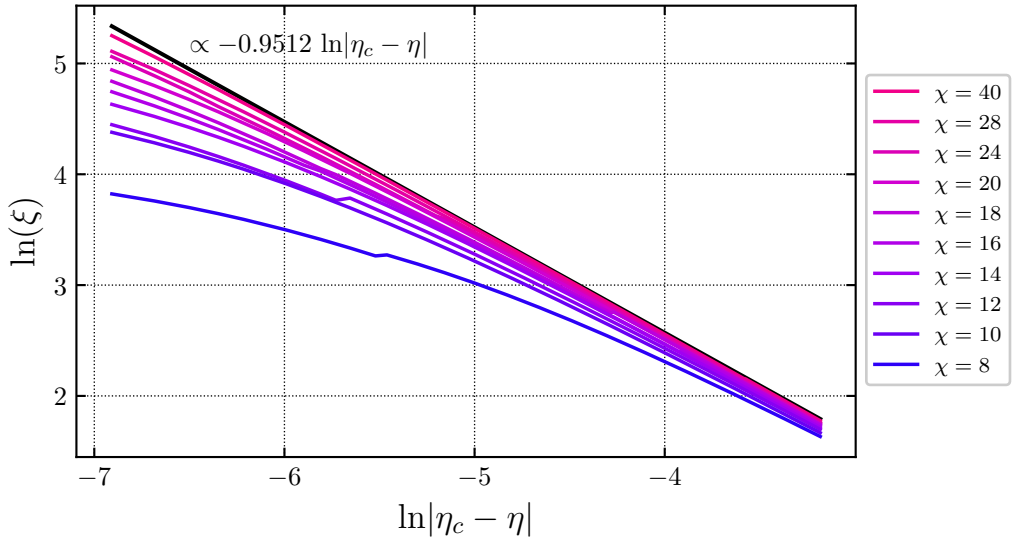

Figure 36: The graphs converge to a line as χ increases. Linear regression on the linear part of the graph for large χ determines the critical exponent $\nu = 0.9512$. (The plot generation took 22.1 min, with $N = 1000$ and η in steps of 0.00025.)

4.2 Fredenhagen-Marcu Order Parameter

Recently Xu et al. [57] studied the critical behavior of the FM observable for a phase transition on the Toric Code. The deformed state is determined through two parameters (with normalization Ω)

$$|\psi(g_x, g_y)\rangle = \frac{1}{\sqrt{\Omega}} \bigotimes_i (\mathbb{1}_i + g_x \sigma_i^x + g_z \sigma_i^z) \, |\mathrm{TC}\rangle. \tag{123}$$

The paper finds, that this family of states highlights the necessary emergent 1-form symmetry for sufficiently small parameters. The FM order parameter consists of locally applied Pauli-Z operators

$$\mathcal{W}_\mathcal{L} = \bigotimes_{i \in \mathcal{L}} \sigma_i^z, \tag{124}$$

for a line $\mathcal{L}$. The FM string creates an "electric" charge e on each end of the line, so that it is only fully sensitive to the g_z-deformation, which enables "electric" charge fluctuations (in the charge condensed region of the trivial phase), but cannot reveal "magnetic" flux fluctuations that are enabled by the g_x-deformation (in the flux condensed region of the trivial phase).

The deformation is no longer a simple string tension, which ruins the simplification discussed in Appendix A.1. Thus, the Z-tensor must be assembled naively from the g- and T-tensors as defined in **II.** of Ref. [52] acting with the deformation on the physical indices, the bond dimension of Z is $d = 4$.

The phase diagram in Fig. 37 mirrors the findings by Xu et al. The topological entanglement entropy in Fig. 38 confirms the phase diagram, whereas the TEE can also resolve the phase transition in the flux condensed regime $g_x > g_z$, which the FM observable is incapable of.

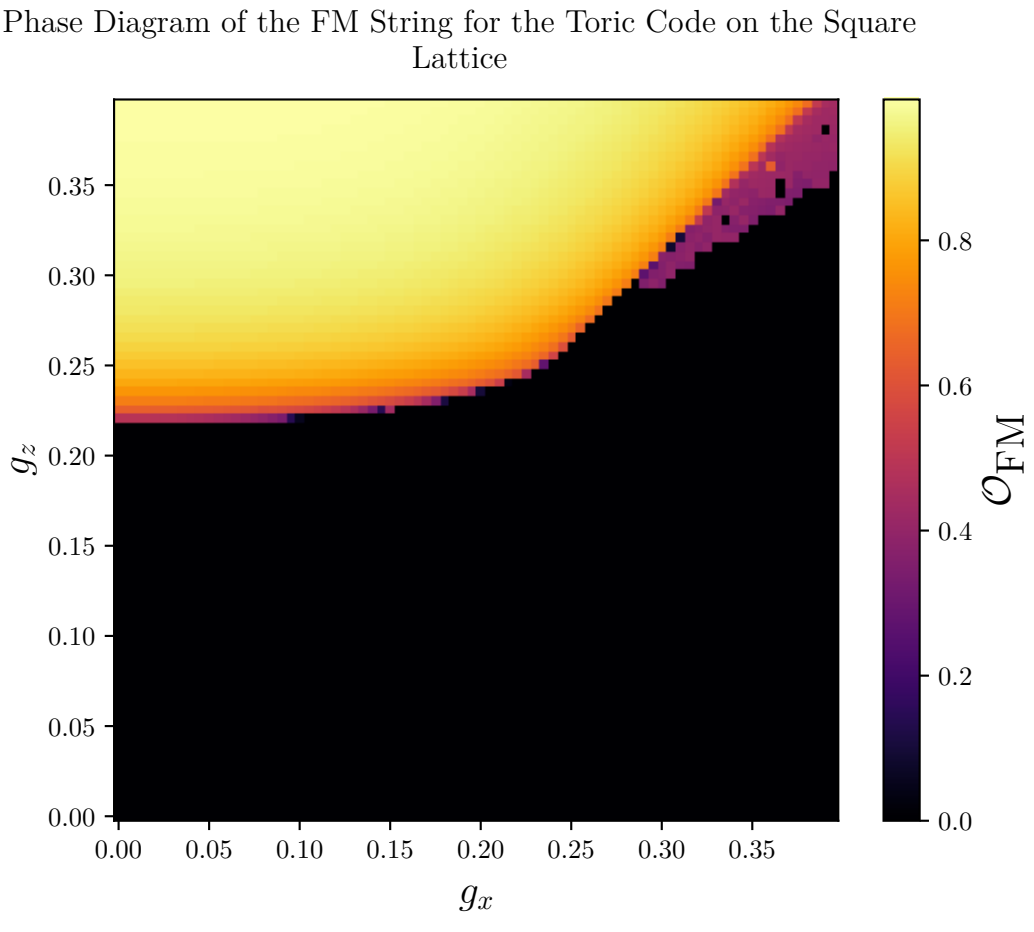

Figure 37: The FM order parameter is constant and equal to zero in the Toric Code phase and becomes finite as the charge condensed phase is entered. Except for some non-zero values spilling into the flux condensed region at the self-duality line $g_x = g_z$, the FM observable is null. The phase diagram reflects the expected shape found in Fig. 4a of Ref. [57]. (The plot generation took 129 min, with $N = 500$, $L = 128$, $\chi = 20$, and g_x, g_z in steps of 0.005.)

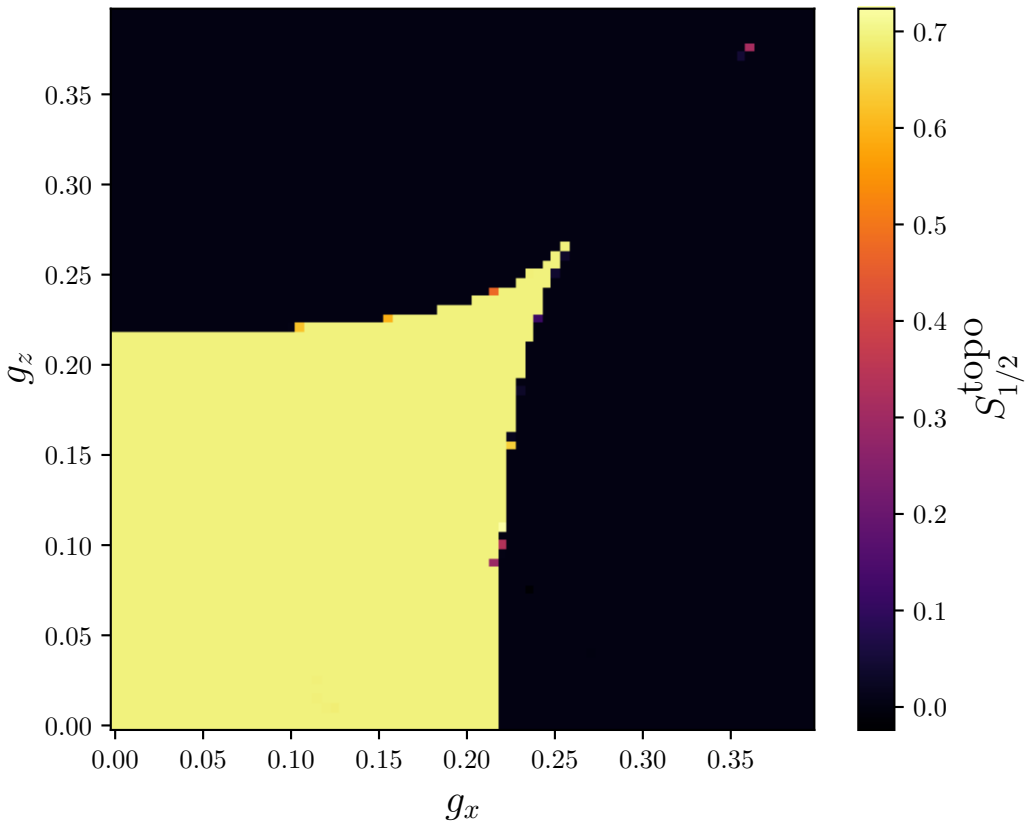

Figure 38: The TEE is constant and equal to ln(2) in the Toric Code phase. Outside of the topological phase, it drops sharply to zero. (The plot generation took 101 min, with $N = 500$, $L = 4000$, $\chi = 16$ resp. $\chi = 32$ close to the phase transition, and g_x, g_z in steps of 0.005.)

4.3 Double Semion Model

The Double Semion (DS) model proposed in 2004 [108] is another $\mathbb{Z}_2$ lattice gauge theory that fits the string-net picture [42]. The Double Semion phase is reminiscent of the TC phase, as the DS ground state is given by the superposition of all closed loop configurations, with a phase $+1$ for an even number and -1 for an odd number of loops

$$|\mathrm{DS}\rangle = \frac{1}{\sqrt{N_{\mathcal{C}}}} \sum_{\mathcal{C}} (-1)^{n_{\mathcal{C}}} |\mathcal{C}\rangle, \tag{125}$$

$N_{\mathcal{C}}$ gives the number of closed loops in configuration $\mathcal{C}$ [109]. The notion of closed loops is ill-defined on the square lattice, so that the Double Semion model is constructed on the honeycomb lattice with the Hamiltonian

$$H_{\mathrm{DS}} = -\sum_{S} \bigotimes_{j \in S} \sigma_j^x + \sum_{P} \left(\bigotimes_{j \in P} \sigma_j^z \right) \left(\bigotimes_{k \in \text{legs of } P} i^{\frac{1-\sigma_k^x}{2}} \right), \tag{126}$$

the legs of P are the six links that radiate out of the plaquette (see Fig. 3).

Due to the similarity between the TC and the DS, we can mirror the transition we considered beforehand for the Toric Code by applying the same deformation onto the DS ground state:

$$|\psi(\eta)\rangle = \frac{1}{\sqrt{\Omega}} e^{\frac{\eta}{2} \sum_i \sigma_i^z} |\mathrm{DS}\rangle. \tag{127}$$

Although it is not evident, we should expect the identical critical point and critical properties for this transition. However, unlike for the TC, the Z-tensor for the DS transition does not have an elegant representation with bond dimension $d = 2$. The ideal TN representation given in **III.** of Ref. [52] has a double-line structure which doesn't project the physical state directly into a single virtual index, so that the previous simplification is not viable. The Z-tensor must be constructed in the naive way, by adding the deformation locally onto the physical indices and then assembling the g- and T-tensors as usual. Whereas, Z can be simplified from a bond dimension $d = 16$ to $d = 8$ through the procedure in Appendix A.2. We find Corollary 1 to hold.

Fig. 39 illustrates the phase transition through the TEE, which drops sharply at the expected critical point. The reduced fidelity in Fig. 40 finds

the critical point to be identical to the critical point of the classical Ising model on the triangular lattice up to a relative error of 0.02%. The central charge and the critical exponent are determined with satisfying accuracy in Fig. 41 and Fig. 42 respectively. The critical point and the critical properties are identical to those found for the Toric Code, so that we can conclude that both systems are indeed subjects of the same phase transition.

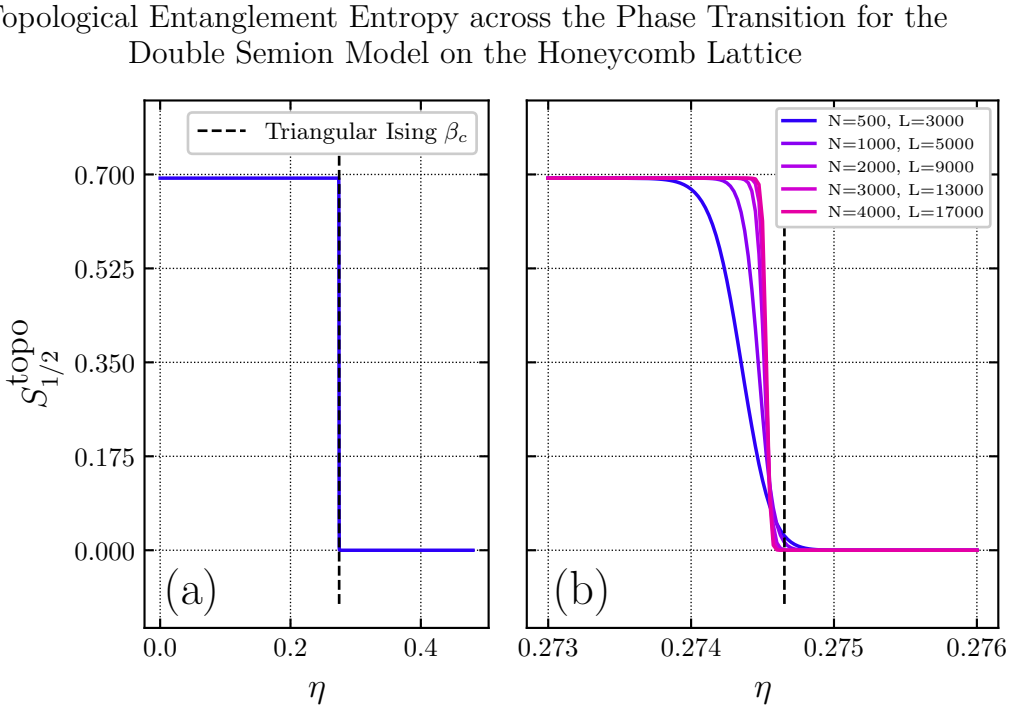

Figure 39: (a) The TEE remains constant and equal to ln(2) up to the critical point, which coincides with the critical point of the classical 2D-Ising model on the triangular lattice $\beta_c = \frac{1}{4}\ln(3) \approx 0.274653$. At the critical, point it drops sharply to zero. (The plot generation took 31 min with $N = 500$, $L = 2000$, $\chi = 56$, and η in steps of 0.0002 close to criticality.) (b) At criticality, the sharpness of the transition is dictated by the system size; the scaling indicates a perfectly sharp transition in the thermodynamic limit. (The plot generation took 6.3 h, with $\chi = 88$, and η in steps of 0.000025.)

Reduced Fidelity across the Phase Transition for the Double Semion Model on the Honeycomb Lattice

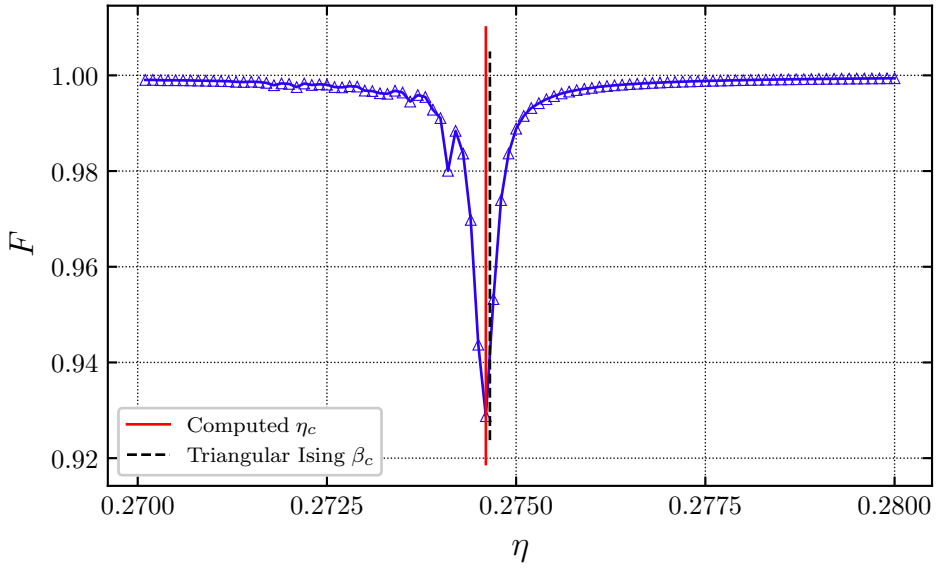

Figure 40: The partial fidelity dips around the critical point of the 2D-Ising model on the triangular lattice. The critical point found through the fidelity is $\eta_c = 0.2746 \pm 0.0001$. (The plot generation took 105 min, with $N = 1200$, $L = 4096$, $\chi = 70$, and η in steps of 0.0001.)

MPS Entanglement Entropy v. the Logarithm of the Correlation Length at the Critical Point for the Double Semion Model on the Honeycomb Lattice

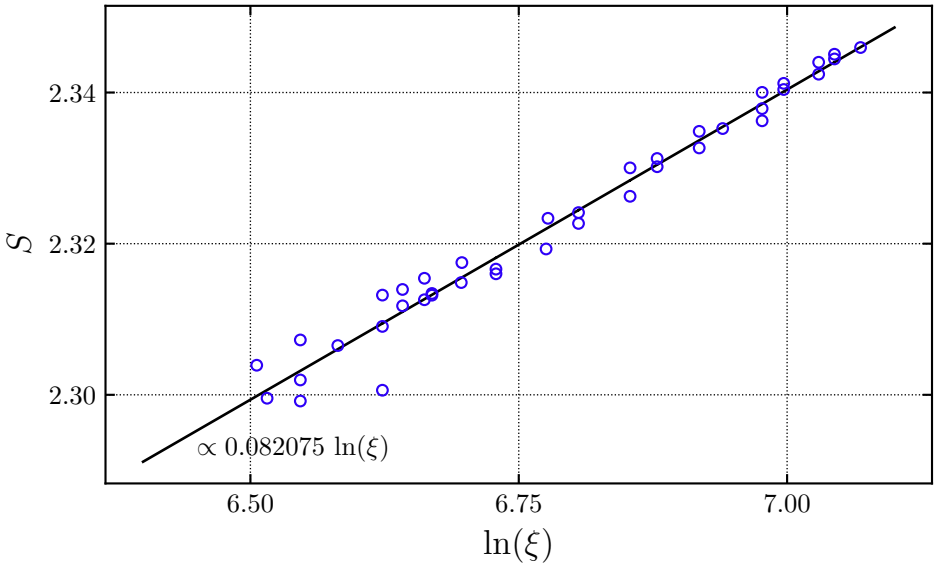

Figure 41: The points are scattered closely along a linear pattern. Linear regression numerically determines the central charge as $C = 0.492451$. (The plot generation took 9 h, with $N = 3500$, $N_u = 2000$, $\chi \in \{100, 101, \ldots, 139\}$, and $\eta = \eta_c = 0.274653$.)

Logarithm of the Correlation Length v. the Logarithm of the Distance from Critical Point for the Double Semion Model on the Honeycomb Lattice

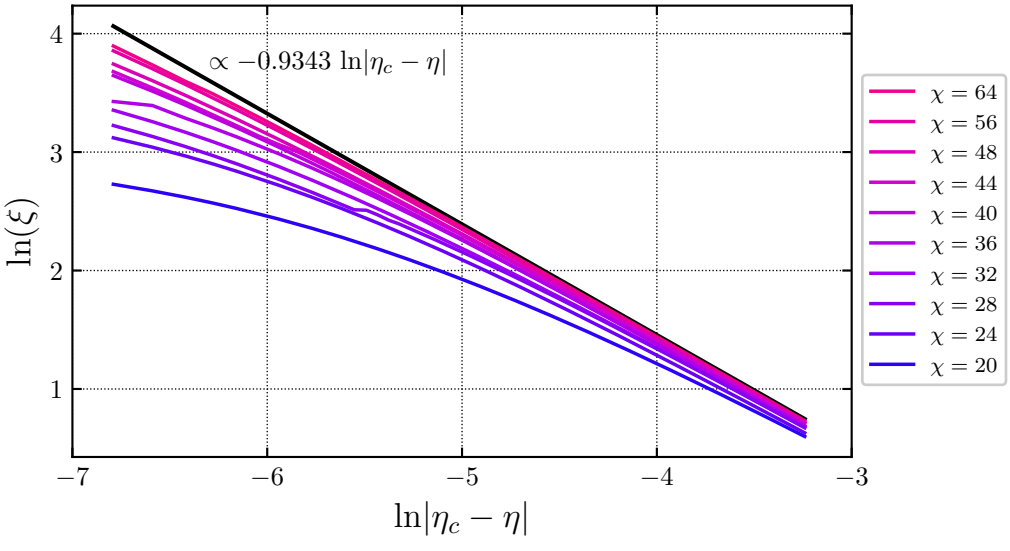

Figure 42: The graphs converge to a line as χ increases. Linear regression on the linear part of the graph for large χ determines the critical exponent $\nu = 0.9343$. (The plot generation took 7.5 h, with $N = 1000$ and η in steps of 0.00025.)

4.4 Double Fibonacci Model

The Double Fibonacci (DFib) model is the string-net realization of Fibonacci anyons τ, which are candidate for universal quantum computation through anyon braiding [62]. Fibonacci anyons are non-Abelian and have quantum dimension $d_\tau = \phi = \frac{1+\sqrt{5}}{2}$, so that the doubled phase yields topological entanglement entropy

$$S^{\text{topo}} = \ln(1+\phi^2) \approx 1.28593. \tag{128}$$

The Fibonacci anyons fuse non trivially

$$\tau \otimes \tau = \tau \oplus \mathbf{1}. \tag{129}$$

A transition from the DFib phase to a trivial phase was studied in [55, 56], the deformed state is nested on the honeycomb lattice

$$|\psi(\eta)\rangle = \frac{1}{\sqrt{\Omega}} \bigotimes_{i,j} e^{\frac{K}{4}(\sigma_i^z+\sigma_j^z)} |\text{DFib}\rangle \tag{130}$$

where i ranges over all the X-bonds and j over all the Y-bonds of the lattice (see Fig. 43), $|\text{DFib}\rangle$ is the Levin-Wen DFib fixed-point wave function, and Ω is the normalization. For the DFib model, $F^{ijk}_{tsu} \neq 0$ whenever

$$\delta_{ijk}\delta_{tsk}\delta_{isu}\delta_{jtu} = 1, \tag{131}$$

where the non-zero entries of δ_{ijk} reflect the fusion/branching rules (eqn. (8))

$$\delta_{\mathbf{111}} = \delta_{\mathbf{1}\tau\tau} = \delta_{\tau\mathbf{1}\tau} = \delta_{\tau\tau\mathbf{1}} = \delta_{\tau\tau\tau} = 1. \tag{132}$$

The non-trivial entries of the F-tensor are

$$F^{\tau\tau k}_{\tau\tau u} = \frac{1}{\phi} \begin{pmatrix} 1 & \sqrt{\phi} \\ \sqrt{\phi} & -1 \end{pmatrix}_{ku}, \tag{133}$$

while the remaining non-zero entries equate 1 [56]. The Z-tensor is constructed as usual (equations (41) and (42)), where the deformation acts as string tension. The use of Appendix A.2 simplifies the bond dimension from $d = 64$ to $d = 13$. We find that Corollary 1 does not hold, so that, unlike for all the previous cases, $S_{1/2}$ is not appropriate. Notably, even if it were

possible to make Corollary 1 hold, the result cannot be made satisfactory: The multiplicity of the largest eigenvalue of X_1 is 13, so that the best possible value for $S_{1/2}^{\text{topo}}$ is $\ln\left(\frac{13}{4}\right) \approx 1.17865$, which is quite far from the actual value of the TEE. (In fact, if one were to ignore that Corollary 1 doesn't hold and calculated $S_{1/2}^{\text{topo}}$ regardlessly, this would be the obtained value.) The solution is to step up to the next higher integer order S_2.

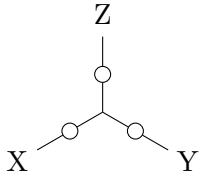

Figure 43: The honeycomb lattice has links (hosting spins represented through circles) pointing in three different directions, that we label X,Y, and Z.

The phase transition is illustrated through the TEE in Fig. 44, the determined value $\ln\left(\frac{610}{169}\right)$ is not exact but is satisfactory close with a relative error of 0.2%. Possibly higher-order Rényi entropies can approximate the true value even closer, whereas obtaining the true value is not possible, as discussed in Remark 5. The fluctuations towards the critical point can probably be mitigated by taking even larger χ with larger space and computational resources. The reduced fidelity in Fig. 45 finds the critical point to be identical to Ref. [56] up to a relative error of 0.04%.

Topological Entanglement Entropy across the Phase Transition for the Double Fibonacci Model on the Honeycomb Lattice

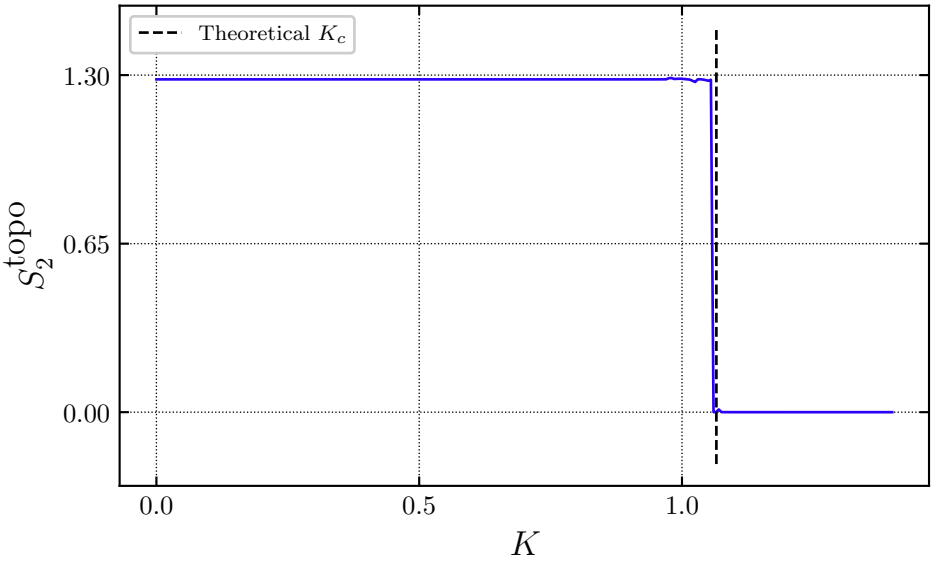

Figure 44: The TEE remains constant and equal to $\ln\left(\frac{610}{169}\right) \approx 1.28356$ up to the critical point (up to small fluctuations towards the critical point), which coincides with the critical point determined by Xu et al. $K_c = \ln(1+\sqrt{2+\phi}) \approx 1.06544$, where ϕ is the golden ratio. At the critical point, it drops sharply to zero. (The plot generation took 2.5 h, with $N = 500$, $L = 4000$, $\chi = 160$ and K in steps of 0.005 in the vicinity of the critical point and $\chi = 80$ and K in steps of 0.02 far from the critical point.)

Reduced Fidelity across the Phase Transition for the Double Fibonacci Model on the Honeycomb Lattice

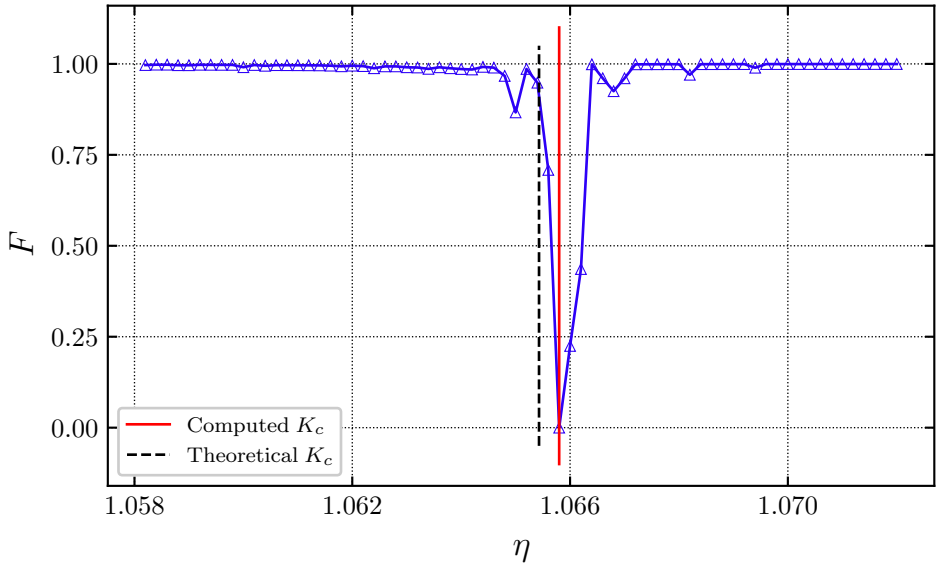

Figure 45: The partial fidelity dips around the critical point determined by Xu et al. The critical point found through the fidelity is $\eta_c = 1.0658 \pm 0.0002$. (The plot generation took 125 min, with $N = 500$, $L = 2048$, $\chi = 100$, and K in steps of 0.0002.)

5 Discussion and Conclusion

In this thesis, we successfully harvest the area law to construct an efficient numerical approach to topological phase transitions on 2D lattice gauge theories. Our approach relies on the holographic principle and translation invariance highlighted by string-net states to encode the bulk information of tensor network states through dominant vectors. The reduced density matrix is accessed readily through the dominant vectors, as is shown in Theorem 1. To efficiently obtain the dominant vectors and RDM, we devise what is essentially an iTEBD algorithm, which recasts these objects as infinite matrix product states. We showed that a sufficient set of physical quantities necessary to characterize topological phases and transitions, specifically the topological entanglement entropy, reduced fidelity, string order parameters, critical exponents, and central charge, can be accessed only from the RDM, respectively, from the dominant vectors. Effectively, the computation of these quantities, which usually require the contraction of 2D TPSs and are exponentially complex in system size, is reduced to contractions of infinite MPSs

with periodic boundary conditions, which are tractable in polynomial time. This promises a substantial reduction in complexity and run-times.

Moreover, our method is perfectly attuned to large systems (of width N and length L) and to the thermodynamic limit. The exact dominant vectors in the thermodynamic limit differ from the numerically determined dominant vectors by an exponentially suppressed error in system width N. Analogously, any of the studied quantities only depends on the largest eigenvalues (and their multiplicities) of local contractions of the tensors that constitute the dominant vectors, hence these too asymptotically approach the thermodynamic limit at large L. It is especially reassuring that complexity scales at most linearly in L and N. The reliance on maximal eigenvalues enables further acceleration of run-times.

We tested our approach for a variety of Abelian and non-Abelian phases and phase transitions of high relevance in the physics community, specifically, on the Toric Code, Double Semion, and Double Fibonacci models. The topological entanglement entropy is successfully implemented through linear regression on low-order Rényi entropies with exact results in the case of Abelian phases and near-exact values for non-Abelian phases, which is expected as of Remark 5. We found that the reduced fidelity allows us to determine the critical point with marvelous accuracy. We trialed the Fredenhagen-Marcu order parameter to generate the phase diagram of the deformation of the Toric Code and found that the TEE approach confirms this diagram. Furthermore, we determined the universal properties of the phase transitions with satisfying accuracy. In particular, we generalized a known phase transition on the Toric Code to the honeycomb and triangular lattice and found that the Double Semion model with the same deformation is subject to the same phase transition in the universality class of the classical 2D Ising model.

The run-times are dominated by the bond dimension d of the Z-tensor and the virtual bond dimension χ of the dominant vectors MPS. In particular, the iTEBD update steps have complexity $O(d^3\chi^3)$ while contractions of quantities are also polynomial in d and χ. Heuristically, we find that our technique produces stable and accurate results if $\chi \geq 5d$ away from and $\chi \geq 10d$ close to criticality. Whereas, χ primarily influences the behavior of the correlation length at criticality. Complexity is linear in N and L, the constraints set by these parameters are less strict, as the exponential suppression assures that the error is reduced quickly. Setting $N \approx 500$ and $L \approx 1000$ gave appropriate results across the board. In extreme proximity to the critical point, the behavior of the TEE is governed through the system size, pointing to a perfectly sharp transition in the thermodynamic limit. Notably, the $\ln(\xi)$

v. $\ln|\eta_c - \eta|$ plots needed larger N and N_u to assure that the central charge has converged fairly close towards the true value. This behavior stems from how the correlation length is determined

$$\ln(\xi) \propto \ln(\ln(x)), \tag{134}$$

where $x = e_0/e_1$ is the fraction of the largest two eigenvalues of the transfer matrix $\mathcal{T}$. Since x is very close to 1 at criticality, small fluctuations in the dominant vector coerce $\ln(\xi)$ to suffer from large discrepancies, due to the asymptotic behavior as $x \to 1$. Nonetheless, run-times in general are manageable for the considered models, remarkably so, as all of the computations were run on personal hardware.

Often, the naive TN representation of the deformed states is not optimal, that is, d is inflated unnecessarily. To mitigate this bloat is substantial in order to keep run-times low, two approaches towards this end are elaborated in Appendix A.

Naturally, certain questions and some further exploration remain uncharted territory. It is of intrinsic interest to put an analytic bound on the error of our approach committed through truncating singular values at a fixed χ. Especially, to understand how this error reflects in the specific calculated quantities. These bounds are understood to an extent in the context of the iTEBD algorithm [82], and have also been explored in the context of writing ground states of 1D gapped local Hamiltonians as MPSs [110, 79, 111, 80, 112]. These approaches rely on exponential decaying correlation, bound entanglement entropy, or the gappedness of the local Hamiltonian, conditions, which are typically violated during a phase transition. Moreover, even far from criticality, it is desirable to understand these bounds better by investigating what 1D "Hamiltonians" the 2D TNS is mapped to through the Z-tensor in equation (66).

From a computational perspective, it is desirable to replace the iTEBD with DMRG [83, 84, 85] or VUMPS [89] and to benchmark the algorithms against each other. Typically, DMRG and VUMPS need fewer iterations to arrive at an MPS that minimizes error, the thermodynamic limit is reached more quickly. On the other hand, iTEBD is the only algorithm for which the iteration number can be interpreted as the system size, as the other two do not apply tensors but minimize energy.

Another consideration is directly linked to this 2D state to 1D "Hamiltonian" mapping, namely, whether the 1D ground state of this Hamiltonian (i.e., the dominant vector) is subject to the same phase transition, and whether the

corresponding 1D physical systems are of interest. This corresponds to checking the previously elaborated 2D to 1D phase transition correspondence.

The fidelity approach to phase transitions also offers insights into the universality class through finite scaling of the fidelity susceptibility [94]. Whether this pathway also leads to efficient and accurate results is still up for exploration.

We discussed multiple times the fixed-point nature of the Levin-Wen states. The RG argument at its base is also enshrined in the tensor network description and has been elaborated into the *Tensor-Entanglement Renormalization Group approach* (TERG) to efficiently contract 2D tensor networks [113, 52]. TERG naturally leads deformed states back to the fixed-point, whereas we found that for these fixed-point states, the dominant vector would always turn out with $\chi = d$. Any more singular values are so vanishingly small that they are always truncated by iTEBD, even if the set limit on singular values has not been exhausted. This much more efficient bound on χ could be exploited through a first evolution of our approach: (1) a set number of TERG steps sends a deformed state to the fixed-point of its phase, (2) the dominant vector of the fixed point is determined, (3) from the dominant vector, the TEE can be calculated more efficiently. Clearly, this is only viable in order to calculate the TEE, as the properties of criticality are lost, and the reduced fidelity loses meaning. It is unclear how the boundary MPS at the initialization of the iTEBD would have to be adapted for this procedure.

More fundamental questions are whether our method can be adapted beyond lattice gauge theories or whether it grants insight into the continuum limit.

Notoriously, in many-body physics, *more is always different*. In the case of much greater d (or precision), it is advisable to pass to more appropriate hardware like clusters. Unfortunately, it seems that the essence of our approach is hard (if not impossible) to transfer to greater spatial dimensions. The holographic principle encodes the information of nD systems into structures of $n-1$ dimensions; only MPSs are contracted efficiently, which sets a natural boundary on the system dimension.

In conclusion, we have achieved a viable, efficient, and easy-to-implement expansion to existing methods in the field of topological phase transitions on 2D spin lattices. Current methods rely on mapping the topological phase transitions onto known transitions [43, 55], the correlation length [54], or anyon condensate and deconfinement fractions [56]. Our method complements these through the computation of the topological entanglement entropy and reduced fidelity. Moreover, alternative pathways to the correlation length, global order

parameters, and the universal critical properties are offered. The approach promises further improvements in efficiency and precision and additional exploration of quantities relevant to topological phase transitions, especially due to its heavy reliance on MPSs, which are generally well-understood.

Acknowledgment

Being able to conduct research and to obtain a degree are far from commonplace; in fact, these are often a product of being in a position of relative privilege. Privilege I am fortunate enough to enjoy, as such, only a fraction of this work's credit belongs to me.

I acknowledge and am thankful for the outstanding guidance and supervision by Prof. Dr. Frank Pollmann and his tireless engagement, which turned this work into an exceptional learning experience.

I am deeply indebted to Dr. Wen-Tao Xu for being immensely resourceful and guiding me through various struggles.

I want to thank Prof. Dr. David Pérez-García for two magnificent lectures on entanglement and tensor network states and for two very kind and enlightening discussions.

I am grateful to Prof. Dr. Adolfo del Campo and Prof. Dr. Jing Yang for getting me excited about anyons and, by extension, about topological phases.

The typographic style is inspired by a thesis by Julen Simón Pedernales. The LaTeX arrangement is adapted from a template by Iagoba Apellaniz. The bibliographic style was created by Sofía Martínez-Garaot.

I will forever be grateful to my parents for setting ablaze my curiosity and passion for natural sciences, for nourishing the flame throughout the years, and for supporting me unconditionally in my endeavor to become a physicist.

I want to thank my partner, Ven, for their patience, compassion, and support, especially throughout the more stressful parts of finishing this work and degree.

Appendices

A Optimizing the Z-Tensor

The bond dimension d of the Z-tensor dominates (together with χ) the complexity of the algorithm. Thus, assuring that Z minimizes d is powerful in keeping run-times short. The two paradigms used in this work depart from the known TN description of the Levin-Wen states and merely rely on reducing bloat, that is, removing copies or "0-Subspaces" from Z.

A.1 Removing Copies

For a single-line g-tensor (associated with $M+1$ spin states)

$$g^m_{\alpha\alpha'} = \delta_{m\alpha}\delta_{\alpha\alpha'} \tag{135}$$

the virtual indices α and α' mirror the physical index m. The double-layer tensor

$$\begin{aligned} G^{\alpha\alpha'}_{\tilde{\alpha}\tilde{\alpha}'} &= \sum_m g^m_{\alpha\alpha'} g^m_{\tilde{\alpha}\tilde{\alpha}'} && (136)\\ &= \delta_{\alpha\tilde{\alpha}}\delta_{\alpha\alpha'}\delta_{\tilde{\alpha}\tilde{\alpha}'} && (137)\\ &= \delta_{\alpha\tilde{\alpha}}\delta_{\alpha\alpha'}\delta_{\alpha'\tilde{\alpha}'} && (138) \end{aligned}$$

arises naturally from the contraction over the physical links when assembling the Z-tensor. Viewing $\alpha\tilde{\alpha}$ and $\alpha'\tilde{\alpha}'$ as singular indices each turns G into a matrix acting as a projecion. On each lattice bond, G can be doubled without changing the TN encoding the traced out region (see Fig. 46). The Z-tensors (on the square lattice) follow from contracting on each vertex the T-tensors with one of the G-tensors per link:

$$\mathrm{Z}_{\alpha\tilde{\alpha};\beta\tilde{\beta};\gamma\tilde{\gamma};\mu\tilde{\mu}} = \sum_{\substack{\alpha'\beta'\gamma'\mu'\\ \tilde{\alpha}'\tilde{\beta}'\tilde{\gamma}'\tilde{\mu}'}} G^{\alpha\alpha'}_{\tilde{\alpha}\tilde{\alpha}'} G^{\beta\beta'}_{\tilde{\beta}\tilde{\beta}'} G^{\gamma\gamma'}_{\tilde{\gamma}\tilde{\gamma}'} G^{\mu\mu'}_{\tilde{\mu}\tilde{\mu}'} T_{\alpha'\beta'\gamma'\mu'} T^*_{\tilde{\alpha}'\tilde{\beta}'\tilde{\gamma}'\tilde{\mu}'}. \tag{139}$$

The Kronecker delta in the G-tensors forces the upper (untilted) and lower (tilted) virtual indices to be equal, and one can write

$$\mathrm{Z}_{\alpha\tilde{\alpha};\beta\tilde{\beta};\gamma\tilde{\gamma};\mu\tilde{\mu}} = \delta_{\alpha\tilde{\alpha}}\delta_{\beta\tilde{\beta}}\delta_{\gamma\tilde{\gamma}}\delta_{\mu\tilde{\mu}}\tilde{\mathrm{Z}}_{\alpha\beta\gamma\mu}, \tag{140}$$

with

$$\tilde{\mathrm{Z}}_{\alpha\beta\gamma\mu} = T_{\alpha\beta\gamma\mu}T^{*}_{\alpha\beta\gamma\mu}. \tag{141}$$

Evidently, all the information of the TN is contained in $\tilde{\mathrm{Z}}$; Z is bloated as it contains $M+1$ copies of each spin state. Thus, running the iTEBD on $\tilde{\mathrm{Z}}$ gives a much more favorable bond dimension of $d = M+1$ instead of $d = (M+1)^2$.

This statement can be extrapolated to any other lattice geometry, as it only relies on the condition that upper and lower virtual indices are identical. In the case of deformed states, extra care must be taken to ensure the deformation preserves this condition (e.g., string tension preserves this).

The contractions of quantities (like TEE, reduced fidelity, ...) need to be adapted accordingly, or the Kronecker deltas must be reintroduced into the dominant vectors through an intermediate step after the iTEBD. Moreover, the definition of the boundary MPS must be altered to fit in with this reduction.

Notice that this property enforces the dominant vectors to be diagonal in upper and lower indices.

A.2 Removing 0-Subspaces

The Z-tensor acts as zero on a substantially sized subspace, that is, $\exists\mathcal{V} \subset \{0,\ldots,M\}$ a subset of the range of the indices, s.t. $\forall i \in \mathcal{V}; \forall j,k,l \in \{0,\ldots,M\}$

$$\mathrm{Z}_{ijkl} = \mathrm{Z}_{jikl} = \mathrm{Z}_{jkil} = \mathrm{Z}_{jkli} = 0. \tag{142}$$

Physically, this subspace corresponds to the illegal recombinations of string types or, alternatively, to the unphysical fusions of fluxes. The entries of the dominant vectors corresponding to this subspace are all sent trivially to zero through the iTEBD, so that we can ignore these indices. A substantial reduction in the bond dimension d is achieved by removing this subspace from the range of indices (e.g., going from $d = 64$ to $d = 13$ for the DFib model).

This optimization is possible regardless of lattice geometry, deformation, or whatever the number of lines of the tensors is.

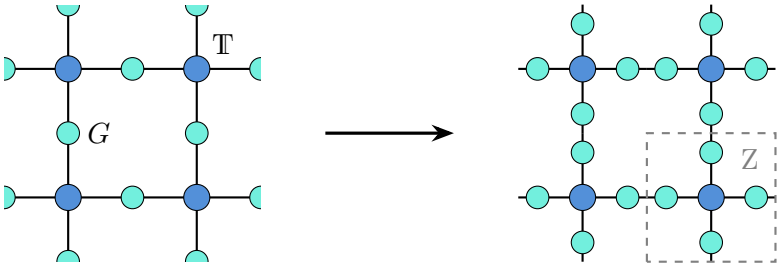

(a) (b)

Figure 46: (a) On the square lattice, the traced-out region consists of double-layer tensors G on the links and $\mathbb{T} = T \otimes T$ on the vertices. (b) The G-tensors have been doubled/split on each link, Z is assembled as the contraction of $\mathbb{T}$ with the closest G on each link. (This process corresponds to Fig. 13 that leads to equations (44) and (45), but on the double-layer TN, as the physical indices were contracted first).

Careful book-keeping is necessary to assure the boundary MPS at initialization is defined and the calculation of quantities is performed correctly.

B Derivations of the Z-Tensors

B.1 TC on the Square Lattice

The tensors that define the Toric Code ground state on the square lattice

$$g^m_{\alpha\alpha'} = \delta_{m\alpha}\delta_{\alpha\alpha'} \tag{143}$$

$$T_{\alpha\beta\gamma\mu} = \begin{cases} 1 \text{ if } \alpha+\beta+\gamma+\mu \text{ even} \\ 0 \text{ if } \alpha+\beta+\gamma+\mu \text{ odd} \end{cases} \tag{144}$$

are given in **II.** of Ref. [52], the indices run over $\{0,1\}$. The considered deformation acts locally as

$$O(\eta) = e^{\frac{\eta}{2}\sigma^z}. \tag{145}$$

Contracting the double-layer tensor, as they occur on each link, and including the deformation gives

$$G^{\alpha\alpha'}_{\tilde{\alpha}\tilde{\alpha}'}(\eta) = \sum_{m,n,k} g^m_{\alpha\alpha'} O_{mn}(\eta) O_{nk}(\eta) g^k_{\tilde{\alpha}\tilde{\alpha}'} \tag{146}$$

$$= \tau_\alpha(\eta)\delta_{\alpha\tilde{\alpha}}\delta_{\alpha\alpha'}\delta_{\alpha'\tilde{\alpha}'} \tag{147}$$

$$= \tau_\alpha(\eta) G^{\alpha\alpha'}_{\tilde{\alpha}\tilde{\alpha}'}, \tag{148}$$

with G the tensor in eqn. (138) and string tension

$$\tau(\eta) = \begin{pmatrix} e^{\eta} \\ e^{-\eta} \end{pmatrix}. \tag{149}$$

As the G-tensor is a projector

$$G(\eta) = \left[G\left(\frac{\eta}{2}\right) \right]^2, \tag{150}$$

$G(\eta)$ can be split into two tensors $G(\frac{\eta}{2})$ (viewing $\alpha\tilde{\alpha}$ and $\alpha'\tilde{\alpha}'$ as singular indices each), as is shown in Fig. 46. In each vertex, the Z-tensors results from contracting the T-tensors with one of the two $G(\frac{\eta}{2})$ per link:

$$\begin{aligned}\mathrm{Z}_{\alpha\tilde{\alpha};\beta\tilde{\beta};\gamma\tilde{\gamma};\mu\tilde{\mu}}(\eta) = \sum_{\substack{\alpha'\beta'\gamma'\mu'\\ \tilde{\alpha}'\tilde{\beta}'\tilde{\gamma}'\tilde{\mu}'}} \Bigg[& G^{\alpha\alpha'}_{\tilde{\alpha}\tilde{\alpha}'}\left(\frac{\eta}{2}\right) G^{\beta\beta'}_{\tilde{\beta}\tilde{\beta}'}\left(\frac{\eta}{2}\right) G^{\gamma\gamma'}_{\tilde{\gamma}\tilde{\gamma}'}\left(\frac{\eta}{2}\right) \\ & G^{\mu\mu'}_{\tilde{\mu}\tilde{\mu}'}\left(\frac{\eta}{2}\right) T_{\alpha'\beta'\gamma'\mu'} T^*_{\tilde{\alpha}'\tilde{\beta}'\tilde{\gamma}'\tilde{\mu}'} \Bigg].\end{aligned} \tag{151}$$

The deformed tensor $G(\eta)$ highlights the property used in Appendix A.1, performing the same optimization gives

$$\begin{aligned}\tilde{\mathrm{Z}}_{\alpha\beta\gamma\mu}(\eta) &= \tau_\alpha\left(\frac{\eta}{2}\right)\tau_\beta\left(\frac{\eta}{2}\right)\tau_\gamma\left(\frac{\eta}{2}\right)\tau_\mu\left(\frac{\eta}{2}\right) T_{\alpha\beta\gamma\mu} T^*_{\alpha\beta\gamma\mu} && (152)\\ &= \tau_\alpha\left(\frac{\eta}{2}\right)\tau_\beta\left(\frac{\eta}{2}\right)\tau_\gamma\left(\frac{\eta}{2}\right)\tau_\mu\left(\frac{\eta}{2}\right) T_{\alpha\beta\gamma\mu}, && (153)\end{aligned}$$

which equals the tensor in equation (112) up to a multiplication by $e^{2\eta}$. Overall multiplicative constants are irrelevant, as the iTEBD restores normalization on each update.

B.2 TC on the Honeycomb Lattice

The Toric Code on the honeycomb lattice is defined analogously to the previous section, with the modification

$$T_{\alpha\beta\gamma} = \begin{cases} 1 \text{ if } \alpha+\beta+\gamma \text{ even} \\ 0 \text{ if } \alpha+\beta+\gamma \text{ odd} \end{cases} \tag{154}$$

into a rank-3 tensor, which is identical on both sublattices. The same splitting procedure gives for Z the contraction in Fig. 47. The simplification from Appendix A.1 results in the optimized tensor

$$\begin{aligned}&\tilde{\mathrm{Z}}_{\alpha\beta\gamma\mu}(\eta) \\ &= \sum_\nu \tau_\alpha\left(\frac{\eta}{2}\right)\tau_\beta\left(\frac{\eta}{2}\right) T_{\alpha\beta\nu} T^*_{\alpha\beta\nu}\tau_\nu(\eta) T_{\nu\gamma\mu} T^*_{\nu\gamma\nu}\tau_\gamma\left(\frac{\eta}{2}\right)\tau_\mu\left(\frac{\eta}{2}\right) && (155)\\ &= \sum_\nu \tau_\alpha\left(\frac{\eta}{2}\right)\tau_\beta\left(\frac{\eta}{2}\right) T_{\alpha\beta\nu}\tau_\nu(\eta) T_{\nu\gamma\mu}\tau_\gamma\left(\frac{\eta}{2}\right)\tau_\mu\left(\frac{\eta}{2}\right), && (156)\end{aligned}$$

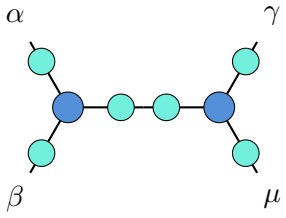

Figure 47: Contraction that gives the Z-tensor for the Toric Code on the honeycomb lattice.

which is identical to equations (116)-(118) up to a multiplication by e^{η}.

B.3 TC on the Triangular Lattice

On the triangular lattice, the T-tensor is rank-6

$$T_{\alpha\beta\gamma\mu\nu\lambda} = \begin{cases} 1 \text{ if } \alpha+\beta+\gamma+\mu+\nu+\lambda \text{ even} \\ 0 \text{ if } \alpha+\beta+\gamma+\mu+\nu+\lambda \text{ odd} \end{cases} . \tag{157}$$

Notice that

$$T_{\alpha\beta\gamma\mu\nu\lambda} = \sum_{\sigma} \Gamma_{\alpha\beta\gamma\sigma}\Gamma_{\sigma\mu\nu\lambda}, \tag{158}$$

where

$$\Gamma_{\alpha\beta\gamma\sigma} = \begin{cases} 1 \text{ if } \alpha+\beta+\gamma+\sigma \text{ even} \\ 0 \text{ if } \alpha+\beta+\gamma+\sigma \text{ odd} \end{cases} . \tag{159}$$

This decomposition could be obtained naively from an SVD (see Fig. 15b); however, it is trivial to deduce the decomposition directly from the branching rules (all loops must be closed on the TC): Remember that the T-tensor enforces the branching rules in all vertices. Moreover, the choice of g directly translates an index 0 into the corresponding link being unoccupied, while an index equal to 1 corresponds to a string. If $\alpha+\beta+\gamma$ is even, then only for $\sigma = 0$ can Γ be non-zero without violating the condition. The converse statement is also true; if the sum is odd, Γ can only be non-zero for $\sigma = 1$.

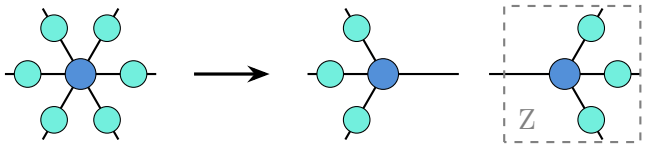

(a) (b)

Figure 48: (a) The local contraction of tensors on the honeycomb lattice after splitting the G-tensors. (b) The decomposition in (158) gives one bond without string tension.

Splitting, contracting, and using Appendix A.1 (as previously) achieves the optimized tensor

$$\tilde{\mathrm{Z}}_{\alpha\beta\gamma\mu}(\eta) = \tau_\beta\left(\frac{\eta}{2}\right)\tau_\gamma\left(\frac{\eta}{2}\right)\tau_\delta\left(\frac{\eta}{2}\right)\Gamma_{\alpha\beta\gamma\mu}\Gamma^*_{\alpha\beta\gamma\mu} \tag{160}$$

$$= \tau_\beta\left(\frac{\eta}{2}\right)\tau_\gamma\left(\frac{\eta}{2}\right)\tau_\delta\left(\frac{\eta}{2}\right)\Gamma_{\alpha\beta\gamma\mu}, \tag{161}$$

which equates the tensor defined in equations (119)-(122) up to a multiplication by $e^{\frac{3}{2}\eta}$.

Notice that only three of the four indices are paired with a string tension: The first index originates from the decomposition, which is not occupied by G-tensors (see Fig. 48). Essentially, the decomposition results in two distinct Z-tensors that are linked through a transposition. The iTEBD can then be performed on one of the Z-tensors, transposing between every update. The condition necessary to use Appendix A.1 still emerges: The Kronecker deltas act on three of the bonds of the double-layered tensor $\Gamma \otimes \Gamma$, which enforces the resulting tensor to equal null if the fourth set of indices isn't equal.

Bibliography

[1] L. Landau, *"The Theory of Phase Transitions"*, Nature **138**, 840–841 (1936).

[2] P. Hohenberg and A. Krekhov, *"An introduction to the Ginzburg–Landau theory of phase transitions and nonequilibrium patterns"*, Phys. Rep. **572**, 1-42 (2015).

[3] J. M. Kosterlitz and D. J. Thouless, *"Ordering, metastability and phase transitions in two-dimensional systems"*, J. Phys. C **6**, 1181 (1973).

[4] K. v. Klitzing, G. Dorda, and M. Pepper, *"New Method for High-Accuracy Determination of the Fine-Structure Constant Based on Quantized Hall Resistance"*, Phys. Rev. Lett. **45**, 494–497 (1980).

[5] D. C. Tsui, H. L. Stormer, and A. C. Gossard, *"Two-Dimensional Magnetotransport in the Extreme Quantum Limit"*, Phys. Rev. Lett. **48**, 1559–1562 (1982).

[6] D. J. Thouless, M. Kohmoto, M. P. Nightingale, and M. den Nijs, *"Quantized Hall Conductance in a Two-Dimensional Periodic Potential"*, Phys. Rev. Lett. **49**, 405–408 (1982).

[7] R. B. Laughlin, *"Anomalous Quantum Hall Effect: An Incompressible Quantum Fluid with Fractionally Charged Excitations"*, Phys. Rev. Lett. **50**, 1395–1398 (1983).

[8] D. Arovas, J. R. Schrieffer, and F. Wilczek, *"Fractional Statistics and the Quantum Hall Effect"*, Phys. Rev. Lett. **53**, 722–723 (1984).

[9] G. Moore and N. Read, *"Nonabelions in the fractional quantum hall effect"*, Nucl. Phys. B **360**, 362-396 (1991).

[10] X. G. Wen, *"Non-Abelian statistics in the fractional quantum Hall states"*, Phys. Rev. Lett. **66**, 802–805 (1991).

[11] J. M. Leinaas and J. Myrheim, *"On the theory of identical particles"*, Il Nuovo Cimento B (1971-1996) **37**, 1–23 (1977).

[12] F. Wilczek, *"Magnetic Flux, Angular Momentum, and Statistics"*, Phys. Rev. Lett. **48**, 1144–1146 (1982).

[13] F. Wilczek, *"From electronics to anyonics"*, Physics World **19**, 22 (2006).

[14] S. M. Girvin, *"The Quantum Hall Effect: Novel Excitations and Broken Symmetries"*, 1999. https://arxiv.org/abs/cond-mat/9907002.

[15] D. Tong, *"Lectures on the Quantum Hall Effect"*, 2016. https://arxiv.org/abs/1606.06687.

[16] F. D. M. Haldane, *"Model for a Quantum Hall Effect without Landau Levels: Condensed-Matter Realization of the "Parity Anomaly""*, Phys. Rev. Lett. **61**, 2015–2018 (1988).

[17] C. L. Kane and E. J. Mele, *"Z_2 Topological Order and the Quantum Spin Hall Effect"*, Phys. Rev. Lett. **95**, 146802 (2005).

[18] C. L. Kane and E. J. Mele, *"Quantum Spin Hall Effect in Graphene"*, Phys. Rev. Lett. **95**, 226801 (2005).

[19] R. S. K. Mong and V. Shivamoggi, *"Edge states and the bulk-boundary correspondence in Dirac Hamiltonians"*, Phys. Rev. B **83**, 125109 (2011).

[20] L. Fidkowski, T. S. Jackson, and I. Klich, *"Model Characterization of Gapless Edge Modes of Topological Insulators Using Intermediate Brillouin-Zone Functions"*, Phys. Rev. Lett. **107**, (2011).

[21] M. König, S. Wiedmann, C. Brüne, A. Roth, H. Buhmann, L. W. Molenkamp, X.-L. Qi, and S.-C. Zhang, *"Quantum Spin Hall Insulator State in HgTe Quantum Wells"*, Science **318**, 766–770 (2007).

[22] D. Hsieh, Y. Xia, D. Qian, L. Wray, J. H. Dil, F. Meier, J. Osterwalder, L. Patthey, J. G. Checkelsky, N. P. Ong, A. V. Fedorov, H. Lin, A. Bansil, D. Grauer, Y. S. Hor, R. J. Cava, and M. Z. Hasan, *"A tunable topological insulator in the spin helical Dirac transport regime"*, Nature **460**, 1101–1105 (2009).

[23] M. Z. Hasan and C. L. Kane, *"Colloquium: Topological insulators"*, Rev. Mod. Phys. **82**, 3045–3067 (2010).

[24] B. Yan and S.-C. Zhang, *"Topological materials"*, Rep. Prog. Phys. **75**, 096501 (2012).

[25] A. M. Turner and A. Vishwanath, *"Beyond Band Insulators: Topology of Semi-metals and Interacting Phases"*, 2013. https://arxiv.org/abs/1301.0330.

[26] N. Armitage, E. Mele, and A. Vishwanath, *"Weyl and Dirac semimetals in three-dimensional solids"*, Rev. Mod. Phys. **90**, (2018).

[27] J. Alicea, *"New directions in the pursuit of Majorana fermions in solid state systems"*, Rep. Prog. Phys. **75**, 076501 (2012).

[28] C.-K. Chiu, J. C. Teo, A. P. Schnyder, and S. Ryu, *"Classification of topological quantum matter with symmetries"*, Rev. Mod. Phys. **88**, (2016).

[29] M. H. Freedman, *"P/NP, and the quantum field computer"*, Proceedings of the National Academy of Sciences **95**, 98-101 (1998).

[30] M. H. Freedman, A. Kitaev, M. J. Larsen, and Z. Wang, *"Topological Quantum Computation"*, 2002. https://arxiv.org/abs/quant-ph/0101025.

[31] A. Kitaev, *"Fault-tolerant quantum computation by anyons"*, Ann. Phys. **303**, 2-30 (2003).

[32] A. Kitaev and C. Laumann, *"Topological phases and quantum computation"*, 2009. https://arxiv.org/abs/0904.2771.

[33] A. Hamma, R. Ionicioiu, and P. Zanardi, *"Ground state entanglement and geometric entropy in the Kitaev model"*, Phys. Lett. A **337**, 22–28 (2005).

[34] X. G. Wen, *"Topological Orders in Rigid States"*, Int. J. Mod. Phys. B **04**, 239-271 (1990).

[35] X. G. Wen and Q. Niu, *"Ground-state degeneracy of the fractional quantum Hall states in the presence of a random potential and on high-genus Riemann surfaces"*, Phys. Rev. B **41**, 9377–9396 (1990).

[36] H. Li and F. D. M. Haldane, *"Entanglement Spectrum as a Generalization of Entanglement Entropy: Identification of Topological Order in Non-Abelian Fractional Quantum Hall Effect States"*, Phys. Rev. Lett. **101**, (2008).

[37] X. Chen, Z.-C. Gu, and X.-G. Wen, *"Local unitary transformation, long-range quantum entanglement, wave function renormalization, and topological order"*, Phys. Rev. B **82**, 155138 (2010).

[38] Y. Zhang, T. Grover, A. Turner, M. Oshikawa, and A. Vishwanath, *"Quasiparticle statistics and braiding from ground-state entanglement"*, Phys. Rev. B **85**, 235151 (2012).

[39] A. Kitaev and J. Preskill, *"Topological Entanglement Entropy"*, Phys. Rev. Lett. **96**, 110404 (2006).

[40] M. Levin and X.-G. Wen, *"Detecting Topological Order in a Ground State Wave Function"*, Phys. Rev. Lett. **96**, 110405 (2006).

[41] K. J. Satzinger, Y.-J. Liu, A. Smith, C. Knapp, M. Newman, C. Jones, Z. Chen, C. Quintana, X. Mi, A. Dunsworth, C. Gidney, I. Aleiner, F. Arute, K. Arya, J. Atalaya, R. Babbush, J. C. Bardin, R. Barends, J. Basso, A. Bengtsson, A. Bilmes, M. Broughton, B. B. Buckley, D. A. Buell, B. Burkett, N. Bushnell, B. Chiaro, R. Collins, W. Courtney, S. Demura, A. R. Derk, D. Eppens, C. Erickson, L. Faoro, E. Farhi, A. G. Fowler, B. Foxen, M. Giustina, A. Greene,

J. A. Gross, M. P. Harrigan, S. D. Harrington, J. Hilton, S. Hong, T. Huang, W. J. Huggins, L. B. Ioffe, S. V. Isakov, E. Jeffrey, Z. Jiang, D. Kafri, K. Kechedzhi, T. Khattar, S. Kim, P. V. Klimov, A. N. Korotkov, F. Kostritsa, D. Landhuis, P. Laptev, A. Locharla, E. Lucero, O. Martin, J. R. McClean, M. McEwen, K. C. Miao, M. Mohseni, S. Montazeri, W. Mruczkiewicz, J. Mutus, O. Naaman, M. Neeley, C. Neill, M. Y. Niu, T. E. O'Brien, A. Opremcak, B. Pató, A. Petukhov, N. C. Rubin, D. Sank, V. Shvarts, D. Strain, M. Szalay, B. Villalonga, T. C. White, Z. Yao, P. Yeh, J. Yoo, A. Zalcman, H. Neven, S. Boixo, A. Megrant, Y. Chen, J. Kelly, V. Smelyanskiy, A. Kitaev, M. Knap, F. Pollmann, and P. Roushan, *"Realizing topologically ordered states on a quantum processor"*, Science **374**, 1237–1241 (2021).

[42] M. A. Levin and X.-G. Wen, *"String-net condensation: A physical mechanism for topological phases"*, Phys. Rev. B **71**, 045110 (2005).

[43] C. Castelnovo and C. Chamon, *"Quantum topological phase transition at the microscopic level"*, Phys. Rev. B **77**, (2008).

[44] F. Verstraete, M. M. Wolf, D. Perez-Garcia, and J. I. Cirac, *"Criticality, the Area Law, and the Computational Power of Projected Entangled Pair States"*, Phys. Rev. Lett. **96**, (2006).

[45] D. Perez-Garcia, F. Verstraete, M. M. Wolf, and J. I. Cirac, *"Matrix Product State Representations"*, 2007. https://arxiv.org/abs/quant-ph/0608197.

[46] N. Schuch, D. Pérez-García, and I. Cirac, *"Classifying quantum phases using matrix product states and projected entangled pair states"*, Phys. Rev. B **84**, (2011).

[47] R. Orús, *"A practical introduction to tensor networks: Matrix product states and projected entangled pair states"*, Ann. Phys. **349**, 117–158 (2014).

[48] J. Biamonte and V. Bergholm, *"Tensor Networks in a Nutshell"*, 2017. https://arxiv.org/abs/1708.00006.

[49] J. Hauschild and F. Pollmann, *"Efficient numerical simulations with Tensor Networks: Tensor Network Python (TeNPy)"*, SciPost Phys. Lect. Notes 5 (2018).

[50] J. I. Cirac, D. Pérez-García, N. Schuch, and F. Verstraete, *"Matrix product states and projected entangled pair states: Concepts, symmetries, theorems"*, Rev. Mod. Phys. **93**, (2021).

[51] D. Perez-Garcia, F. Verstraete, J. I. Cirac, and M. M. Wolf, *"PEPS as unique ground states of local Hamiltonians"*, 2007. https://arxiv.org/abs/0707.2260.

[52] Z.-C. Gu, M. Levin, B. Swingle, and X.-G. Wen, *"Tensor-product representations for string-net condensed states"*, Phys. Rev. B **79**, (2009).

[53] N. Schuch, D. Poilblanc, J. I. Cirac, and D. Pérez-García, *"Topological Order in the Projected Entangled-Pair States Formalism: Transfer Operator and Boundary Hamiltonians"*, Phys. Rev. Lett. **111**, (2013).

[54] W.-T. Xu and G.-M. Zhang, *"Tensor network state approach to quantum topological phase transitions and their criticalities of $\mathbb{Z}_2$ topologically ordered states"*, Phys. Rev. B **98**, (2018).

[55] W.-T. Xu, Q. Zhang, and G.-M. Zhang, *"Tensor Network Approach to Phase Transitions of a Non-Abelian Topological Phase"*, Phys. Rev. Lett. **124**, (2020).

[56] W.-T. Xu and N. Schuch, *"Characterization of topological phase transitions from a non-Abelian topological state and its Galois conjugate through condensation and confinement order parameters"*, Phys. Rev. B **104**, 155119 (2021).

[57] W.-T. Xu, F. Pollmann, and M. Knap, *"Critical behavior of Fredenhagen-Marcu string order parameters at topological phase transitions with emergent higher-form symmetries"*, npj Quantum Information **11**, (2025).

[58] J. I. Cirac, D. Poilblanc, N. Schuch, and F. Verstraete, *"Entanglement spectrum and boundary theories with projected entangled-pair states"*, Physi. Rev. B **83**, (2011).

[59] S. Sachdev, *Quantum Phase Transitions*. Cambridge University Press, 2 ed., 2011.

[60] K. G. Wilson, *"Confinement of quarks"*, Phys. Rev. D **10**, 2445–2459 (1974).

[61] A. Khare, *Fractional Statistics and Quantum Theory*. World Scientific, 2nd ed., 2005.

[62] C. Nayak, S. H. Simon, A. Stern, M. Freedman, and S. Das Sarma, *"Non-Abelian anyons and topological quantum computation"*, Rev. Mod. Phys. **80**, 1083–1159 (2008).

[63] A. G. Fowler, M. Mariantoni, J. M. Martinis, and A. N. Cleland, *"Surface codes: Towards practical large-scale quantum computation"*, Phys. Rev. A **86**, (2012).

[64] H. Bombin and M. A. Martin-Delgado, *"Topological Quantum Distillation"*, Phys. Rev. Lett. **97**, (2006).

[65] M. Srednicki, *"Entropy and area"*, Phys. Rev. Lett. **71**, 666–669 (1993).

[66] J. Eisert, M. Cramer, and M. B. Plenio, *"Colloquium: Area laws for the entanglement entropy"*, Rev. Mod. Phys. **82**, 277–306 (2010).

[67] K. Kato, F. Furrer, and M. Murao, *"Information-theoretical formulation of anyonic entanglement"*, Phys. Rev. A **90**, (2014).

[68] P. Bonderson, C. Knapp, and K. Patel, *"Anyonic entanglement and topological entanglement entropy"*, Ann. Phys. **385**, 399–468 (2017).

[69] B. Shi, K. Kato, and I. H. Kim, *"Fusion rules from entanglement"*, Ann. Phys. **418**, 168164 (2020).

[70] R. Haag and D. Kastler, *"An Algebraic Approach to Quantum Field Theory"*, J. Math. Phys. **5**, 848-861 (1964).

[71] A. Garbarz and G. Palau, *"A note on Haag duality"*, Nucl. Phys. B **980**, 115797 (2022).

[72] P. Naaijkens, *"Haag Duality and the Distal Split Property for Cones in the Toric Code"*, Lett. Math. Phys. **101**, 341–354 (2012).

[73] L. Fiedler and P. Naaijkens, *"Haag duality for Kitaev's quantum double model for abelian groups"*, Rev. Math. Phys. **27**, 1550021 (2015).

[74] Y. Ogata, *"A derivation of braided C*-tensor categories from gapped ground states satisfying the approximate Haag duality"*, J. Math. Phys. **63**, (2022).

[75] Y. Ogata, *"Mixed state topological order: operator algebraic approach"*, 2025. https://arxiv.org/abs/2501.02398.

[76] Y. Ogata, D. Pérez-García, and A. R. de Alarcón, *"Haag Duality for 2D Quantum Spin Systems"*, 2025. https://arxiv.org/abs/2509.23734.

[77] F. Verstraete and J. I. Cirac, *"Renormalization algorithms for Quantum-Many Body Systems in two and higher dimensions"*, 2004. https://arxiv.org/abs/cond-mat/0407066.

[78] C. H. Bennett, H. J. Bernstein, S. Popescu, and B. Schumacher, *"Concentrating partial entanglement by local operations"*, Phys. Rev. A **53**, 2046–2052 (1996).

[79] M. B. Hastings, *"An area law for one-dimensional quantum systems"*, J. Stat. Mech.: Theory Exp. **2007**, P08024–P08024 (2007).

[80] I. Arad, A. Kitaev, Z. Landau, and U. Vazirani, *"An area law and sub-exponential algorithm for 1D systems"*, 2013. https://arxiv.org/abs/1301.1162.

[81] G. Vidal, *"Efficient Classical Simulation of Slightly Entangled Quantum Computations"*, Phys. Rev. Lett. **91**, (2003).

[82] G. Vidal, *"Classical Simulation of Infinite-Size Quantum Lattice Systems in One Spatial Dimension"*, Phys. Rev. Lett. **98**, (2007).

[83] S. R. White, *"Density matrix formulation for quantum renormalization groups"*, Phys. Rev. Lett. **69**, 2863–2866 (1992).

[84] S. R. White, *"Density-matrix algorithms for quantum renormalization groups"*, Phys. Rev. B **48**, 10345–10356 (1993).

[85] U. Schollwöck, *"The density-matrix renormalization group in the age of matrix product states"*, Ann. Phys. **326**, 96–192 (2011).

[86] D. Pérez-García, M. Sanz, C. E. González-Guillén, M. M. Wolf, and J. I. Cirac, *"Characterizing symmetries in a projected entangled pair state"*, New J. Phys. **12**, 025010 (2010).

[87] S. Singh, R. N. C. Pfeifer, and G. Vidal, *"Tensor network decompositions in the presence of a global symmetry"*, Phys. Rev. A **82**, (2010).

[88] R. Orús and G. Vidal, *"Infinite time-evolving block decimation algorithm beyond unitary evolution"*, Phys. Rev. B **78**, (2008).

[89] V. Zauner-Stauber, L. Vanderstraeten, M. T. Fishman, F. Verstraete, and J. Haegeman, *"Variational optimization algorithms for uniform matrix product states"*, Phys. Rev. B **97**, (2018).

[90] A. Rényi, *"On measures of infromation and entropy"*, Berkeley Symposium on Mathematics, Statistics and Probability **4**, (1961).

[91] S. T. Flammia, A. Hamma, T. L. Hughes, and X.-G. Wen, *"Topological Entanglement Renyi Entropy and Reduced Density Matrix Structure"*, Phys. Rev. Lett. **103**, 261601 (2009).

[92] A. Uhlmann, *"The "transition probability" in the state space of a $*$-algebra"*, Rep. Math. Phys. **9**, 273-279 (1976).

[93] H. T. Quan, Z. Song, X. F. Liu, P. Zanardi, and C. P. Sun, *"Decay of Loschmidt Echo Enhanced by Quantum Criticality"*, Phys. Rev. Lett. **96**, 140604 (2006).

[94] S.-J. GU, *"Fidelity Approach to Quantum Phase Transitions"*, Int. J. Mod. Phys. B **24**, 4371–4458 (2010).

[95] H.-Q. Zhou, *"Renormalization group flows and quantum phase transitions: fidelity versus entanglement"*, 2007. https://arxiv.org/abs/0704.2945.

[96] N. Paunković, P. D. Sacramento, P. Nogueira, V. R. Vieira, and V. K. Dugaev, *"Fidelity between partial states as a signature of quantum phase transitions"*, Phys. Rev. A **77**, 052302 (2008).

[97] C. D. Batista and Z. Nussinov, *"Generalized Elitzur's theorem and dimensional reductions"*, Phys. Rev. B **72**, (2005).

[98] Z. Nussinov and G. Ortiz, *"A symmetry principle for topological quantum order"*, Ann. Phys. **324**, 977–1057 (2009).

[99] D. Gaiotto, A. Kapustin, N. Seiberg, and B. Willett, *"Generalized global symmetries"*, J. High Energy Phys. **2015**, (2015).

[100] J. McGreevy, *"Generalized Symmetries in Condensed Matter"*, Annu. Rev. Condens. Matter Phys. **14**, 57-82 (2023).

[101] M. B. Hastings and X.-G. Wen, *"Quasiadiabatic continuation of quantum states: The stability of topological ground-state degeneracy and emergent gauge invariance"*, Phys. Rev. B **72**, (2005).

[102] X.-G. Wen, *"Emergent anomalous higher symmetries from topological order and from dynamical electromagnetic field in condensed matter systems"*, Phys. Rev. B **99**, (2019).

[103] K. Fredenhagen and M. Marcu, *"Charged states in $\mathbb{Z}_2$ gauge theories"*, Commun. Math. Phys. **93**, 81-119 (1983).

[104] K. Fredenhagen and M. Marcu, *"Confinement criterion for QCD with dynamical quarks"*, Phys. Rev. Lett. **56**, 223–224 (1986).

[105] M. Marcu, *"(Uses of) An Order Parameter for Lattice Gauge Theories with Matter Fields"*, 1986.

[106] K. Fredenhagen and M. Marcu, *"Dual interpretation of order parameters for lattice gauge theories with matter fields"*, Nucl. Phys. B - Proc. Suppl. **4**, 352-357 (1988).

[107] F. Pollmann, S. Mukerjee, A. M. Turner, and J. E. Moore, *"Theory of Finite-Entanglement Scaling at One-Dimensional Quantum Critical Points"*, Phys. Rev. Lett. **102**, (2009).

[108] M. Freedman, C. Nayak, K. Shtengel, K. Walker, and Z. Wang, *"A class of P,T-invariant topological phases of interacting electrons"*, Ann. Phys. **310**, 428-492 (2004).

[109] O. Buerschaper, S. C. Morampudi, and F. Pollmann, *"Double semion phase in an exactly solvable quantum dimer model on the kagome lattice"*, Phys. Rev. B **90**, (2014).

[110] F. Verstraete and J. I. Cirac, *"Matrix product states represent ground states faithfully"*, Phys. Rev. B **73**, (2006).

[111] N. Schuch, M. M. Wolf, F. Verstraete, and J. I. Cirac, *"Entropy Scaling and Simulability by Matrix Product States"*, Phys. Rev. Lett. **100**, (2008).

[112] F. G. S. L. Brandão and M. Horodecki, *"An area law for entanglement from exponential decay of correlations"*, Nature Physics **9**, 721–726 (2013).

[113] Z.-C. Gu, M. Levin, and X.-G. Wen, *"Tensor-entanglement renormalization group approach as a unified method for symmetry breaking and topological phase transitions"*, Phys. Rev. B **78**, (2008).